Compliant Substrates for Materials on Silicon

by

Kate Black

Thesis submitted for the degree of Doctor in Philosophy (PhD) in accordance with the requirements of the University of Liverpool.

July 2008

K.B.O

Winston Churchill 1942.

Abstract

This thesis describes the development of processes to fabricate compliant layers for the epitaxy of gallium nitride on silicon. A range of metalorganic chemical vapour deposition processes have been investigated. Three generic materials systems have been explored, namely: a perovskite-based rare earth aluminate; a rocksalt nitride system; and a hexagonal symmetry oxide based buffer layer.

Single source precursors for the deposition of lanthanum- and praseodymium- aluminate have been demonstrated using $[LnAl(OPr^i)6(Pr^iOH)]_2$ (Ln = La or Pr) for the first time. Annealing the films above 850°C crystallises them to form a rhombohedral perovskite phase. The growth of gallium nitride on these films has been investigated to establish their chemical stability. The GaN growth is textured and the interface between the oxide and GaN is abrupt indicating negligible interdiffusion. The promotion of better epitaxy via a SrO seed layer to inhibit adverse interfacial interactions is considered.

The deposition rocksalt structured LaN and ScN on Si(111) is investigated using $M[N(SiMe_3)_2]_3$ (M = La or Sc) precursors via a transamination reaction. The thin layers were susceptible to oxidation in the ambient, which prevented subsequent analysis or GaN growth. To overcome this, molecular beam epitaxy studies of the nitride buffer layers were investigated. The optimum growth temperature for ScN is 850°C. Selective area diffraction reveals the epitaxial relationship between the ScN and Si substrate is $(111)_{ScN}//(111)_{Si}$ and $[1\ \bar{1}0]_{ScN}//[0\ \bar{1}1]_{Si}$. After gallium nitride deposition diffraction measurements indicate the structure: GaN [0001] // Si [111] and GaN($1\ \bar{1}00$) // Si($11\ \bar{2}$). Even after capping with gallium nitride, the MBE LaN was prone to oxidation and spalling.

The feasibility of depositing gallium nitride on silicon by molecular beam epitaxy has been demonstrated employing a ZnO compliant layer. $[Me_2Zn(THF)]$ produced films consisting of a nano-rods microstructure, however $[Zn(thd)_2]$ produced films with a film-like morphology. MBE GaN films grown at 600°C on the ZnO nano-rods led to the complete removal of the ZnO and the formation of a $[Si/GaO_x/GaN]$ heterostructure. GaN deposited on ZnO films led to the formation of a 2nm $Ga_xZn_yO_z$ interlayer. The GaN microstructure was c-axis oriented but with significant azimuthal misorientation.

Publications

Some of the results and discussions of the research presented in chapters 4 and 6 and other work performed during the course of study have been published in the following scientific literature.

1. *Black K*, Jones A.C., Chalker P.R., Gaskell J.M., Murray , Joyce T.B., Rushworth S.A., 'MOCVD of ZnO thin films for potential use as compliant layers for GaN on Si', Journal of Crystal Growth, **310**(5) (2008) pp. 1010-1014

2. O'Kane R , Gaskell J, Jones A.C., Chalker P.R., *Black K*, Werner M , Taechakumput P , Taylor S, Heys P.N., Odedra R, 'Growth of HfO_2 by liquid injection MOCVD and ALD using new hafnium -cyclopentadienyl precursors ', Chemical Vapor Deposition, **13**(11) (2007) pp. 609-617

3. Gaskell J.M., Przybylak S, Jones A.C., Aspinall H.C., Chalker P.R, *Black K*, Potter RJ, Taechakumput P, Taylor S, 'Deposition of Pr- and Nd-aluminate by liquid injection MOCVD and ALD using single-source heterometallic alkoxide precursors', Chemistry of Materials, **19**(19) (2007) pp. 4796-4803

4. Gaskell JM, Jones AC, Aspinall HC, Przybylak S, Chalker PR, *Black K*, Davies HO, Taechakumput P, Taylor S, Critchlow GW, 'Liquid injection MOCVD and ALD of ZrO_2 using Zr-cyclopentadienyl precursors', Journal of Materials Chemistry, **16**(39) (2006) pp. 3854-3860

5. Gaskell J.M., Jones A.C., *Black K*, Chalker P.R., Leese T, Kingsley A, Odedra R, Heys P.N., 'Liquid injection ALD and MOCVD of lanthanum aluminate using a bimetallic alkoxide precursor'. Surface & Coatings Technology, **201**(22-23) (2006) pp. 9095-9098

List of Figures

List of Tables

Acknowledgments

First and foremost, I would like to express my profound gratitude to my supervisors, Professor Paul Chalker and Professor Anthony Jones for their invaluable support, encouragement and supervision. Throughout my Ph.D studies Paul provided guidance, sound advice, good company and plenty of first-class ideas. I would have been lost without him. Tony has been a great mentor, a friend and the person who gave me the opportunity to fulfil my aspirations. Without their combined faith and belief in me, none of this would have been possible.

I am grateful to all involved in the COSMOS project: Dr Peter Wright, Mr Doug Warne and Mr Simon Rushworth who were always willing to help answer my questions without hesitation. Their comments and guidance were useful contributions during my research. Moreover, I would like to acknowledge all my colleagues at the University of Liverpool, with special thanks to Dr Robert Murray, Dr Tim Joyce, Dr Simon Romani and Mr David Atkinson.

I also wish to thank my sisters Jessica and Amy together with Julian for their continuous support and understanding during my studies. My sincere appreciation goes to my friends for all their emotional support, camaraderie and entertainment, which was a welcome relief.

Finally, the greatest thanks of all must go to my parents, Linda and Neil who throughout my education believed in me where others doubted. Without their love, belief and encouragement this amazing journey could never have happened.

Contents

Chapter 3 Experimental Methods

Chapter 4 Lanthanum and praseodymium aluminate

Chapter 5 Lanthanum Nitride and Scandium Nitride

Glossary

θ	Scattering angle
acac	Pentane-2,4dionate
AFM	Atomic force microscopy
ALD	Atomic layer deposition
C-V	Capacitance - voltage
DEZ	Diethyl Zinc
DMZ	Dimethyl Zinc
EDX	Energy dispersive X-ray
EELS	Electron energy loss spectroscopy
ELS	Energy loss spectroscopy
Hfac	1,1,1,5,5,5-hexafluoro-2-4-pentanedionate
J-V	Current density - voltage
MBE	Molecular beam epitaxy
MEIS	Medium energy ion scattering
MOCVD	Metalorganic chemical vapour deposition
MOVPE	Metal organic vapour phase epitaxy
rms	Root mean square
RT	Room temperature
SNMS	Sputtered neutral mass spectrometry
STEM	Scanning transmission electron microscopy
TEM	Transmission electron microscopy
thd	2,2,6,6-tetramethyl-3,5-heptanedionate
THF	Tetrahydrofuran
XRD	X-ray diffraction

Chapter 1

Introduction

1.1. Context of the research within the COSMOS project

The research in this PhD was conducted within the framework of the DTI Basic Technologies for Industrial Applications project: 'COSMOS - Oxide based compliant layers for the integration of InP and GaAs epitaxial layers on to silicon'. The project originally involved four partners, namely: QinetiQ Ltd; Kamelian Ltd; Epichem Ltd; and the University of Liverpool.

At the outset of the project in February 2004, the aim of the research was to demonstrate a commercially viable, cost effective, 'universal' substrate based on silicon onto which a range of high quality single crystal III-V semiconductors and oxides could be deposited. The second objective for the project partners was to evaluate these substrates by fabricating demonstrator electronic devices from the semiconductor layers deposited and assessment of their performance.

The original objectives of the project were:

- Design, synthesis and manufacture of precursors.
- Develop low cost CVD based route to manufacture the compliant substrate.

- Identify and realise compliant substrates to allow the deposition of commercially important target III-V semiconductor materials based on InP and GaAs.
- Demonstrate manufacture of the target materials.
- Exploitation in conjunction with end users.

Regrettably, within the first year of the project Kamelian ceased to trading and in the second year, the project aims were refocused towards the development of compliant substrates for the *GaN-based* semiconductor materials, which could be exploited by Qinetiq.

The project partners considered two generic approaches to achieving epitaxial growth of semiconductors on silicon substrates via either oxide-based compliant layers or non-oxide based (nitride) ones. The candidates for the oxide-based compliant layers fell into three quite distinct categories. In its simplest form, the layer could be a single binary oxide, which forms a good lattice match to silicon. Examples include some rare earth oxides [1,2]. The second type includes more complex oxides with the perovskite structure [3] where matching is achieved through a 45° rotation between the oxide lattice and the silicon to achieve the matching required. The last type uses a series of thin oxide layers to provide the stable interface and orientation control in the subsequent layers.

The options for non-oxide compliant layer systems include stoichiometric nitride materials. One approach is to use 'domain matched epitaxy' where an integral number of silicon unit cells is equivalent to an integer

number of compliant layer unit cells. (e.g. TiN on silicon with 4 TiN cells equivalent to 3 silicon). The second approach exploits a nitride initially matched to silicon but then graded in composition towards the target material.

1.2 The research embodied within this thesis

The research described within this thesis describes the research of compliant layers deposited using precursors and chemical vapour deposition (CVD) processes developed at Liverpool. Only the development of compliant layers for gallium nitride is described.

To achieve a suitable substrate for the integration of GaN-based materials to silicon, attempts were made to utilise rare earth aluminates, nitride materials such as LaN and Sc and oxide materials (ZnO). Precursors for the CVD of these materials were developed to allow the exploitation of the reaction between ammonia and the rare earth silylamide precursors. Deposition of the nitride materials proved a challenge. Attempts to deposit the metal nitrides yielded low temperature deposited thin films but these were essentially the metal oxide rather than the nitride. The chemistry of the transamination reaction giving a low temperature intermediate as expected but this then reacts with traces of oxygen containing species in the reactor to yield the oxide based product. However, this route opens a new method of depositing rare earth oxides at low temperatures by CVD, which could have significant potential applications. A novel route for the deposition of ZnO was devised which gave high quality films but the thermal

stability of the ZnO presented limitations on their subsequent use for GaN deposition.

1.3 Structure of the thesis

In Chapter 2, an overview of materials that are candidates as buffer layers and substrates for gallium nitride epitaxy is presented. The chapter considers a range of factors that are important in growth processes and epitaxy of thin films. The history and development of the MOCVD and MBE growth processes is reviewed. Finally a brief consideration of the potential applications of III-nitride based semiconductors is given. In the following chapter, the growth processes and analytical techniques used throughout this thesis are described. In particular, the MOCVD reactors employed in this research are reviewed and the important experimental parameters are stated.

In Chapter 4, the deposition of rare earth aluminate ($MAlO_3$, M = La or Pr) compliant layers by MOCVD and ALD is reported. A single-source alkoxide precursor $[MAl(OPr^i)_6(PriOH)]_2$ is used for the first time. The rationale for this approach is to exploit the stoichiometry of the precursor molecule to achieve the 'perovskite-like' composition. Post growth annealing experiments are reported that reveal the crystallization temperature. The physical structure and electrical properties of the films have been characterised. The interaction between the metal aluminate and the silicon substrate is investigated using medium energy ion scattering. This analysis reveals that inter-diffusion occurs after high

temperature treatments and the nature of the resulting interface is discussed. Because of this interlayer, the resulting buffer layers are not epitaxially oriented. The growth of gallium nitride on the aluminate films is discussed.

Chapter 5 describes the development of lanthanum nitride and scandium nitride for compliant layers. The MOCVD of these materials is investigated using a novel approach based on a low temperature gas-phase transamination reaction. The thermodynamic stability of the nitride layers with respect to their oxides is considered, as this is an important issue in a compliant layer deposition process.

In addition to the MOCVD studies, an alternative approach to deposition of LaN and ScN was developed using molecular beam epitaxy. Layers of these rocksalt structured materials were subsequently used as substrates for epitaxial GaN growth. Scanning transmission electron microscopy has been used to investigate the microstructure of the interface between the nitride and silicon.

The sixth chapter presents a study of the MOCVD of zinc oxide, which is a candidate compliant layer material. The influence of lattice parameter mismatch and polarity of the oxide are significant issues in the subsequent growth of gallium nitride and are discussed.

Two precursors are investigated: dimethyl zinc – tetrahydrofuran; and bis(2,2,6,6-tetramethyl-3,5-heptanedionate) zinc for the MOCVD of zinc

oxide. The resulting microstructure of the compliant layers is analysed using electron microscopy and X-ray diffraction. The layers are subsequently used as substrates to explore the molecular beam epitaxy of gallium nitride.

The last chapter provides a summary of the major outcomes of this thesis and their relevance to the COSMOS project research. It also considers the prospects for further research arising from this thesis. The major areas for development include. The most important of these is the exploitation of the SrO based seed layer developed by Qinetiq that should be coupled with the rare earth aluminate compliant layers. Other areas for further consideration include the development of a precursor system for the deposition of perovskite-like compositions. The development of graded rocksalt based nitrides based on the ternary alloy $La_xSc_{1-x}N$ should be considered. Finally the use of ZnO nanowires should be investigated further as a means of integrating gallium nitride epitaxially with silicon substrates.

References

1. Jeutter, N. M., Hennemeyer, M., Stark, R. W., Stierle, A., Moritz, W., 'Growth of epitaxial Pr_2O_3 layers on Si(111)', Materials Science in Semiconductor Processing, 9(6) (2006) pp. 1079-1083

2. Schroeder T, Lee TL, Libralesso L, Joumard I, Zegenhagen J, Zaumseil P, Wenger C, Lupina G, Lippert G, Dabrowski J, Mussig HJ, 'Structure and strain relaxation mechanisms of ultrathin epitaxial Pr_2O_3 films on Si(111)', Journal of Applied Physics, 97(7) (2005) Art. 074906

3. Yu, Z; Liang, Y; Li, H; Curless, J; Overgaard, C; Droopad, R; Wei, Y; Hu, X; Craigo, B; Finder, J; Eisenbeiser, K; Talin, A; Smith, S; Voight, S; Wang, J; Marshall, D; Jordan, D; Edwards, J; Moore, K, "Progress in epitaxial oxides on semiconductors', Crystalline Oxide-Silicon Heterostructures And Oxide Optoelectronics. Materials Research Society Symposium Proceedings 747 (2003) 31-42

Chapter 2

Literature review

2.1. Background and rationale

Gallium nitride (GaN) is a material that has many benefits and applications in electronic and optical devices. For example, it has been possible to manufacture GaN-based white light emitters with efficiencies an order of magnitude higher than is available using incandescent bulbs [1]. Considerable research and development effort has been aimed at integrating the currently used technologies in order to improve efficiency, performance and competitiveness, and thereby reduce the cost of manufacturing electro-optical components. Within this research and development context, the ability to deposit device quality single crystal III-V semiconductor materials onto silicon has formed one of the primary objectives in the semiconductor industry.

The broad aim of the COSMOS research project was to investigate the deposition of a "universal" substrate onto silicon, thus allowing GaN and other high quality single crystal III-V semiconductors to be grown. The underpinning rationale for the work is that it should be possible, simply by adjusting the composition of such a "universal" substrate, to deposit a compliant layer with favourable lattice parameters. The ability to develop and manufacture such an innovative and versatile substrate would represent a step change in the semiconductor industry, bringing with it potentially enormous advantages spanning a wide range of

applications and technologies. Moreover, this would simplify greatly the current manufacturing processes, reduce the tool sets required and open the way for more rapid device design, prototyping and development. In particular, access to large area silicon-based substrates (currently available up to 300mm diameter) would facilitate scaling-up and hence significant cost reductions, shorten development times for large area III-V semiconductors and allow new product markets to be explored.

The purpose of this review is to provide a broad background of information spanning the various aspects of GaN-related topics of importance to deposition research. It includes sections devoted to epitaxy; crystal structure; and band properties. It also considers how these may be utilised in the search for a "universal" compliant layer. Additional sections cover areas such as III-V growth techniques; substrate materials and III-N based devices.

2.2. Gallium Nitride (GaN)

GaN has many unique properties that render it a very useful material for application in a wide range of electronic and optical devices. In recent years, research has focused on attempts to integrate GaN with silicon devices[2], driven largely by the desire to find less expensive and more accessible alternatives to the sapphire and silicon carbide substrates presently used. In order to understand why GaN is the material of choice for a growing number of optoelectronic device applications, its key electronic properties and crystal lattice characteristics (Table 2.2.1) must first be considered. This draws on a recent review by Liu and Edgar [3] in

which the properties of GaN epilayers deposited on various commonly used substrates have been reported in detail.

Under ambient and thermodynamically stable conditions, GaN normally takes on a wurtzite structure having a P63mc space group. This structure consists of alternating diatomic close packed [0001] planes of Ga and N pairs formed in an ABAB sequence. In this structure, the atoms in the first and third layers are directly aligned with each other. Figure 2.1 illustrates the wurtzite GaN structure along the [0001], [1120] and [1010] lattice planes; in this diagram, the [0001] planes represent the close packed ones. Since group III nitrides lack an inversion plane perpendicular to the c-axis, the crystal surfaces have either an N-polarity or a group III element (Al, Ga or In) polarity.

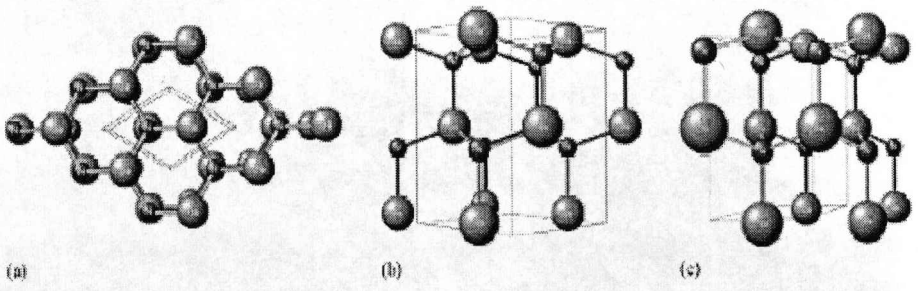

Figure 2.1 Perspective views of wurtzite GaN along various directions: (a) [0001] (b) [1120] and (c) [1010]. Large circles represent Ga atoms; small circles represent N atoms (Edgar and Liu [3])

Table 2.1 Properties of gallium nitride

Property	Value
Energy band gap (eV) (300 K)	3.44
Maximum electron mobility ($cm^2/V\ s$)	
300 K	1350
77 K	19200
Maximum hole mobility (300 K) (cm^2/Vs)	13
Controlled doping range (cm^3)	
n-type	1016-1020
p-type	1016-1018
Melting point (60 kbar) (K)	>2573
Lattice constants (300 K)	
a (nm)	0.318843
c (nm)	0.518524
Percentage change	
Thermal conductivity (300 K) (W/cm K)	2.1
Heat capacity (300 K) (J/mol K)	35.3
Modulus of elasticity (GPa)	210 ±23

Under thermodynamically unstable conditions, GaN sometimes forms a zincblende structure, known to form when grown on cubic substrates such as silicon or gallium arsenide. In this zincblende structure, the stacking sequence is ABCABC and the (111) planes are the closely packed planes. Figure 2.2 shows the GaN zincblende structure from different angles.

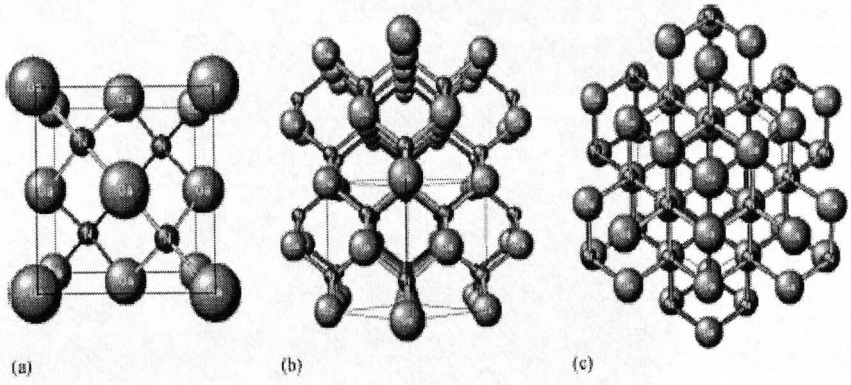

Figure 2.2. Perspective views of zincblende GaN along various directions (a) [100] (1x1x1 unit), (b) [110] (2x2x2 units) and (c) [111] (2x2x2 units) (Edgar and Liu [3])

The quality of GaN films is determined by a range of factors including: defects, impurities, phase purity and functional properties. These factors can be investigated by analytical techniques including transmission electron microscopy (TEM), X-ray diffraction (XRD), Raman spectroscopy, atomic force microscopy (AFM), photoluminescence and SIMS. Many of these techniques have been employed in this project to evaluate the quality of GaN layers and these are discussed in more detail in Chapter 3.

The lattice parameters of the III-nitride binary materials have been reviewed in some detail by Orton and Foxon[4] and those pertaining to the three principal binary III-nitrides are given in Table 2.2. This data permits electronic charge carrier densities, lattice mismatch between III-nitride epilayer and substrate material and strain to be quantified.

Table 2.2 WB and ZB lattice parameters for the nitride semiconductors

Material	a_0 (Å)	c_0 (Å)	c_0/a_0	a_0 (ZB)
AlN	3.112±0.002	4.980±0.002	1.601±0.001	4.38
GaN	3.1892±0.0009	5.1850±0.0005	1.6258±0.0006	4.52±0.03
InN	3.540±0.008	5.80±0.10	1.615±0.008	4.98

2.3 Gallium Nitride and III-V Crystal Growth Techniques

There are many growth techniques used in the semiconductor industry for the deposition of III-V and III-nitride materials. Two of the most commonly used techniques and the ones used in this particular work, are that of metal organic chemical vapour deposition (MOCVD) [5-6] and molecular beam epitaxy (MBE)[7-8]. These growth methods have previously been used to deposit a wide range of semi-conducting materials.

2.3.1 Metal Organic Chemical Vapour Deposition (MOCVD)

MOCVD is a widely used growth technique as it is particularly well suited to modern manufacturing methods in the semiconductor industry. It also offers the potential for large area growth and good composition control. MOCVD is important in this particular work as the development of a low cost CVD based route would be a key step in the commercialisation of a compliant layer technology in terms of cost and wafer throughput. Provision of a "universal" substrate technology by

CVD would therefore provide a step change improvement in manufacturing capability and reduction in costs.

The earliest application of metalorganic compounds to deposit III-V semiconductor layers was published by Manasevit in 1968 [9]. It involved the deposition of GaAs by the pyrolsis of a mixture of triethylgallium (Et_3Ga) and arsine (AsH_3) in an open tube system using hydrogen as the carrier gas. This was the first true example of metalorganic chemical vapor deposition (MOCVD). Mansasevit was primarily interested in the growth of films on insulating substrates, such as sapphire. The advancement of MOCVD occurred rapidly and the growth of GaAs on GaAs substrates was demonstrated.[10] Many other groups showed the versatility of the MOCVD technique and by 1973 numerous III-V compound semiconductors had been deposited in this way. Nevertheless, the purity levels of these films were still not up to the quality required for device applications. This standard was not reached until 1975, when Seki *et al* grew a film of GaAs with an electron mobility as high as 120 000 $cm^2\ V^{-1}s^{-1}$. [11] This achievement allowed the realisation of state-of-the-art devices such as GaAs photocathodes and field effect transistors (FETs)[12]. It was also demonstrated that the MOCVD technique was capable of the growth of complex multilayer structures such as AlGaAs/GaAs/AlGaAs.[13] Subsequently, MOCVD was further improved by the introduction of low reactor pressures (i.e. 0.1 atm). This step helped to avoid any unwanted pre-reactions between the group III and V precursors and made possible the growth of complex quaternary structures with abrupt interfaces between layers (e.g. InGaAsP).

The deposition of GaN is now frequently deposited using trimethyl gallium and ammonia [14]. Ammonia is used as the nitrogen source due to its availability and the fact that it can be readily decomposed at the deposition temperatures of the GaN (1000°C). The first GaN deposited using MOCVD [15] had poor morphologies and high background carrier densities (> 10^{17} to 10^{19} cm^{-3}). The quality of the GaN epilayers was improved when Amano *et al* [16] employed a thin AlN buffer layer before the GaN growth. This development facilitated deposition of smoother crack-free GaN. Amano's process deposited the AlN buffer layer at a temperature of 600°C. The substrate temperature was then raised to 1040°C for the growth of the GaN layer. X-ray diffraction showed that the quality of the GaN was good. The feasibility of using a buffer layer for the deposition of GaN was established and many other groups started to investigate other possible candidates such as low temperature GaN buffer layers [17].

2.3.2 Precursors

MOCVD reactors generally operate at intermediate pressures of around 1-200mbar. This allows chemical reactions to occur in both the gas-phase and on or close to the substrate. One of the most important factors in the MOCVD process is that of the precursor and is availability and suitability. Ideally, MOCVD precursors should possess a number of properties to be commercially viable. The principle property of sufficient volatility is essential for acceptable growth rates. An adequately wide temperature window is also needed between evaporation and thermal

decomposition. 'Clean' decomposition i.e. without the incorporation of residual impurities is essential. Other factors include: good compatibility with co-precursors during the growth of complex films; a long shelf life; and they should present a low hazard risk. It is very unlikely that a single precursor will posses all of these attributes and some compromises are nearly always needed.

2.3.3 Molecular Beam Epitaxy

Molecular Beam epitaxy (MBE) was first developed in the 1970's, having evolved from surface kinetic studies of the interactions of Ga and As gas beams with GaAs [18]. The term MBE was first coined by Cho *et al*[19], who demonstrated that the technique could be used to successfully deposit a variety of III-V materials. Prior to this, MBE systems were based on single vacuum chambers designed for loading, deposition and analysis. The drawback of this approach is long pump-down times between growth runs. Improvements to the single vacuum chamber system were necessary before the deposition of high quality films was possible. In this respect, the introduction of a substrate-exchange load lock, which also reduced contamination of the deposition chamber, represented a significant advance.

The MBE technique essentially enables complex structures to be deposited atomic layer by atomic layer with precise control over film thickness. The use of ultrahigh vacuum (UHV) systems in MBE allows the growth process to be executed virtually impurity free and enables compatibly with in-situ analytical monitoring (e.g. RHEED). The

background pressure in the growth chamber is typically around 10^{-10} to 10^{-11} Torr. The system usually employs evaporative sources of group III elements called Knudsen cells. These are separated from the growth chamber by shutters, which are designed to provide high precision control of the group III atom fluxes by switching between open and closed positions. The Knudsen cells generate a flux of Al, Ga or In atoms into the growth chamber. Since there is no solid nitrogen source available, an alternative approach has to be used. This is because the typical MBE growth temperatures of range from 400 to 800°C, where molecular nitrogen is almost completely inert. Therefore, an active nitrogen source for nitride growth is achieved by: either radio frequency RF plasma activation of nitrogen; microwave cyclotron resonance excitation of nitrogen; or thermal cracking of ammonia. The use of ammonia as a nitrogen source has proved to be particularly useful for speeding up growth rates to around 1 μm h^{-1}[20]. In this study, both RF plasma source and 'on-surface' cracking of ammonia have been employed in MBE growth runs.

The ability to conduct in-situ monitoring, such as reflection high-energy electron diffraction (RHEED), represents a major advantage of MBE in relation to other available III-V growth techniques. RHEED compatibility permits the real time monitoring of growth rates and of compositional changes in the III-V layers deposited on the substrate. This monitoring capacity has underpinned some significant contributions and advances in GaN studies, despite the overall dominance of MOCVD (section 2.3.1) in this field. For example, MBE studies have

demonstrated that high quality group III nitride devices can be made such as high-power and microwave devices. MBE also allows more control over layer-by-layer growth and has lower deposition rates than that of MOCVD.

2.4 Substrates and compliant layers for Gallium Nitride

The poor availability of bulk GaN substrates has dictated the use of heteroepitaxy in research aimed at growing III-nitride materials on various substrates. Clearly, the benefits of integrated III-V/Si based technologies are more likely to be achieved through consideration of a variety of suitable compliant layer materials. Table 2.3 lists some of these candidate materials together with their basic structural parameters. Background information on a selection of possible substrates and compliant layers is given in sections 2.4.3 and 2.4.4 respectively. Before this, it is useful to consider and understand the terms *epitaxy* (section 2.4.1) and *thin film growth modes* (section 2.4.2).

Table 2.3 Potential substrate materials for GaN

Material	*Structure*	*Space group*	*Lattice constants (nm)*		
			a	*b*	*c*
Semiconductors					
w-GaN	Wurtzite	$P6_3mc$	0.31885		0.5185
zb-GaN	Zincblende	$F\bar{4}3m$	0.4511		
r-GaN	Rock salt	$F\bar{4}3m$	0.422		
w-AlN	Wurtzite	$P6_3mc$	0.31106		0.49795
zb-AlN	Zincblende	F43m	0.438		
r-AlN	Rock salt	Fm3m	0.404		
ZnO	Wurtzite	$P6_3mc$	0.32496		0.52065
β-SiC	3C (ZB)	$F\bar{4}3m$	0.43596		
SiC	4H (W)	$F\bar{4}3m$	0.3073		1.0053
GaAs	Zincblende	$F\bar{4}3m$	0.56533		
GaP	Zincblende	$F\bar{4}3m$	0.54309		
Si	Diamond	$Fd\bar{3}m$	0.54310		
Oxides and sulphides					
Al_2O_3	Rhombohedral	$R\bar{3}c$	0.4765		1.2982
$MgAl_2O_4$		$F\bar{4}3m$	0.8083		
$LiGaO_2$	Orthorhombic	$Pna2_1$	0.5402	0.6372	0.5007
$NdGaO_3$	Orthorhombic	$Pna2_1$	0.5428	0.5498	0.771
$LaAlO_3$	Rhombohedral	$R\bar{3}c$	0.5364		1.1311
Metals and metal Nitrides					
Hf	HCP	$P6_3mc$	0.318		0.519
Zr	HCP	$P6_3mc$	0.318		0.519
ZrN	Rock salt	$F\bar{4}3m$	0.45776		
Sc	HCP	$P6_3mc$	0.3309		0.54
ScN	Rock salt	$F\bar{4}3m$	0.4502		
TiN	Rock salt	$F\bar{4}3m$	0.4241		

2.4.1 Epitaxy:

The term *epitaxy* is derived from two Greek words: *epi* meaning placed upon and *taxis* meaning arrangement. In the context of this field of research, epitaxy refers to "the extended single-crystal film formation on top of a crystalline substrate"[21]. There are two forms of epitaxy: *homoepitaxy* and *hetroepitaxy*. The former refers to the situation where the film and substrate are formed of the same material. For example, epitaxial Si deposited on Si substrates produces a film that has fewer defects and which is purer than the substrate itself. *Heteroepitaxy* is where film and substrate are composed of different materials e.g. AlAs deposited on GaAs. The differences between the two types of epitaxy are illustrated in Figure 2.3.

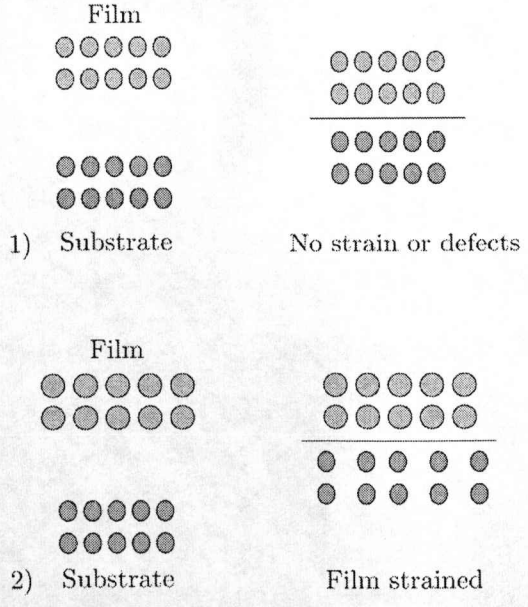

Figure 2.3 schematic illustrations of the two types of epitaxy, (1) homoepitaxy and (2) heteroepitaxy.

When the film and substrate are the same material (homoepitaxy) they are perfectly matched and therefore no strain develops at the interface. However, when film and substrate crystal structures are different, as in *heteroepitaxy,* lattice mismatch will occur, causing defects in the epilayer. Depending on the extent of lattice mismatch this can give rise to three types of epitaxial possibilities. If the lattice mismatch is small then the interface structure is essentially the same as that prior to deposition. However, owing to differences in chemistry and thermal expansion coefficient of the two materials, the electronic properties of the interface can be strongly affected. When the lattice mismatch of the two materials is more severe, dislocations form at the interface and lattice strains develop in order to accommodate the crystallographic differences between film and substrate.

2.4.2 Growth Modes:

In epitaxial film growth, the initial growth mode is strongly influenced by the nature of the substrate. This arises from the previously mentioned factors, such as lattice mismatch and thermal expansion coefficient and the subsequent affects they give rise to. Three generic modes of epitaxial film growth are possible: the Volmer-Weber (VW); Frank-van der Merwe (FW); and Stranski- Krastanov (SK) modes. The growth mode is not only determined by the substrate but also by the deposition temperature and the adhesion energy involved. The VW-mode, more commonly known as island growth, occurs when small clusters of atoms diffuse over the surface, nucleate on the substrate and grow into islands. These islands eventually coalesce to form a continuous film. The VW-mode occurs when the atoms of the deposited material are more strongly

bonded to each other than to the substrate. In the FW-mode, also termed layer-by-layer growth, the opposite condition prevails whereby the atoms of the deposited material are more strongly bonded to the substrate than to each other. Here, the initial atoms to arrive at the surface condense to form a monolayer across the substrate. The subsequently deposited layers then decrease in their binding strength. The FW-mode requires there to be a much higher mobility of adatoms - atoms arriving at the surface - than in the VW-mode. The third type of growth mode, SK, is a combination of the two previously mentioned modes. Initially, layer-by-layer growth occurs until subsequent layer growth becomes unfavourable, island growth then takes over. This change in growth mode occurs because the decrease in binding energy characteristic of layer-by-layer growth is disturbed. These three modes of thin film growth are illustrated in Figure 2.4.

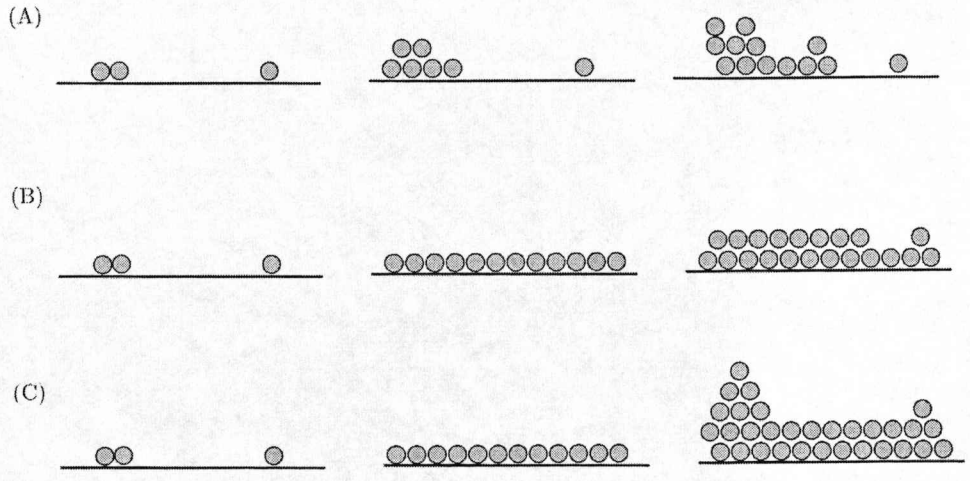

Figure 2.4. The three growth modes in thin film growth, a) showing island growth b) layer-by-layer and c) SK-mode

2.4.3 Substrates

It is clear that both epitaxy and growth modes of thin deposited films can be affected by the nature of the substrate. The substrate can influence many of the properties of the subsequent GaN epilayer(s) and therefore its performance in devices. The epilayer properties that may be affected include crystal orientation, polarity, polytype, surface morphology, and strain and defect concentration. Table 2.4 shows some of the problems that may occur in heteroepitaxy.

Table 2.4 Problems that arise in heteroepitaxy

Substrate property	*Consequence*
Lateral (*a*-lattice constant) mismatch	High misfit (primarily edge) dislocation densities causing: high device leakage currents; short minority carrier lifetimes; reduced thermal conductivity; rapid impurity diffusion pathways
Vertical (*c*-lattice constant) mismatch	Antiphase boundaries, inversion domain boundaries
Surface steps in non-isomorphic substrates	Double positioning boundaries (stacking mismatch boundaries)
Coefficient of thermal expansion mismatch	Thermally induced stress in the film and substrate; crack formation in the film and substrate
Low thermal conductivity	Poor heat dissipation
Different chemical composition than the epitaxial film	Contamination of the film by elements from the substrate; electronic interface states created by dangling bonds; poor wetting of the substrate by the growing film
Non-polar surface	Mixed polarity in the epitaxial film; inversion domains

It has been shown that the shortcomings of heteroepitaxy with GaN, such as crystal quality or poor adhesion characteristics, can be alleviated by appropriate surface preparation for example by nitridation or the deposition of a buffer layer such as AlN[22]. Such alleviation processes have resulted in the production of GaN layers with dislocation densities as low as 10^7 cm^{-2} [23]. However, the semiconductor industry is producing evermore increasingly sophisticated devices that operate under more extreme conditions such as high temperatures or frequencies, which

demand even lower defect densities than this. Therefore substrates capable of supporting better quality GaN epitaxial layers will be needed for the exploitation of these technologies. What follows is a review of some of the common substrates used for the heteroepitaxy of GaN layers and also some of the compliant layers, which are presently employed.

Sapphire (Al_2O_3)

Al_2O_3 is a single crystal aluminium oxide and one of the most commonly used substrates for the epitaxial growth of GaN. The combination of Al_2O_3 and GaN results in a large lattice constant mismatch of ~15%. Consequently, high dislocation densities in the region of 10^{10} cm^{-2} have been reported [24]. Such high defect densities reduce the charge carrier mobility, the minority carrier lifetime and also the thermal conductivity; all of which degrade device performance. The thermal expansion coefficient of Al_2O_3 is greater than that of GaN, producing compressive stress in the epilayer as the wafer is cooled from the deposition temperature. It has been observed that for thick films the stress can crack both the film and substrate [25]. The thermal conductivity of Al_2O_3 is relatively low at around 0.25 W/cmK at 100°C, resulting in poor heat dissipation. The cleavage planes of epitaxial GaN do not parallel those of Al_2O_3, which makes laser facet formation difficult. Al_2O_3 is also electrically insulating and consequently all the electrical contacts must be made to the front of the device. This significantly reduces the area available for devices and complicates fabrication. These and some other properties of Al_2O_3 relevant to epitaxial growth are highlighted in Table 2.5.

Table 2.5 Properties of Sapphire

Property	*Value*	*Range*
Lattice constant (nm)	$a = 0.4765$ $c = 1.2982$	20°C
Melting point (°C)	2030	
Density (g/cm^3)	3.98	20°C
Thermal expansion coefficient (K^{-1})	6.66 x10^{-6} ∥ *c*-axis	20-50°C
	9.03 x10^{-6} ∥ *c*-axis	20-1000°C
	5.00 x10^{-6} ⊥ *c*-axis	20-1000°C
Percentage change in lattice constants	$a/a_0 = 0.83$ $c/c_0 = 0.892$	Heating from 293-1300K
Thermal conductivity (W/cm K)	0.23 ∥*c*-axis	296K
	0.25 ∥*a*-axis	299K
Heat capacity (J/Kmol)	77.9	298K
Young's modulus (GPa)	452-460 in [0001] direction	
	352-484 in [112 $\bar{0}$] direction	
Tensile strength (MPa)	190	300K
Poisson's ratio	0.25-0.30	300K
Dielectric constants	8.60 ∥*c*-axis	10^2-10^8 Hz
	10.55∥*a*-axis	10^2-10^8 Hz
Refractive index	1.77 (λ=577nm)	
	1.73 (λ=233μm)	
Energy band gap (eV)	8.1-8.6	300K
Resistivity (Ωcm)	$>10^{11}$	300K

Al_2O_3 can form single crystal units described by both rhombohedral unit cells with a volume of 84.929 Å and hexagonal unit cells with volume 254.792 Å. Al_2O_3 has a space group of R3c and contains predominantly ionic bonds. Figure 2.5 shows both unit cell types of Al_2O_3. In the

rhombohedral phase there is a total of 10 ions comprising of 4 x Al^{3+} and 6 x O^{2+} ions whereas the hexagonal cell has 30 ions comprising of 12 x Al $^{3+}$ and 18 x O^{2+} ions.

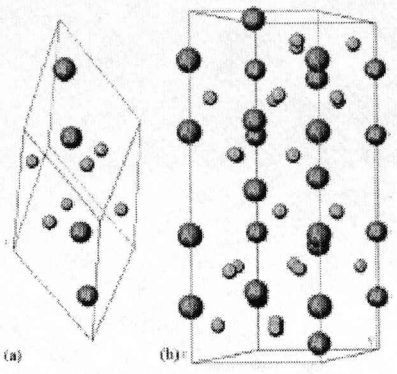

Figure 2.5. The unit cell of sapphire (a) rhombohedral unit cell (b) hexagonal unit cell (Edgar and liu [3]).

Epitaxial GaN can be deposited on various orientations of Al_2O_3 substrates (Table 2.6), the most common of these being the c-plane. In order to produce high quality GaN epilayers, a nitration process must be applied with a high quality buffer layer of AlN or GaN grown at low temperatures e.g. below 500°C. The quality of MBE grown GaN epilayers of the same thickness (1.2μm) were deposited on different planes (c-, a-, r- and m-) and compared by Tripathy et al (1999) [26]. The c- plane produced the best quality GaN heteroepitaxy, giving a smooth and flat surface. The quality of the GaN epilayer decreased when it was deposited on a- plane sapphire and further declined when grown on r-plane and m- plane orientations. Only (0002) and (0004) XRD peaks were observed for GaN epilayers deposited on c- and a- plane sapphire

substrates. Mixed orientations of (0002) and (1120) peaks were observed from those epilayers deposited on r- and m- plane sapphire substrates.

Table 2.6. Crystallographic relationship between GaN films and sapphire substrates.

Crystal plane	*Miller indices (h jk l) or (h k l)*	*GaN plane//sapphire plane*	*GaN direction//sapphire plane*
c	(0001) or (001)	(0001)	[1 $\bar{2}$1 $\bar{0}$]//[1 $\bar{1}$00]
a	(112 $\bar{0}$) or (110)	(0001) or (101 $\bar{0}$)	[112 $\bar{0}$]//[11 $\bar{0}$0] [112 $\bar{0}$]//[0003]
r	(101 $\bar{2}$) or (102)	(112 $\bar{0}$) or (12 $\bar{1}$6)	[0001]//[11 $\bar{0}$1] [0001]//[1 $\bar{0}$11]
m	(101 $\bar{0}$) or (100)	(101 $\bar{3}$) or (12 $\bar{1}$2)	[12 $\bar{1}$0]//[0001] [101 $\bar{0}$]//[12 $\bar{1}$0]

Today, manufactured Al_2O_3 substrates are typified by relatively high root-mean square (RMS) roughness values of less than around 0.1nm. Thus, steps must be taken to reduce RMS roughness prior to the subsequent deposition of layers such as GaN. One of the most commonly used procedures involves baking the Al_2O_3 substrates under a flow of hydrogen at temperatures of between 1000°C and 1100°C prior to MOCVD growth of GaN. Upon the completion of backing, the Al_2O_3 substrates are nitrated by exposure to thermally cracked ammonia or nitrogen plasma source in an MBE system. For the MOCVD process, the Al_2O_3 substrates can be exposed to a mixed hydrogen/ammonia gas.

The nitration of Al_2O_3 has the effect of decreasing the number of defect densities and also improves the electron mobility [26].

Once the surface preparation and nitration of Al_2O_3 substrates is complete, it is known that the subsequent growth of a buffer layer dramatically improves the surface morphology and crystallinity of the GaN layer [27]. A temperature of around 500-550 °C is required for the growth of a GaN or AlN buffer layer for MOCVD and 400 °C for MBE. Amorphous buffer layers may crystallise into films with preferential orientation when they are annealed at high temperatures. Annealing results in a reduction in the density of low angle grain boundaries. The influence of a buffer layer on the subsequent quality of GaN epilayers is well known. For example Kirchner *et al* suggested that the most important parameters include growth temperatures and thickness of buffer layer [28]. Siugiura *et al* demonstrated that post-deposition thermal treatments were also important parameters to consider.

Silicon Carbide (SiC)

The epitaxy of GaN on SiC substrates, of both 4H- and 6H polytypes, has a number of theoretical advantages over that on Al_2O_3. SiC has a relatively small lattice mismatch with GaN (3.1% for [0001] orientated films) and is also characterised by a significantly higher thermal conductivity (3.8W/cmK) [29]. Furthermore, the semiconductor properties of SiC allow fabrication of simpler device structures than are available using Al_2O_3. The parallelism of crystal planes in epitaxial GaN with those of SiC renders the formation of facets by cleaving relatively

easy. The polarity of GaN epilayers can easily be controlled since both carbon and silicon polarities are available.

However, SiC does have some disadvantages as a substrate. For example direct epitaxy of GaN on SiC can prove problematic and the use of a buffer layer such as AlN or $Al_{\chi}Ga_{1-\chi}N$ is needed. This improves the epitaxy of GaN by reducing defect densities but the hardness of SiC makes it is very difficult to obtain a smooth substrate surface. The surface roughness of substrates currently received from manufactures lie in the region of 1nm RMS, an order of magnitude higher than that of Al_2O_3 (0.1nm RMS). This enhanced roughness results in higher defect densities which propagate into the GaN epitaxial layer leading to decreased device efficiency. Since the thermal expansion coefficient of SiC is less than AlN or GaN, at room temperature the films are under biaxial tension. At a practical level, SiC substrates are very expensive and there are very few manufactures producing single crystal SiC.

The basic unit structure for SiC is a covalently bonded tetrahedron of carbon atoms and a silicon atom at its centre or vice versa (SiC_4 or CSi_4) as illustrated in Figure 2.6. The distance between silicon and carbon atoms for all polytypes is around 3.08 Å and the length of the Si-C bonding is about 1.89 Å. The height of the unit cell C varies for different polytypes. This means that the c/a ratios are around 1.641, 3.271, and 4.908 for the 2H-, 4H-, and 6H-SiC polytypes respectively, which is close to the known value [30]. Summary data on the crystal lattice properties of SiC is given in Table 2.7.

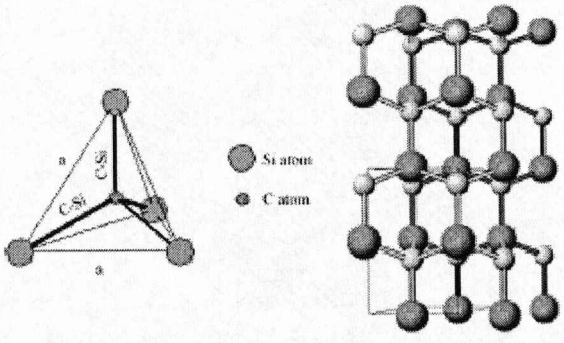

Figure 2.6 The tetrahedral bonding of a carbon atom with four nearest silicon neighbours (Edgar and liu [3])..

Table 2.7. Properties of Silicon Carbide.

Properties	*Polytype*	*Value*
Lattice constant (nm)	3C	$a = 0.43916$
	2H	$a = 0.30753$ $c = 0.50480$
	4H	$a = 0.30730$ $c = 1.0053$
	6H	$a = 0.30806$ $c = 1.51173$
Density (g/cm^3)	3C	3.166
	2H	3.214
	6H	3.211
Melting point (°C)	3C	2.7930
Heat capacity (J/kg K)	6H	0.71
Linear thermal expansion coefficient (x10 $^{-3}$ K^{-1})	3C	3.9
	6H	4.46 *a*-axis
		4.15 *c*-axis
Young's modulus (GPa)	3C	-440
Poisson's ratio	Ceramic	0.183-0.192

Summary information regarding the optoelectronic properties of SiC is given in Table 2.8. Each polytype of SiC has its own set of electronic and optical properties. The most important polytypes for GaN epitaxy are 6H- and 4H- SiC. Lui and Edger [4] have reported that the band gaps for 6H- and 4H- SiC are 3.02 and 3.27eV respectively at liquid helium temperatures. The hexagonal polytypes 4H- and 6H-SiC have the same $P6_3$ mc space group as wurtzite GaN. 3C-SiC/Si (100), 4H- SiC and 6H-SiC are the commercially used substrates for the epitaxial growth of GaN.

Table 2.8. Electrical and optical properties of SiC.

Property	*3C-SiC*	*6H-SiC*	*4H-SiC*
Energy band gap (eV) T-<5K)	24	3.02	3.26
Charge carrier mobilities (cm^2/Vs) (300K)			
Electrons	800	400	1000
Holes	40	101	115
High breakdown electric field (V/cm)	$2.12x10^6$	$2.4x10^6$	$2.2x10^6$
High saturation drift velocity (cm/s)		$2.0x10^7$	$2.0x10^7$
Static dielectric constant	9.72	9.66	
Electrical resistivity (undoped) (Ωcm)			10^2 to 10^3

The production of bulk SiC crystals is often achieved using a modified Lely sublimation process [31]. In this process crystal growth is typically carried out at temperatures of 200 ° C in an argon atmosphere at

pressures between 20 and 500Torr. This technique has resulted in large good quality 4H- and 6H-SiC substrates to be commercially produced. However, a problem with bulk SiC is its high screw dislocation density, which can either be closed or hollow. These holes are oriented to the c-axis and run through the length of the crystal. It is thought that such defects affect the quality of any GaN epilayer, although little research verifying this has been reported in the literature.

Silicon (100) and (111)

The attraction of Si as a substrate for epitaxial GaN deposition stems from its wide availability at low cost and in large sizes. Si also has a much higher degree of crystal perfection than either Al_2O_3 or SiC and therefore its surface can be prepared with a very smooth finish prior to GaN deposition. The $Fd3\bar{m}$ space group of Si gives rise to a diamond structure. This consists of two interpenetrating face cubic centred (fcc) sub-lattices, with one sub-lattice displaced from the other by one quarter of the distance along a body diagonal of the cube. Each Si atom is surrounded by four neighbors that lie at the corners of a tetrahedron. Figure 2.7 represents a Si unit cell along the [001], [011] and [111] directions.

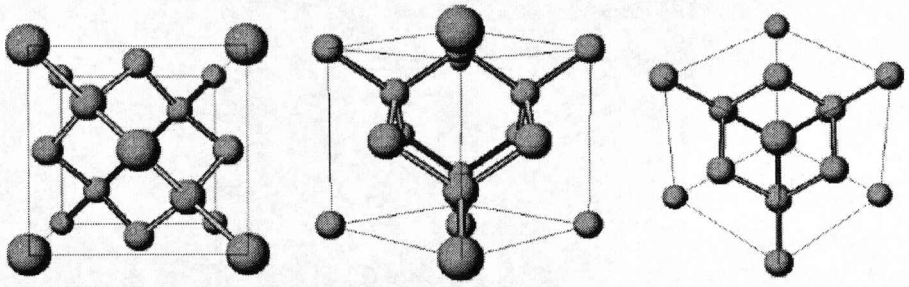

Figure 2.7 Si lattice viewed along the [001],[011] and [111] directions (Edgar and liu [3]).

The two most commonly used Si substrates for GaN deposition are (001) and (111). Both wurtzite and zincblende GaN have been deposited on Si (001) substrates [32], although only wurtzite or mixed phased GaN has been deposited directly onto Si (001). The deposition of zincblende phase GaN requires the deposition of a buffer layer to enhance wetting and also to reduce the lattice mismatch. By far the most commonly used Si substrate for GaN deposition is that of Si (111). However, the use of a buffer layer is again required for high quality defect free GaN growth. The poor quality of epitaxial GaN on Si substrates can be explained by the relatively large lattice and thermal expansion mismatches. The high thermal expansion coefficient of GaN, (5.6 $x10^{-6}$ K) in relation to Si (2.6 x 10^{-6} K) puts the GaN epilayer under tension, causing cracks and defects to occur upon cooling of the film.

2.4.4 Compliant Layers

The quality of the deposited GaN epilayer can be influenced not only by the nature of the underlying substrate but also that of an overlying

compliant or buffer layer. At this point, it is useful to clarify the difference between a compliant layer and a buffer layer. The term compliant layer has been coined to describe an interlayer that will elastically absorb any miss-match induced stresses between the substrate and film. The initial demonstration of compliant substrate technology was by Motorola in 2000[33], involving the deposition of oxide/GaAs structures by MBE. This important work has opened up route ways for the successful integration of III-V semiconductors and other materials, onto Si wafers.

There are many factors to consider when attempting developing a compliant layer, such as compatibility with the growth process (in the case of the present study, MOCVD) an availability of suitable precursors. However, the most critical factors to consider are the lattice and thermal expansion mismatches between the compliant layer, the underlying substrate and overlying film. The stability and electrical properties of the compliant layer material represent additional important factors.

Several mechanisms are available in order to accommodate lattice mismatch: elastic deformation, dislocations, rotation, tilt and cracking. Some of these mechanisms are undesirable, since for example threading dislocations can cause premature device degradation. However, controlled introduction of mismatch can be achieved by using graded layers, which allows better control of dislocation nucleation and multiplication. The following sections review some of the materials that have previously been used as compliant layers for the growth of GaN and some possible new

candidates.

Aluminum Nitride (AlN)

AlN is an attractive candidate as a compliant layer as it shares the same wurzite structure as GaN with the space group of $P6_3mc$. AlN also has similar lattice constants and thermal expansion coefficients] to that of gallium nitride. In this respect it is theoretically possible to produce and abrupt and strain-free compositional interface between the two materials. A further attraction of AlN is that it is capable of supporting eptiaxy on non-*c*-plane substrates and remains stable during GaN growth by both MOCVD and MBE. Table 2.9 provides a summary of some of the key physical, chemical and optical properties of AlN.

Unfortunately, bulk AlN wafers are not commercially available. However, previous workers have been successful in producing AlN crystals by other methods. For example, in 1976 Slack *et al* [34] have reacted aluminum and nitrogen at a temperature of 1850°C. At 2250°C they observed free nucleation of AlN crystallites at the tip of a sealed tungsten crucible. In their study, crystal growth rates of 0.3 mm/h were achieved under an environment of nitrogen. Melt and vaporization techniques have also been used to grow bulk AlN crystals.

Table 2.9. Properties of wurtzite AlN at room temperature (Liu and Edgar 2002)

Properties	*Value*
Lattice constant (bulk crystal, nm)	$a = 0.31106$, $c = 0.49795$
Density (g/cm^3)	3.28
Melting point	2800°C at 100 atm
Heat capacity (J/mol K)	29.83
Thermal conductivity (bulk crystal) (W/cm K)	2.85
Thermal expansion coefficient (linear) x10^{-6}K^{-1})	$a = 2.9$, $c = 3.4$
Young's modulus (GPa)	344.83
Refractive index	2.15±0.5
Dielectric constant	ε(0) : 8.5±0.2; ε(∞):4.68,4.84
Band gap (bulk crystal, eV)	6.2
Electrical resistivity (Ωcm)	
Undoped	10^{7} to 10^{13}
n-, p-type	400, 10^{3} to 10^{5}

The first successful application of AlN as a GaN compliant layer was reported in 1986 by Amano *et al*[35], who deposited a 50nm layer of AlN on an Al_2O_3 substrate prior to depositing GaN by MOCVD. They found that the use of the AlN compliant layer resulted in an improvement in the surface morphology and electrical/optical properties of the GaN epilayer. Further TEM analysis revealed that many defects were present at the AlN/GaN interface but that the defect density decreased abruptly with increasing thickness of the epilayer. From their results it was asserted that the introduction of an AlN layer supplies nucleation sites of the same orientation as the subst rate and promotes lateral growth of the GaN film. This affect occurs due to the decrease in interfacial free energy between film and substrate.

Zinc Oxide (ZnO)

ZnO is a wide band-gap II-VI semiconductor (E_g = 3.37 eV) with piezoelectric properties. ZnO thin films have been used in a variety of commercial applications, including light emitting diodes [36], photodetectors [37], solar cells [38] and surface acoustic wave filters [39]. However, ZnO has recently been investigated as a possible compliant layer for GaN on Si due to its small lattice miss-match to GaN (1.8) and its hexagonal wurtzite structure. Table 2.10 below shows the lattice constants for wurtzite ZnO.

Table 2.10. Lattice constants for wurtzite ZnO

Wurtzite			
a (Å)	*c (Å)*	*c/a*	*u*
3.2496	5.2042	1.6018	0.3819
3.2501	5.2071	1.6021	0.3817
3.2860	5.2410	1.5950	0.3830
3.2498	5.2066	1.6021	
3.2475	5.2075	1.6035	
3.2497	5.206	1.6020	
		1.5930	0.3856
		1.6000	0.3830

ZnO thin films have been grown by a variety of techniques, such as radiofrequency or magnetron sputtering [40], spray pyrolysis [41], MBE [42] and MOCVD [43]. Early work on ZnO growth used RF magnetron sputtering because of the relatively low cost of the procedure and the low temperatures involved. This usually involved growth carried out with

$O_2/Ar+O_2$ ratios in the range of 0 to 1 under pressures of 10^{-3} to 10^{-2} Torr. In this process, the argon acts as the sputtering enhancing gas whilst the oxygen acts as the reactive gas. However, most of the ZnO films produced by this early work were polycrystalline or amorphous.

In the growth of ZnO films by MBE, metallic zinc and molecular oxygen are normally used as the source materials. An effusion cell of Zn metal is evaporated to produce the Zn flux and O is provided by a plasma source. A pressure of 10^{-5} Torr in the growth chamber is usual when using an O plasma source. In the past, nitrogen dioxide (NO_2) has been used as an alternative source. While NO_2 helps to maintain the chamber vacuum to protect sensitive filaments and heaters, it's used has resulted in generally poor quality ZnO films. Hydrogen peroxide (H_2O_2) is another alternative and has produced more promising results [44].

MOCVD-based deposition of ZnO usually employs metal alkyls such as dimethyl zinc [$(CH_3)_2Zn$] (DMZn) or diethyl zinc [$(C_2H_5)_2Zn$] (DEZn). These are combined with a separate O source (e.g. O_2 or H_2O) and an argon carrier gas [45]. Unfortunately, these particular precursor/oxygen combinations produce severe premature reactions in the gas phase. These reactions can lead to the formation of particulates that block up reactor inlet lines and degrade film quality. However, recent progress has been made to reduce these unwanted reactions by using alternative oxygen sources such as N_2O or NO_2 [46].

The majority of ZnO films deposited by these various growth techniques have been done so on Al_2O_3 substrates. Efforts are now being made to deposit on the more technologically viable substrate material Si.

Scandium Nitride (ScN)

ScN has been investigated as a compliant layer for GaN as it exhibits a rock-salt crystal structure with lattice parameters producing a very lattice mismatch of less than 0.1% with that of hexagonal GaN. ScN also has a reported melting point (T_m) in excess of 2600 °C which is desirable since as in the case of AlN it will not decompose within the temperature range for GaN growth. It also has direct band gap of 2.1-2.4 eV and an indirect gap of 0.9±0.1 eV.

ScN has been grown by a variety of methods such as chemical vapor deposition [47], magnetron sputtering [48] and molecular beam epitaxy [49], although deposition by the latter technique has been reported in only a limited number of studies. Moustakas *et al* [50] reported the deposition of ScN on Al_2O_3 using cyclotron resonance MBE producing a polycrystalline film with a preferred [111] orientation. Most attempts to deposit ScN have employed Al_2O_3, MgO and quartz substrates. When Si substrates have been used low crystallinity of ScN has been reported [52]. Steps have been taken to try and overcome this problem so that quality ScN can be deposited on this technologically important substrate.

2.5 Applications for III-N Semiconductors

Group III-N materials have been actively developed for semiconductor devices since the early 1970's, when the successful commercialization of light emitting diodes (LED's) and laser diodes (LD's) caused a surge of interest and development for III-N/GaN, based devices. Materials such as GaN, AlN and InN are ideal candidates for optical devices because they can form continuous alloy systems (e.g. InGaN, AlGaN) with direct optical band-gaps that range from 1.9 to 6.2 eV. Other advantageous properties of these materials include high mechanical and thermal stability. In combination these attributes lend themselves to the successful development and production of devices, such as control systems in the electrical sub-systems of automobiles, ships and aircraft, power microwave devices in radar, satellite and wireless base stations, photodetectors for solar-blind UV detection and many more. A brief outline of some of these devices will be explained further in the following sections.

2.5.1 Light Emitting Diodes (LEDs)

The 1960's saw the very first semiconductor LED using the material GaAs[4]. This was followed by a flourish of further developments, which gave rise to devices such as infrared LED's and other visible range emitting devices. For example AlGaAs was used for red, GaP for green and GaAsP for red/yellow. The development of the blue LED proved to be a slightly more arduous task due to a combination of factors. However after many years of development high efficiency blue and green

LEDs have now been achieved. Table 2.11 shows the efficiency and brightness of LEDs prior to the advent of these modern LEDs.

Table 2.11 Efficiency and brightness of LED's prior to the modern LED

Semiconductor	*Colour*	*Efficiency (%)*	*Brightness (mcd)*
AlGaAs	Red	15	2000
GaP	Green	0.15	200
SiC	Blue	0.12	15

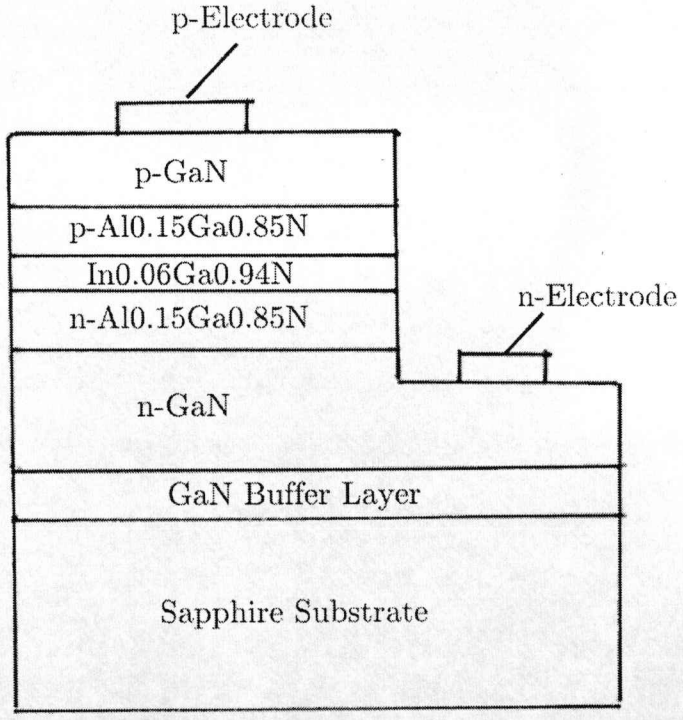

Figure 2.8 Schematic diagram of the first high brightness LED

Nakamura *et al* [50] produced blue LEDs with and efficiency of around 9% and 6% at 450nm and 520nm emission wavelengths. Figure 2.8 shows a schematic diagram of one of Nakamura's blue LED. This type of LED consists of an $In_{0.06}Ga_{0.94}N$ active layer that is doped with Si and Zn that is sandwiched between p- and n-doped $Al_{0.15}Ga_{0.85}N$ confining layers. At room temperature the barrier height is in excess of 10kT. The diode uses a Ti/Al ohmic contact for the n-GaN layer and a Ni/Au contact for the p-GaN layer. Since a sapphire substrate was used, it has to be etched down to the n-GaN layer in order to make the back electrical contact. It was reported that the diodes had good current-voltage characteristics and a linear light-current of up to 20mA with a current density of around $20Acm^{-2}$. At this current density the voltage drop at the p-contact decreased to below 0.1V and the light power was 3mW for the blue emission (450nm). For a purer blue light to be produced a thinner quantum well is needed and a larger In fraction. To achieve this, Nakamura used a 20A quantum well placed between two-step barriers of one 500Å barrier of $In_{0.05}Ga_{0.95}N$ and one 1000Å barrier of $Al_{10.1}Ga_{0.9}N$. All of Nakamura's LEDs were grown by MOVPE. By comparison the efficiency of LEDs produced by other researchers using deposition techniques, such as MBE, has been relatively poor [54].

2.5.2 Light Diodes (LD's)

LD's are very similar in construction to the LED's described in the previous section. At this present time of research the main aim is the

realization of short wavelength diodes, which operate near the UV-spectral range. In order for lasing to occur and therefore stimulated emission, there must be a very large number of excited electrons and holes present. This means that a p and n-type junction must be present, where each p and n-type material are heavily doped so that their Fermi levels lie within the valence or conduction band. A voltage close to that of the energy gap voltage E_g/eV then forward biases the p-n junction. A population inversion is then formed in a region coined the *active region* that is typically around 1-3μm and were an excited atom spontaneously emits a photon. When the injected carrier concentration is large enough the stimulated emission can exceed absorption and lasing occurs when round trip gain exceeds the losses over the same distances.

There are four main types of LD's these being; double heterostructure lasers (DH), quantum well lasers (QW), separate confinement heterostructure lasers (SCH) and vertical-cavity surface-emitting lasers (VCSEL's). A detailed description of these LD's is beyond the scope of this study but brief summaries are presented below.

DH lasers contain a low bad gap material sandwiched between two high band gap materials for example GaAs and $Al_xGa_{(1-x)}As$. QW lasers have a very thin material between the p and n junction, which acts as a quantum well. The efficiency of a quantum laser is much greater than the average bulk laser due to the density of states function of electrons in the quantum well having an abrupt edge that concentrates electrons in energy states that contribute to laser action. SCH lasers are simply a

more advanced version of a QW laser were two layers are added onto a simple QW laser to confine the light effectively. This is done because the added layers have a lower refractive index than the central layers. Finally VCSEL lasers have the optical cavity axis along the direction of current flow rather than perpendicular to the current flow as in the other types of lasers. The active region length is very short compared with the lateral dimensions so that the radiation emerges from the surface of the cavity rather than from its edge.

2.5.3 Micro-electric-mechanical devices (MEMs)

Devices, which incorporate either an electrical or an optical transduction technique, can be classified as a micro-electric-mechanical system. MEMs integrate sensors, actuators, and electronics with silicon substrates by micro-fabrication technologies. They are utilized in many industrial applications such as accelerometers in automobiles, pressure sensors, inkjet printers and high-precision optics. Figure 2.9 shows a schematic representation of piezoelectric accelerometer, used in crash sensors and a piezoelectric charge amplifier circuit.

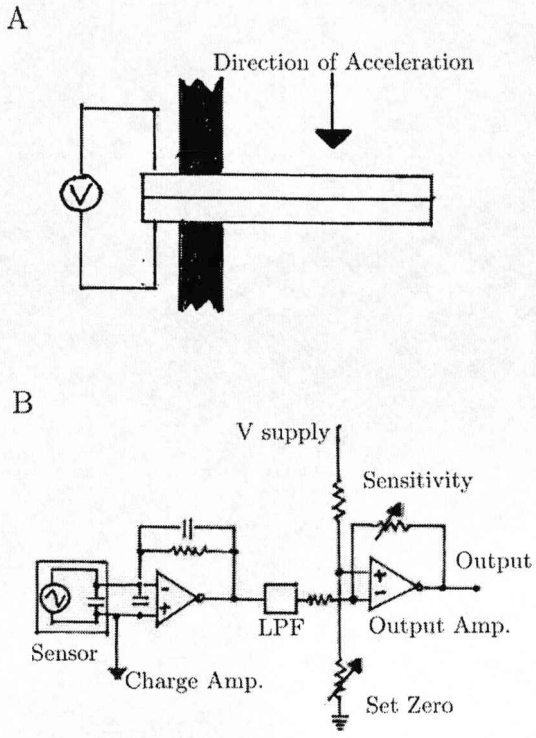

Figure 2.9 Micro-electric-mechanical devices, upper showing a piezoelectric accelerometer and lower showing a piezoelectric charge amplifier

The piezoelectric accelerometer (a) consists of two piezoelectric slabs of opposite polarity and has a bimorph structure. Once the sensor is accelerated it causes one slab to be placed under tension and the other under compression. These stresses cause a reverse polarity and leads to the creation of a signal doubling effect. For the charge amplifier (b) a signal is passed through and this converts the signal into voltage. When passed through a low-pass filter (LPF) the signal is adjusted for offset and sensitivity during further amplification.

One of the main disadvantages of piezoelectric sensors is that they are

sensitive to load and electromagnetic interference. Their high output impedance causes this. However piezoelectric sensors can operate at temperatures up to 300°C and also have a high operating frequency of around 100kHz. There are many other MEM devices than the ones mentioned here such as, piezoresitive sensors, electrothermal actuators and capacitive sensors. These have been extensively reviewed elsewhere [62].

2.6 Summary

This chapter has reviewed some of the rational for depositing III-N materials onto silicon substrates. The crystal structures and physical properties of these materials have been discussed, along with an introduction to some of the growth techniques used to deposit GaN and other III-V materials. A review of previous developments of substrates and compliant layers for the growth of epitaxial GaN has been presented. Some potential compliant layer materials such as the rare-earth aluminates have also been considered. Finally a brief overview of some of the applications for the III-N semiconductors is made.

References:

1 J. K. Sheu, C. J. Pan, G. C. Chi, C. H. Kuo, L. W. Wu, C. H. Chen, S. J. Chang, and Y. K. Su. IEEE Photonics technology letters. (2002) 1041-1135

2 S Pal and C Jacob. Bull. Mater. Sci. Vol. 27 6 (2004) 501–504

3 Liu L. and Edgar J.H. 2002 *Material Science and Engineering. R* **37** 61.

4 Orton J.W. and Foxon C.T. 1998 *Rep. Prog. Phys.* **61**.1.

5 Wu.J, Yaguchi. H, Onabe. K and Shairaki Y. 1998 *Appl.Phy.Lett.* **73** 193.

6 Dadgar. A, Pochenrider. M, Blasing. J, Fehse.K, Diez.A, and Krost.A. 2002 *Appl.Phy.Lett.* **80** 3670.

7 Degera,C. Born,E. Angerer,H. Ambacher, O. Stutzmann, M. Hornsteiner, J. Riha, E and Fischerauer, G. 1998 *Appl. Phys. Lett.* **72** 2400.

8 Gleize,J. Demangot. F. Frandon. J. Renucci M.A, Widmann. F and Daudin. B 1999 *Appl.Phy.Lett.* 74 703.

9 Manasevit H M 1968 *Appl. Phys. Lett.* **12** 156

10 Zang KY, Wang LS, Chua SJ, Thompson CV, Journal of Crystal Growth, 268 (3-4) (2004) 515-520

11 H. Seki, H.Eguchi, H.Kobayashi. Journal of Crystal Growth. Volumes **24-25** (1974) 225-228

12 Shintaro Miyazawa, Yasunobu Ishii, Satoru Ishida, and Yasushi Nanishi, Appl. Phys. Lett. **43** 853 (1983)

13 Dupuis RD, Journal of Crystal Growth 55 (1) (1981) 213-222

14 Morisaki M, Ogura M, Hase N, Kajiwara T, Electronics Letters 21 (4) (1985) 164-165

15 H.M. Manasevit, EM. Erdman and W.I. Simpson, J. Electrochem. Soc. **118** (1971) 1864.

16 H. Amano, I Akasaki, K.Hiramatsu, N.Koide and N.Sawaki. Thin Solid Films **163** (1988) 1156.

17 S.Nakamura. Japan. J.Appl.Phys. **30** (1991) L1705.

18 H.Cho, C.Vartuli, S.M.Donovan, C.R.Abernathy, S.J.Pearton, R.J.Shul and C.Constantine. J. Vac. Sci. Technol A **16** (1998) 1631.

19 J.W.Yang, J.N.Kuznia, Q.C.Chen, M.A.Khan, T.George, M.DeGraef and S.Mahajan. Appl. Phy. Lett. **67** (1995) 3759

20 I.V.Markov. Crystal Growth for beginners. World Scientific Publishing Company 2nd edition (2004) ISBN-10: 9812382453

21 F.A.Ponce Group III Nitride Semiconductor Compounds (Oxford University Press)p 123 (1998)

22 J.E.Van Nostrand, J.Solomon, A.Saxler, Q.H.Xie, D.C. Reynolds and D.C.Look. J.Appl.Phy. **87** (2000) 8766

23 M. Tanaka, S. Nakahata, K. Sogabe, H. Nakata, M. Tobioka, Jpn. J. Appl. Phys. 36 (1997) L1062.

24 J.Pankove, S.Bloom and G.Harbeke. RCA Rev. **36** (1975) 163

25 Etzkorn.E and Clarke D.R. 2001 *J.Appl.Phys.* **89**. 1025.

26 Tripathy.S. Soni. R.K. Asahu.H. Iwata.K. Kuroiwa.R. Asami.K. and Gonda.S. 1999. *J.Appl. Phys.* **85**. 8386.

27 V.Kirchner, R.Ebel, R.Heinke, S.Einfeldt, D.Homel, H.Selke and P.L.Ryder. Mater.Sci.Eng. B **59** (1999) 47

28 A. Hanser, R.F.Davis. Properties, Processing and Applications of Gallium Nitride and Related Semiconductors INSPEC (Stevenage, UK: The institution of electrical engineers) p 386 (1999)

29 Gith. J and Petusky. W.T. 1987 *J. Phys. Chem. Solids.* 48. 541.

30 Tairov. Y.M and Tsvetkov. V.F. 1978 *J.Cryst.Growth.* **43**. 209.

31 V.Lebedev, J.Jinscheck, U.Kaiser, B.Schoroter, W.Richter and J.Kraublich. Appl. Phys.Lett. **76** 15 (200) 2029

32 Motorola patent. J.M.Finder, K.Eisenbeiser, J.Ramdani, R. Droopad, W.J.Ooms Patent No. US655946 B1 2003]

33 Slack.G.A and McNelly.T.F. 1976. *J.Cryst.Growth.* **34**. 263

34 H.Amano, N.Sawaki, I.Akasaki and Y.Toyoda. Appl.Phys.Lett. 48 353 (1986)

35 X. Duan, Y. Huang, Y. Cui, J. Wang, C.M. Lieber, Nature, 409 (2001) 66.

36 S. Liang, H. Sheng, Y. Lin, Z. Hio, Y. Lu, H. Shen, J. Cryst. Growth, 225, (2001) 110.

37 N. Golego, S.A. Studenkin, M. Cocivera, J. Electrochem. Soc., 147 (2000) 1592.

38 N.W. Emanetoglu, C. Gorla, Y. Liu, S. Liang, Y. Lu, Mater. Sci. Semicond.Process., 2 (1999) 247.

39 T. Hata, T. Minamikawa, O. Morimoto, T. Hada, J. Cryst. Growth, 47 (1979) 171.

40 J. Aronovich, A. Oritiz, R.H. Bube, J. Vac. Sci. Technol., 16 (1979) 994.

41 X. Gu, M.A. Reschikov, A. Teke, D. Johnstone, H. Morkoç B. Nemeth, J. Nause, Appl. Phys. Lett.,84 (2004) 2268.

42 C.K. Lau, S.K. Tiku, K.M. Lakin, . Electrochem. Soc., 127 (1980) 1843.

43 F.T.J. Smith, Appl. Phys. Lett., 43 (1983) 1108.

44 R. Solanki, G.J. Collins, Appl. Phys. Lett., 42 (1983) 662.

45 J. P. Dismukes, W. M. Yim and V. S. Ban, *J. Cryst. Growth* **13-14**, (1972) p.365

46 T. D. Moustakas, R. J. Molnar and J. P. Dismukes, *ECS Proc. Vol.* **96-11**, (1996), p.197

47 D. Gall, I. Petrov, L. D. Madsen, J.-E. Sundgren, J. E. Greene, *J. Vac. Sci. Technol. A* **16** (1998), p.2411

48 G. G. Stoney, *Proc. R. Soc. Lond.* **A82** (1909) p.172

49 S. Nakamura, M.Senoh, N.Iwasa and S.Nagahama. Appl.Phys.Lett. **67** (1995) 1868.

50 R.Molnar, R.Singh anf T.D.Moustakas. Appl. Phys. Lett. **66** (1995) 268

Chapter 3

Experimental Methods

As referred to in Chapter 2, several experimental techniques are available in order to deposit and characterise the nature and quality of epitaxial GaN layers and compliant layers. In this study, a multi-technique experimental set-up has been adopted in order to provide the best available range of information on film growth, the crystal structure and opto-electronic properties of the GaN over-layers and various compliant layers. Section 3.1 describes the deposition techniques, including information on basic theory and on the specific experimental set-up employed. Section 3.2 covers the various analytical techniques used to characterise the deposited thin films.

3.1 Growth Techniques

3.1.1 Metalorganic Chemical Vapour Deposition (MOCVD)

MOCVD has been utilized in the manufacture of many high performance electronic devices. The inherent characteristics of the process make it ideally suited for growing multiple epitaxial layers, which are essential in new device technology. In general terms, MOCVD can be described as a technique for the deposition of multi-constituent films using one or more metal-organic compounds as the source for one of the constituents. In the deposition of epitaxial semiconductors specifically the compound source is a metal alkyl. In this growth process, one or more of the film components is transported to the reaction zone in the form of a metal

alkyl. The remaining constituents are usually transported in the form of hydrides.

$$RnM + XH\,n \longrightarrow MX + nRH \qquad \text{(equ.3.1)}$$

Table 3.1 shows some of the reactants used for the MOCVD of III-V semiconductors.

Table 3.1 Reactants used for the MOCVD of III-V semiconductors

Material	*Reactants*
AlAs	$TMAl\text{-}AsH_3$
AlN	$TMAl\text{-}NH_3$
GaAs	$TMGa\text{-}AsH_3$ $TEGa\text{-}AsH_3$ $DEGaCl\text{-}AsH_3$
GaN	$TMGa\text{-}NH_3$
GaP	$TMGa\text{-}PH_3$ $TEGa\text{-}PH_3$

The formation of the desired compound occurs via the thermal decomposition of the organometallics and hydrides and the subsequent recombination of the atomic or molecular species at or near to the heated substrate. The whole process is closely controlled by fixing the flow rates and therefore the partial pressures of various reactants with electronic mass flow controllers. The pyrolytic nature of the reaction requires only the substrate to be heated in order to ensure efficient deposition, thus

simplifying the temperature control. MOCVD techniques used in the laboratory can be scaled-up to produce epitaxial layers on a commercial scale. In addition, production volumes can be achieved since the technologies already exist for silicon-based materials. The basic MOCVD reactions for the growth of compound semiconductors can be grouped into three categories: (i) those involving organometallic compounds and hydrides, (ii) those involving strictly organometallic compounds and (iii) those with other metalorganic compounds such as chlorine substituted metal alkyls and co-ordination compounds.

In conventional MOCVD the metal-organic precursors are held in a stainless steel bubbler, which is equipped with a dip pipe and bellow-sealed valves. The bubblers are held in temperature-controlled baths in the range of -20°C to +40°C. The precursors are then transported into the reactor chamber by bubbling a carrier gas such as H_2 through the precursor, which is controlled by a mass flow controller (MFC). Conventional MOCVD reactors operate on the principle of "vent-run" whereby a vent line allows the flow of reactants to be stabilized before entering the reactor chamber. The draw-back to this type of MOCVD process is the need for the bubblers and inlet pipe work to be heated to temperatures of 150-200°C. Many metal organic precursors such as metal alkoxide or β-diketonate have insufficient thermal stability to withstand heating for long periods and decompose in the bubbler or in the inlet pipe-work leading to poor layer uniformity and reactor blockages. However, the problems of premature thermal decomposition associated with low volatility precursors can be largely overcome by the

use of liquid injection MOCVD, in which the precursor is dissolved in an inert solvent, usually an ether (eg. tetrahydrofuran) or a hydrocarbon (eg. heptane or nonane) [1] The precursor solution is held at room temperature until required in the MOCVD process, and this prevents the thermal decomposition of the precursor prior to use. The precursor solution is then delivered at a precisely controlled rate and quantity into a heated evaporator and transported by a carrier gas into the reactor zone. Separate precursor solutions can be used for the growth of multi-component oxides, but more usually a number of precursors are dissolved in an appropriate molar ratio in a single solution or "precursor cocktail".

In this study liquid injection MOCVD was employed to deposit some of the compliant layers and the two reactor configurations used in this work are outlined in the following sections.

Axitron 200FE Reactor

MOCVD reactors are generally designed to be either horizontal or vertical. One of the systems used to produce the samples at Liverpool is a horizontal Axitron 200 FE reactor for the growth of oxide materials. The reactor design is a state-of-the-art liquid injection MOCVD instrument in which a Trijet ® solvent injection delivery system is coupled to the horizontal flow CVD reactor, shown in Figure 3.1.

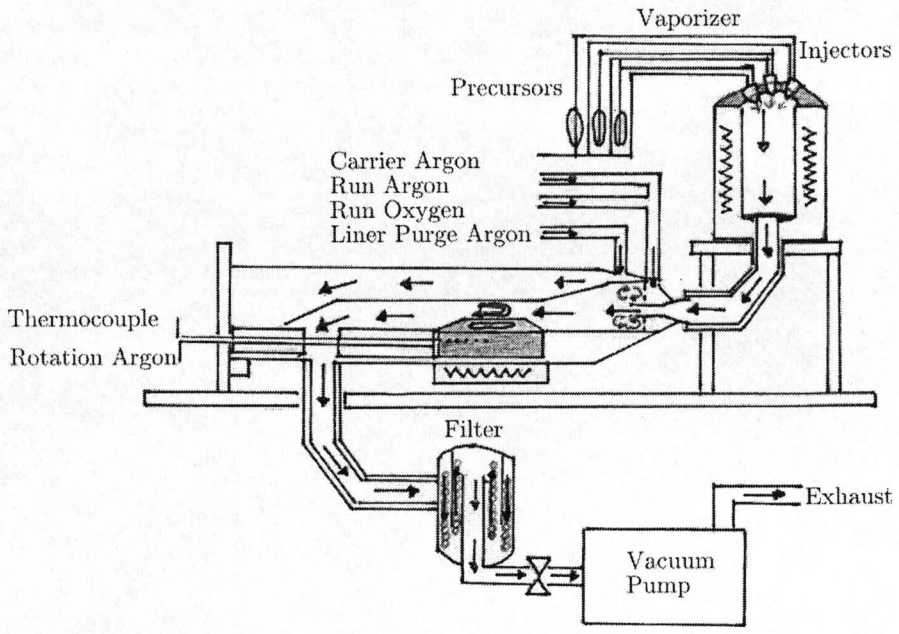

Figure 3.1 Aixtron 200FE liquid injection MOCVD reactor

A graphite rotary susceptor stage holds a 2-inch silicon wafer in the reactor chamber. Three separate liquid injectors feed a single vertically mounted vaporizer and this in turn feeds a horizontal quartz reactor chamber. Figure 3.1 shows a schematic representation of the whole system illustrating the main features and components.

A quartz lined cylindrical reactor chamber acts as the vacuum vessel containing an inner liner, which can be removed for cleaning and maintenance. Loading and unloading of the reactor is simple and straightforward by sliding the graphite stage in and out.

Precursors are dissolved or diluted in a carrier solvent, such as hexane or toluene. This allows pressurized liquid transport of the chemical from the glass bottle containers to the liquid injectors. The injectors are in effect miniature solenoid valves that gauge, dispense and spray precursor into the vaporizer in an accurate and controlled manner. The feed bottles and lines are held at room temperature to avoid the decomposition of thermally sensitive materials. The cylindrical vaporizer, approximately 40mm in diameter is stepped-in at the lower end and heated by embedded cartridge heaters. Thermocouples are used to control the five independent temperature zones. A Venturi mixing system allows oxygen and argon to be introduced into the reaction chamber. A susceptor graphite block supports a gas driven graphite rotary stage upon which the silicon (111) 2-inch wafer sits. A bank of five electrically tuneable infrared lamps heat the susceptor controlled by a thermocouple embedded inside the susceptor. Exhaust gases pass out of the reactor and through a water-cooled filter where non-volatile materials are condensed and subsequently vented through an externally vented duct. A five stage dry rotary pump with inter-stage cooling and nitrogen purge is used to establish the base pressure. The pressure is precisely controlled using a butterfly throttle valve and the vacuum monitored inside the reactor chamber using a Penning gauge.

A rotary substrate stage is used to ensure the even deposition of the films onto the wafer. Precursor depletion occurs due to deposition onto the wafer, susceptor and the reactor walls. This causes variation in the deposition rates along the axis of gas flow. The gas flows are individually controlled by mass flow controllers (MFCs) to give stable

and experimentally repeatable reactor flow conditions. The design ensures injector stability with precursor bottle pressure supplied by a MFC set up to continually purge to the exhaust. This avoids any pressure surges caused by valves opening or closing. Injector conditions, such as continuously open or pulsing, pulse duration, frequency and count along with other conditions such as temperature, pressure and flow are all controlled using CACE software. The injectors are usually run in pulsed mode due to the small volumes of precursor used. Running the vaporizer and injectors at precise temperatures controls premature solvent volatilization or condensation at the injector tip. To achieve thermal stability the temperature of the assembly is carefully controlled by a water-cooled jacket surrounding the injector. This arrangement is illustrated schematically in Figure 3.2. In addition, heated carrier gas could be introduced to the lower end of the injector assembly. The carrier gas subsequently passes the injector tip into the vaporizer via an array of fine holes angled to carry away the precursor spray.

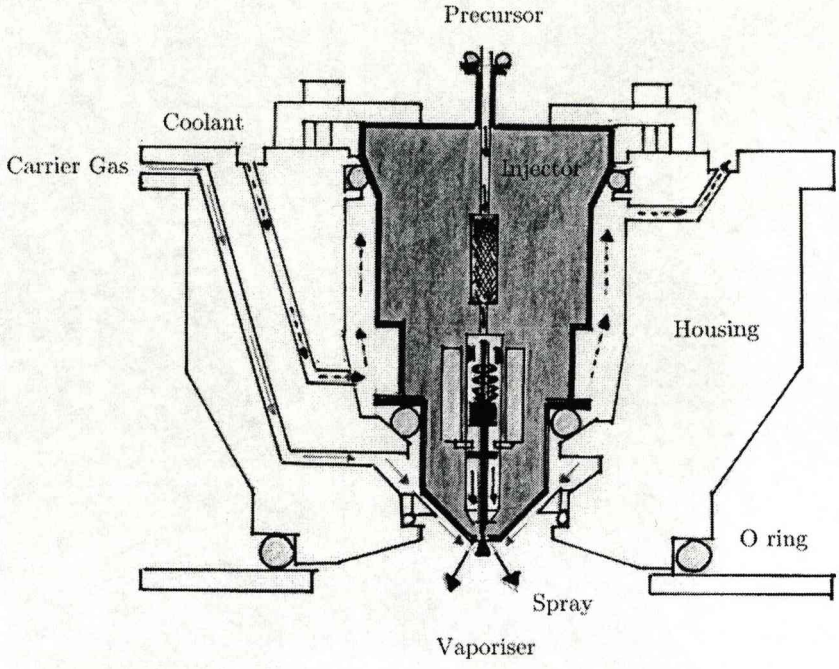

Figure 3.2 Section of liquid injector and housing (not to scale)

A 30nm thick non-removable filter embedded within the body of the injector is used to coarse-filter the incoming precursor. When the injector is actuated by a voltage across the solenoid coil, precursor is sprayed into the vaporizer due to compression of the internal spring. The spray pattern is improved by using a conical pin (pintle) positioned at the tip of the injector. The injector is opened by retracting the pintle upwards by about 100mm, breaking a metal-to-metal seal inside the injector body. Since machining tolerances have to be close for controlled operation of the injector, the parts in contact with the precursor are made of plastic or non-ferrous materials to minimise corrosion under normal operational conditions. This also reduces the incidence of blocking or sticking due to trapped particles of decomposed precursor. The outer body of the injector is ferrous based and so a corrosion inhibitor is required in the coolant.

Electrogas Reactor

The second reactor configuration used in this study is an Electrogas liquid injection reactor. This is a hand built machine that is used to screen MOCVD precursors. The Electrogas was used to deposit the LaN and ScN compliant layers in this work. However, before films could be deposited the reactor had to be reconfigured from an oxide to a nitride reactor. This entailed the porting of an ammonia gas line in through the reactor manifold system. So that the NH_3 could be handled safely an ammonia scrubber and detector system were also fitted to the exhaust system. Other minor modifications were required to the reactor geometry before nitride growth could be carried out.

The growth parameters used in the individual MOCVD deposition runs, employing both reactor configurations, are given in the relevant results and discussion chapters.

3.1.2 Molecular Beam Epitaxy (MBE)

MBE is essentially an ultra high vacuum (UHV) technique were neutral atomic and molecular beams from elemental effusion cells impinge with thermal velocities onto a heated substrate. The fact that MBE is a UHV growth technique means that this is a very clean process with very low impurity levels. MBE also lends itself to in situ analytical techniques, which is essential if the surface reaction kinetics of the deposition of thin films is to be understood.

The system employed in this study was a Polaron CVT TFS 4550. The modular two-chamber design allows simultaneous substrate introduction

and material deposition [2]. The deposition compartment consists of a 480nm internal diameter chamber, fabricated in stainless steel and a top flange that accommodates a double skinned liquid nitrogen cryoshroud (460mm OD X 380mm) and substrate manipulator. The deposition chamber is evacuated using a rotary pump and turbomolecular pump, which typically reaches a vacuum of $7x10^{-10}$ mbar after bake out. The pumping speed for this system is approximately 1600 l/s^{-1}.

In order to suppress contamination and to allow the substrate to be heated to > 100°C, the rotation and wafer heating stage is coated with pyrolytic-graphite. A W/Re type C thermocouple monitors the substrate temperature and a manual gate valve, VAT series 10NW 100 is used to isolate the deposition chamber from the load lock. The load lock is fabricated from stainless steel with an opening hinged door. An additional turbomolecular pump with a pumping speed of 70 l/s^{-1} is used to pump the load lock region to enable efficient transfer and access into the deposition chamber. This system is backed up using an oil-free diaphragm pump, allowing a vacuum pressure of < $5x10^{-8}$mbar. A Polaron CVT *Wafertrac*™ is used to transfer the wafers to the deposition chamber. This particular system employs a "rack and pinion" mechanism with no need for the usual wires or wobbles sticks.

Eight solid sources can be installed onto this MBE system, including standard effusion, high temperature effusion, cracker and gas sources. The Sc and La sources employed in this study are 30cc pBN crucibles with a maximum operating temperature of 1400flC. Hot/cold zones in

an ammonia atmosphere controls the temperature. The Gallium source is also a 30cc pBN crucible but with a maximum operating temperature of 1350°C. A dual filament source with special thermal gradient for operation in ammonia is used. Fast sinusoidal motion shutters operating at speeds of up to 100ms are used to control the flux from the crucibles. An EpiSoft ™ mass flow controller controls the ammonia gas flow and an EpiSoft ™ "tempframe" controller controls temperature. This controller allows both the temperature of the effusion cell and substrate heater to be regulated. An Epi CAD™ MBE deposition computer control package automatically converts growth characteristics into control parameters. For more details on the Polaron CVT TFS 4550 MBE system specification, see Davies 2000[2].

In this work, GaN was deposited on 2-inch Si (111) wafers in the CVT MBE system using an on surface cracking of ammonia as a source of nitrogen unless otherwise stated. Compliant layers of varying thicknesses were deposited employing this technique over a range of deposition temperatures. Further details of these experimental conditions are given in the subsequent results chapters.

3.2 Analytical techniques

3.2.1 Scanning Electron Microscopy (SEM)

A Hitatchi S-2460N Scanning Electron Microscope, operating at an accelerating voltage of 25kV, was used to investigate the surface micro-morphology of the oxide and nitride compliant layers along with the

surface topography of the GaN layers. Wafer sections were divided and mounted with conductive tape onto the goniometer stage of the microscope, enabling the samples to be examined in all directions. The instrument is fitted with an Energy Dispersive X-ray detector that allows elemental information to be acquired from the bulk of the sample. However, analysis of the resulting X-ray elemental information must be carried out with caution, since the penetration of the primary beam into the sample surface can be in the order of 1-2 μm. Due to the fact that the compliant layer and gallium nitride layers are considerably less in thickness than this range the X-ray information could be from several layers.

3.2.2 Energy Dispersive X-ray (EDX) Analysis

Elemental analysis is possible due to the unique characteristic X-ray emissions that occur from the inelastic interaction of the electron beam with individual atoms. This phenomenon arises when a high-energy beam electron penetrates and interacts with the inner shell electrons of the atom. During this interaction, if sufficient energy is transferred to one of these core electrons, the electron will be ejected leaving the atom in an excited state. In order to return to its ground state, the hole is filled by one of the outer shell electrons and this transition is accompanied by the emission of an X-ray. The energy of this emission is characteristic of the difference in energy of the two electron shells involved and thus is unique to the atom or element.

The X-rays emitted from a material are characteristic of the elements present and in the case of the thin films, peaks from the elements are generated. These peaks will be for all elements present including the substrate. Peaks that are present at certain characteristic energies indicate the presence of known elements and due to availability of many possible transitions from the sub-shells of each atom, a family of peaks on the energy spectrum may be used to infer the presence of an element. It is then possible through simple comparison of peak intensities to estimate the approximate elemental concentrations if similar transitions are considered eg. K_α N with K_α Ga.

3.2.3 Atomic Force Microscopy (AFM)

AFM was used to acquire information on the topography of the sample surfaces. The technique was used to evaluate the surface roughness (RMS) and any variation in the general topography of the thin film samples grown in this study.

The main advantage of AFM is that it offers sub-nanometre resolution without a long or expensive sample preparation period before investigation. AFM was derived from the scanning tunnelling microscope developed by Binnig et al [3] and overcomes the problem of using non-conducting samples. In this technique, a cantilever tip passes over the sample either in contact with or very near to the surface. Inter-atomic, frictional, magnetic and electrostatic forces deflect the tip when it is passed close to the surface. This allows the tip deflection to be measured and thus in turn generates an image. The tip may also be

lowered onto the sample surface to give contact mode AFM. In this case the tip is deflected by the contours of the sample and using direct surface height measurements a topographical image can be generated. A three dimensional graphical image is created by generating lines of equal force with the same contrast level. In contact mode, AFM allows atomic resolution providing that no background vibration is present. However contact-mode AFM can be physically damaging for softer samples.

A schematic representation of the Digital Instrument Nanoscope 3a atomic force microscope used in this study is provided in Figure 3.3. Contact mode was used for all the surfaces analysed in this study. The system used a 100-200μm long cantilever of approximately 2μm thickness and terminated in a sharp tip. The area was scanned using a slow raster, variable up to 5Hz (5 lines per second), to provide co-ordinates of features within an area up to a maximum of 100μm square.

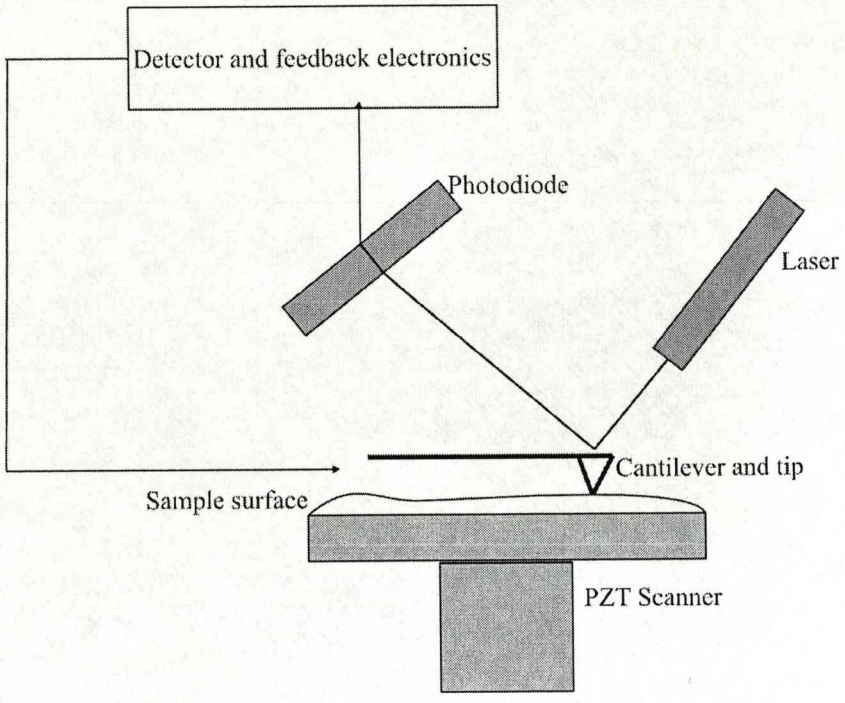

Figure 3.3 Schematic representation of AFM microscope

3.2.4 Raman Spectroscopy

The Raman effect is a term referring to the inelastic scattering of light by matter. When a photon of visible light that is too low in energy to excite an electronic transition interacts with a molecule, it can be scattered and therefore retains its incident energy. It can also be inelastically scattered by giving up or removing energy from the molecule. Photons that undergo inelastic loss of energy give rise to Stokes scattering and photons undergoing inelastic gain give rise to anti-Stokes scattering. The energy gained by the molecule in Stokes scattering appears as vibrational energy. Where a molecule has excess vibrational energy above the ground state the energy is lost to the anti-Stokes scattered photons (Figure 3.4).

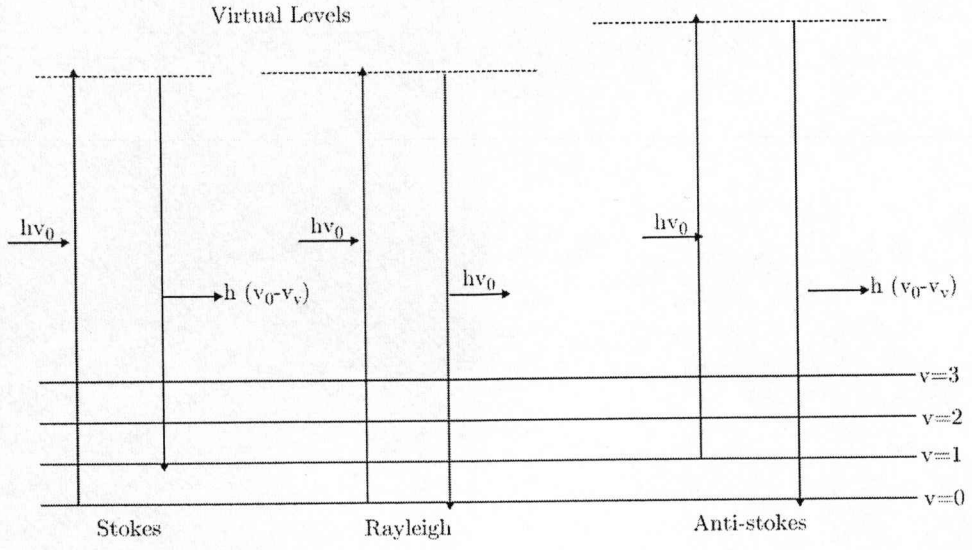

Figure 3.4 Idealised model of Rayleigh scattering and Stokes and anti-Stokes Raman scattering

The classical theory regards the scattering molecule as a collection of atoms undergoing simple harmonic vibrations and takes no account of quantisation of the vibrational energy. If a molecule is placed in an electric field, its electrons are displaced relative to its nuclei and therefore it develops an electric dipole moment. The induced dipole moment μ_i is proportional to the field strength ε in the case of small fields.

$$\mu_I = \alpha\varepsilon \qquad \text{(equ. 3.2)}$$

The proportionality constant α is the polarisability of the molecule. A fluctuating electric field produces a fluctuating dipole moment of the

same frequency. Electromagnetic radiation generates an electric field that can be expressed as:

$$\varepsilon = \varepsilon^0 \, \mathrm{Cos} 2\pi t \nu_0 \qquad \text{(equ.3.3)}$$

where ε^0 is the equilibrium field strength and ν_0 is the angular frequency of the radiation.

Rayleigh scattering arises from transitions that start and finish from the same vibrational energy level. Stokes Raman scattering arises from transitions, which start at the ground state vibrational energy level and finish at a higher vibrational energy level. Anti-Stokes Raman scattering involves a transition from a higher to a lower vibrational energy level. At room temperature, most molecular vibrations are in the ground, $\nu = 0$ state and therefore the anti-Stokes transitions are less likely to occur than the Stokes transitions. This results in the Stokes Raman scattering being more intense although it is not as intense as the Rayleigh scattering. A schematic diagram of a Raman system is provided in Figure 3.5.

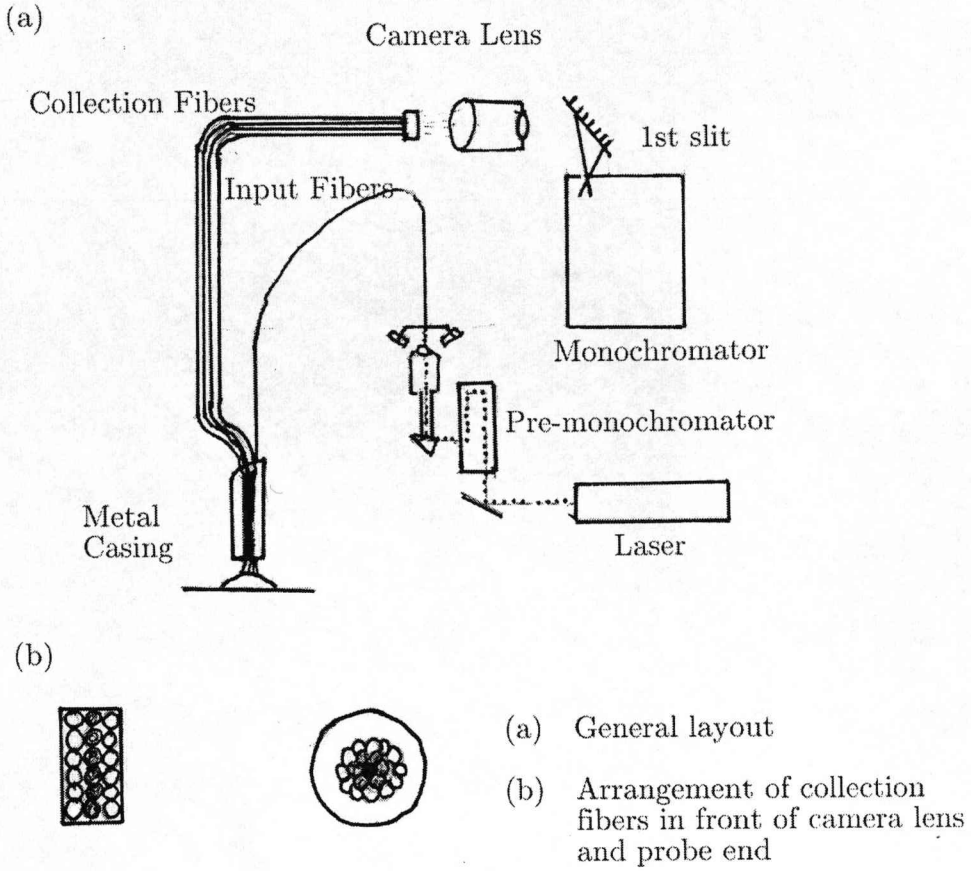

Figure 3.5 Schematic diagram of a fibre optic probe for Raman spectroscopy

The optical fibres can be used to focus the output from the laser beam into one end, typically 200μm in diameter. At the other end the emergent laser light illuminates the sample under analysis. The Raman signal is normally in the visible part of the spectrum, facilitating the collection of Raman scattered photons by one or more fibres placed close to the sample.

There are two types of laser that can be used as the light source for Raman Spectroscopy, these being continuous wave (CW) and pulsed.

The most widely used laser in Raman spectroscopy is the continuous wave laser that gives a continuous supply of photons. The first and still the most commonly used laser for Raman spectroscopy is the helium/neon laser, which lazes at 632.8nm. It is relatively cheap, very robust and is air-cooled. Argon and Krypton ion lasers are also used; the argon ion laser is most useful over the blue and green spectrum, whereas the krypton ion laser is most effective over the red and yellow regions of the spectrum.

Raman spectroscopy uses light scattered from the thin films to determine the chemical and phase composition and also resolves physical measurements, such as residual strain. In this study a Renishaw Compact System 100 was used. Measurements were carried out at room temperature, using a fibre optic probe instrument and employing an Argon ion (Ar^+) laser at 514.53nm. The spectrometer includes a holographic filter at a low angle of incidence acting as a beam splitter; this gave a beam incident power of ~15mW. Spectra were recorded in the back-scattered geometry, without any polarisation, using an x100 high numerical aperture objective lens, allowing a sampled area of ~100μm.

3.2.5 Transmission Electron Microscopy (TEM)

TEM was used to investigate the growth processes of the various grown layers. Specifically, TEM was used to observe the micro-morphology, thickness and lattice defects associated with the layers. Selective area

diffraction (SAD) was also employed in order to determine crystallographic information about the individual layers.

Two specimen preparation techniques were used to examine the thin film epilayers: thin films cross-section and plan view. The cross-section specimens were prepared conventionally along the [1 $\bar{1}$00] GaN projection, by gluing the cleavage sections face to face and mechanically thinning them to ~100μm, followed by dimpling to ~5μm in an ion beam miller. The samples were Ar^+ ion milled, at beam energy of 5 keV during the final stage to produce samples transparent enough for transmission electron microscopy. The TEM studies were carried out using a Jeol 2000 FX transmission electron microscope operating at 200 kV.

3.2.6 Dynamic Optical Reflectivity (DOR)

The DOR technique was used for the monitoring of in-situ growth rates of the heterostructures. The reflectivity of a growing epilayer has oscillations with a period equal to the epilayer thickness of $m\lambda/2n$ (where m is a positive integer, n is the refractive index of the film and λ is the free space wavelength). The apparatus consists of a laser light source (usually a He/Ne gas laser of λ equal to 632.8nm, or solid state laser diode of λ equal to 670nm) and a large area photodiode. The photodiode collects the reflected signal from the sample. The output is then analysed by a computer and transformed into a DOR spectrum of photodiode intensity versus time. At least one period of oscillation is required to determine the growth rate of the material. In these studies

DOR has been used to record the growth rate of III-nitride materials deposited by the MBE method.

3.2.7 X-ray Diffraction (XRD)

XRD spectroscopy was employed to determine the phase composition and crystallinity of the III-nitride/oxide samples grown by the MOCVD and MBE techniques. This technique is relatively sensitive and yields valuable atomic spacing and structural information for the thin films deposited.

X-ray diffraction spectroscopy utilizes the wave nature of electromagnetic radiation to generate constructive or destructive interference effects. Figure 3.6 provides a schematic representation of how two monochromatic parallel incident rays 1 and 2 strike and are diffracted by two adjacent layers of atoms separated by a distance d (termed the d-spacing). If the two exit rays 1and 2 are in phase it results in a high-amplitude wave. However, if the two rays are out of phase the resultant wave is of significantly lower energy. If the exit rays $1'$ and $2'$ are to be in phase and so constructively interfere, then the path length A-B-C must be equal to an integer multiple (1,2 etc) of the radiation wavelength used. The incident and exit angles q) must also be equal.

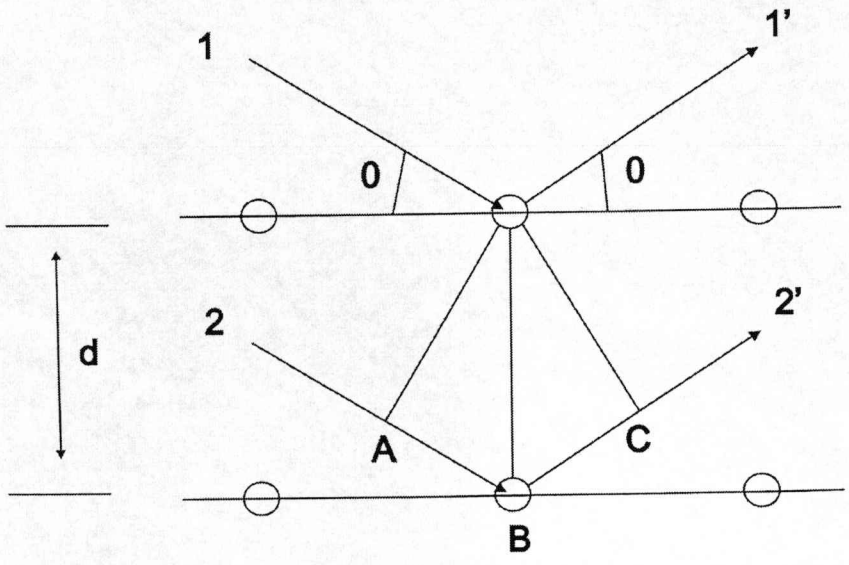

Figure 3.6 Geometry for X-ray diffraction

From the geometry of Figure 3.6 the extra distance travelled by ray 2-2′ compared with 1-1′ i.e. the distance A-B-C was first formulated by W.L. Bragg and is termed Bragg's Law (see equation 3.4).

$$n\lambda = 2d\sin\theta \qquad \text{(equ.3.4)}$$

Where n is the Integer, d Atomic spacing (Å) λ Radiation wavelength (Å) and θ is the diffraction angle (°)

The technique requires the wavelength used to be smaller than the d spacing, which is typically in the region of a few angstroms. To make this requirement X-rays are employed, which are generated from various

metal sources, e.g. molybdenum l = 0.709Å or copper l = 1.5405Å. The nature and inter-atomic d spacing of the material being studied determines the choice of wavelength.

All diffraction analyses conducted in the present study were carried out using a copper α- source. By detecting and plotting the intensity and angle of the exit rays it was possible to determine if the thin films had regular order i.e. crystalline. By comparing the data against standards it was possible to determine the structure and phase of the deposited films.

3.2.8 Medium energy ion scattering (MEIS)

MEIS is a refinement of the more commonly applied Rutherford back-scattering spectrometry (RBS) technique, but with enhanced depth and angle resolution. Its use is relatively new in the UK and the facility at the Daresbury Laboratory of the Council for the Central Laboratory of the Research Councils (CCLRC) was developed jointly by Warwick and Salford University and officially opened in 1996. Ion scattering using higher energies (up to about 2MeV) is termed High Energy Ion Scattering (HEIS) and is similar to MEIS, whilst Low Energy Ion Scattering (LEIS) is slightly different typically using alkali ions of a few keV.

In a typical MEIS experiment a collimated beam of mono-energetic (typically 100 keV) light ions (H^+ or He^+) impinges onto a target along a known direction. The energy and angle of the scattered ions are analysed

simultaneously, allowing MEIS measurements of atomic mass, depth, and surface structure from the following physical principles:

Mass: ions scattered from the surface of a material undergo energy loss by a 'billiard ball' type collision with surface atoms. The scattered ion energy relates directly to the mass of the scattering atom.

Depth: ions scattered from below the surface lose energy inelastically at a rate proportional to the ion's path length in the target. This extra energy loss relates directly to the depth of the scattering atom. In favorable cases, MEIS can achieve a depth resolution of one atomic layer.

Surface structure: when the ion beam is aligned with a crystallographic axis the surface atoms shadow deeper atoms from the ion beam. This alignment therefore makes the technique surface specific and, for a particular crystal, certain ingoing directions can allow the ion beam to illuminate only the top one, two, or three layers according to choice. Ions scattered from the second layer will have their outward paths blocked at certain angles by first layer atoms. The variation in the intensity of scattered ions with angle thus relates to the geometrical arrangement of surface atoms. A complete solution of surface structure requires a comparison between experiment and simulation for several scattering geometries. Figure 3.7(a) shows a schematic representation of the scattering geometry and the position of surface and near-surface atoms in which the surface atoms are shown relaxed outwards from the bulk positions. Figure 3.7 (b) shows the effect of this surface relaxation

on the MEIS blocking spectrum. The shift of blocking features to higher scattering angles indicates an outward relaxation. The degree of relaxation can be derived from the magnitude of the shift, either by geometrical calculation or computer simulation. By appropriate choice of scattering geometry, atomic displacements as small as ~0.03 can be measured.

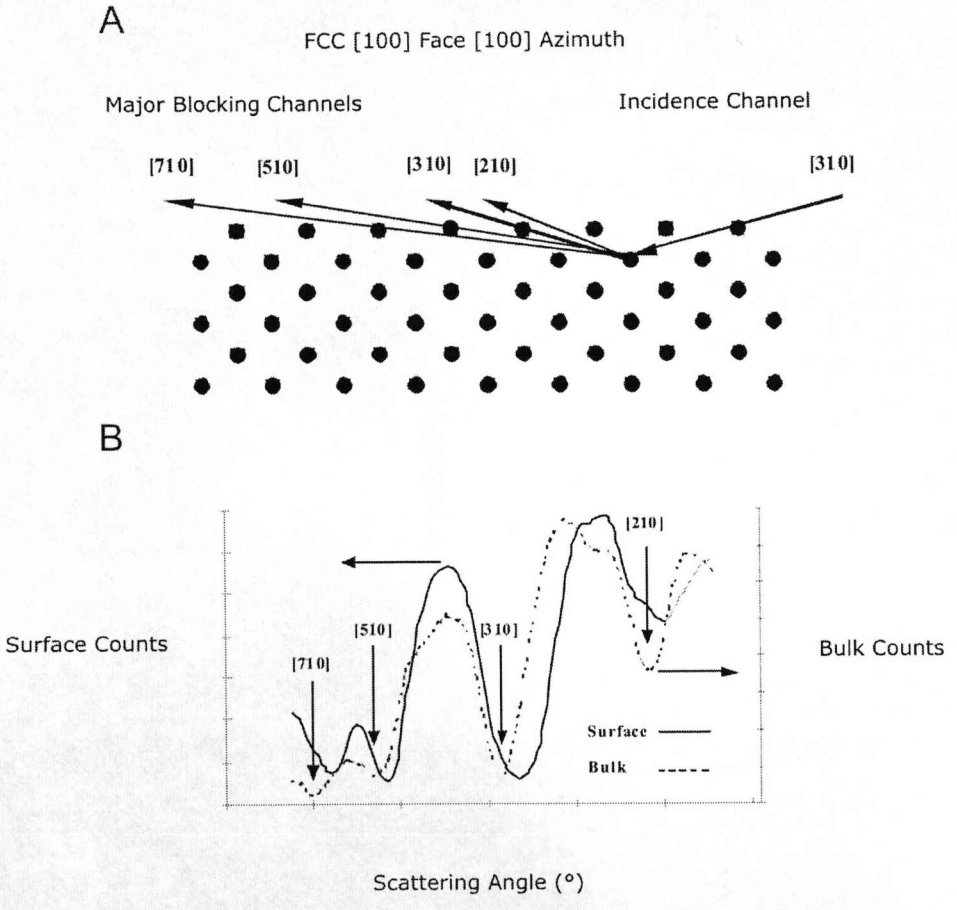

Figure 3.7 (a) MEIS surface scattering geometry and (b) Shift in MEIS features due to outward surface expansion

The ion source and beam line deliver a beam of mono-energetic, low-divergence (0.1°) ions into the scattering chamber and onto the sample. Scattered ions are analysed according to their energy and scattering angle by a Toroidal Electrostatic Analyser (TEA). The TEA uses the field created by positive and negative voltages to bend the scattered ions through 90 ° and onto a detector. To bend 100 keV ions requires ±6 kV across the TEA. Once bent through 90 °, analysed ions enter a detector assembly. The first component of the detector is a pair of channel plates which amplify (typical gain figure of 10^6) the tiny charge pulse generated by each ion.

The electron charge cloud produced by the channel plates impinges on a two-dimensional area detector which determines the position of the charge cloud and hence the energy and angle of the scattered ion. Measurement is achieved in two stages, firstly alignment of the beam with a particular crystallographic direction and secondly data taking. Sample alignment requires repeated scan and orientation changes of the sample to minimize the scattered ion count effectively lining up the layers of underlying atoms. The three axes of the goniometer are in turn scanned to produce a plot of the integrated counts that shows a minimum where some alignment is achieved.

Samples were initially aligned to detect the silicon substrate [111] crystal plane and surface normal. This was followed by rotation of 45° to align the incident ion beam along the [110] crystal plane, thus effectively

shadowing any silicon atoms below the first one or two layers. The other standard conditions used in the MEIS analysis are shown in Table 3.2.

Table 3.2 Standard conditions for MEIS analysis.

Parameter	*Value*
Ion source	He^+
Beam current	330 nA
Beam dimensions	Rectangular, 0.5mm high, 1mm wide
Substrate	Silicon [111]
Sample charge dose	2.5mC
Energy per pass	1.5%
TEA angle	28°
TEA range	160-40 keV

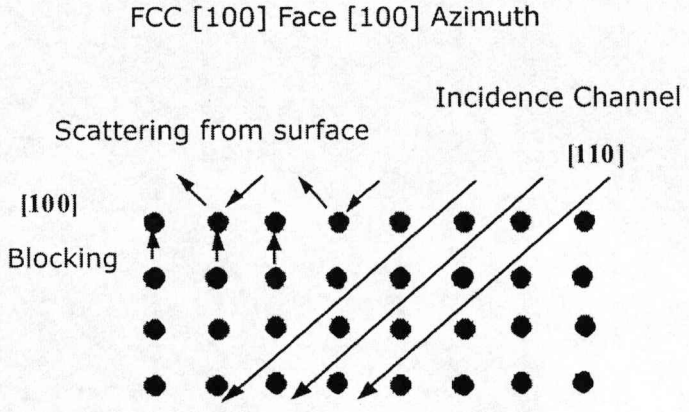

Figure 3.8 MEIS beam and sample alignment

The outlined set-up maximizes the system sensitivity to thin surface layers present on the substrate and minimises scattering from the crystalline silicon.

References:

1 A.C.Jones and P.O'Brien. CVD of Semiconductors: Preparation and Uses Wiley VCH (1 May 1997)

2 Davis.R. 2000 CVT TFS45500 MBE System (Polaron CVT Ltd.) 4506/RD.

3 G.Binning, C.F.Quate and Ch.Gerber. *Phys. Rev. Lett.* 56, 930 - 933 (1986)

4 P. Bailey, T.C.Q. Noakes, D.P. Woodruff, *Surface Science* 426, 358–372 (1999)

Chapter 4 Lanthanum and praseodymium aluminate

Overview

In this chapter the MOCVD and ALD deposition of $MAlO_3$ (M = La or Pr) is explored using a single-source alkoxide precursor $[MAl(OPr^i)_6(PriOH)]_2$. The resulting films are amorphous as -deposited and non-stoichiometric as established by AES. Annealing experiments indicate that the onset of crystallization occurs at between 750° and 850°C in air. After annealing, X-ray diffraction indicates the presence of polycrystalline perovskite phase on either Si(100) or Si(111) substrates. Capacitance-voltage measurements show that the permittivity of this materials is 13 ($LaAlO_3$) and 14 ($PrAlO_3$) at strong accumulation. The interaction between the metal aluminate and the silicon substrate is investigated using medium energy ion scattering. This reveals that inter-diffusion occurs at high temperatures which is consistent with the formation of interfacial silicates reported elsewhere in the literature.

Although epitaxial growth is not established, the growth of MBE gallium nitride on polycrystalline films of both lanthanum- and praseodymium aluminate has been investigated using in-situ annealing in an ammonia ambient. The growth of GaN is textured in the [0001] direction and the interface between the oxide and GaN is observed to be abrupt.

Chapter 4

Lanthanum and praseodymium aluminate

4.1 Background and rationale

In recent years there has been an increasing interest in materials with dielectric constants greater than SiO_2 (κ 3.9) as alternative gate dielectrics in integrated circuits. Researchers have also employed the same approach to integrate a range of functional materials with silicon. For example, Motorola have integrated ferroelectric and piezoelectric materials with silicon [1]. Their work employed a compliant layer of monocrystalline strontium titanate (STO) incorporating an amorphous layer at the interface of the silicon substrate. For a compliant layer to be truly successful it needs to meet two main criteria, namely its electrical properties and its lattice structure. A compliant layer needs to be lattice matched to both the underlying silicon substrate and the compound semiconductor thin film. In Motorola's work this was achieved using an amorphous layer of SiO_2, allowing the strain that arises from the silicon substrate and the STO to be dissipated. This enabled a high quality crystalline STO layer to be formed, which acted as an epi-substrate for deposition of a monocrystalline compound semiconductor layer, typically GaAs. To relieve strain in the STO layer further, a proportion of the film was laser annealed so that it became amorphous. This provided a true compliant layer for the subsequent deposition of a compound semiconductor.

In considering Motorola's work three limitations come to mind. Firstly the unwanted SiO_2 is still present in the system. Secondly the STO layer was deposited by MBE rather than the more suited MOCVD technique. Finally the benefit of a fully integrated process was not fulfilled due to the need for an additional heat treatment process to produce amorphous STO. In an attempt to overcome these limitations and improve the process, the COSMOS project indentified alternative oxides which could be deposited via CVD. Lanthanum aluminate ($LaAlO_3$) was chosen in this study as a potential compliant layer for the deposition of epitaxial GaN. This choice was based firstly on the lattice parameter of $LaAlO_3$ which has a value of a= 5.364 Å resulting in a small lattice mismatch of 1.3% with that of Si(111) [2]. Secondly, $LaAlO_3$ has also been highlighted as a possible candidate substrate for the deposition of epitaxial GaN [3]. Finally, $LaAlO_3$ is also stable in contact with Si and its low oxygen diffusion coefficient minimises formation of undesirable SiO_2 layers during the deposition of the aluminate. In its crystalline form $LaAlO_3$ has a layered perovskite-type structure with alternating Al-O_2 and La-O layers. However CVD $LaAlO_3$ layers are usually amorphous at temperatures of up to 900°C. This is because both La and Al have a valence of 3 and compete to occupy the same lattice site during growth, which results in an amorphous structure [4]. The following sections present the results of the work carried out to assess the use of $LaAlO_3$ as a compliant layer for the subsequent deposition of epitaxial GaN. In addition $LaAlO_3$ has also been investigated as a potential high-κ dielectric insulator for CMOS devices and DRAMS.

4.2 $LaAlO_3$ /Si (100)

Thin films of $LaAlO_3$ have been deposited using a variety of techniques such as pulsed laser deposition,[5-6] RF magnetron sputtering,[7-8] sol-gel processes,[9] spray pyrolysis,[10] spray combustion flame techniques,[11] metal organic chemical vapour deposition (MOCVD)[12-15] and atomic layer deposition.[16-18] As mentioned in chapter 2 the COSMOS project identified MOCVD as the deposition tool for this research, as it is most suited to current manufacturing methods in the semiconductor industry. A number of La and Al precursors have been previously used in MOCVD to deposit lanthanum aluminate. A combination of La and Al β-diketonate precursors such as [La(hfac)$_3$.diglyme] / [Al(acac)$_3$] (hfac = 1,1,1,5,5,5-hexafluoro-2,4-pentanedionate,acac=pentane-2,4dionate),[18-19] [La(thd)$_3$] / [Al(thd)$_3$],[14] (thd=2,2,6,6-tetramethylheptane-3,5-dionate) and [La(acac)$_3$] / [Al(acac)$_3$] have been employed.[12] However in this thesis a novel "single-source" alkoxide precursor [LaAl(OPr^i)6(Pr^{i}OH)]$_2$ was chosen (precursor supplied by Epichem Ltd.) . The advantages of using alkoxide precursors compared with β-diketonates includes lower deposition temperatures and reduced carbon contamination. Employing a "single-source" precursor has the further advantage that the metals are in the nominal ratio required to form a complex solid oxide. This potential for improved stoichiometry control is essential, as reactors frequently employ a single evaporator, which necessitates careful matching of precursor evaporation and deposition characteristics.

For an MOCVD precursor to be successful, it is important that it evaporates without premature decomposition at moderate temperatures, usually in the region of 300°C. The thermogravimetric analysis (TGA) data shown in Figure 4.1 demonstrates that this is the case for $[LaAl(OPr^i)_6(Pr^iOH)]_2$. The complex evaporates in the temperature range of 150°C – 300°C, leaving approximately 2% residue. A shoulder in the TGA curve can be clearly seen at 150°C-180°C. This can be attributed to loss of the weakly coordinating $[Pr^iOH]$ ligand in the complex.

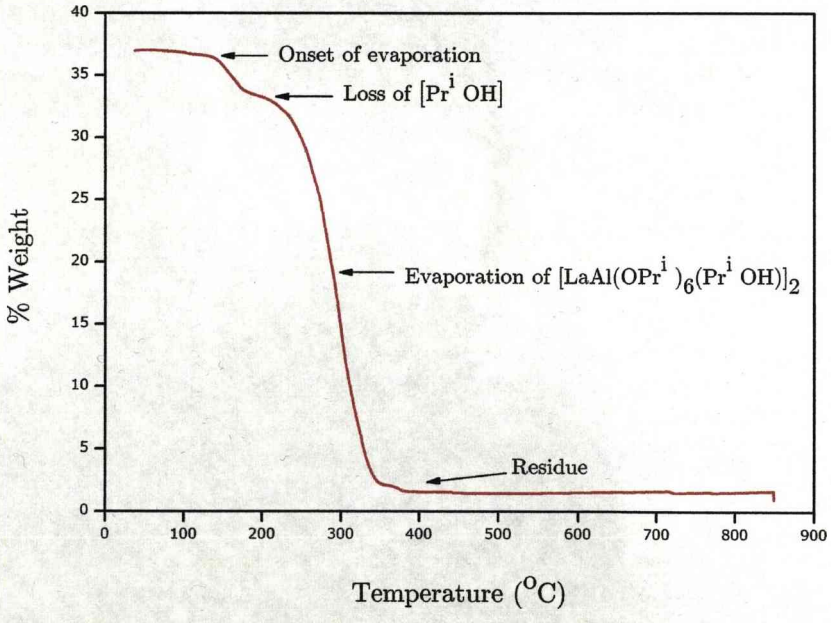

Figure 4.1 TGA data for $[LaAl(OPr^i)_6(Pr^iOH)]_2$, ($N_2$ atmosphere, 1atm).

Thin films of $LaAlO_x$ were deposited with varying thicknesses in the temperature range of 200°C – 600°C by liquid injection MOCVD and 160°C - 300°C by liquid injection ALD. Figure 4.2 shows the relationship between the growth temperature and growth rate of the $LaAlO_3$ for both the MOCVD- and ALD-grown films. The growth rates have been normalised with respect to moles of injected precursor to allow for a direct comparison between the two data sets.

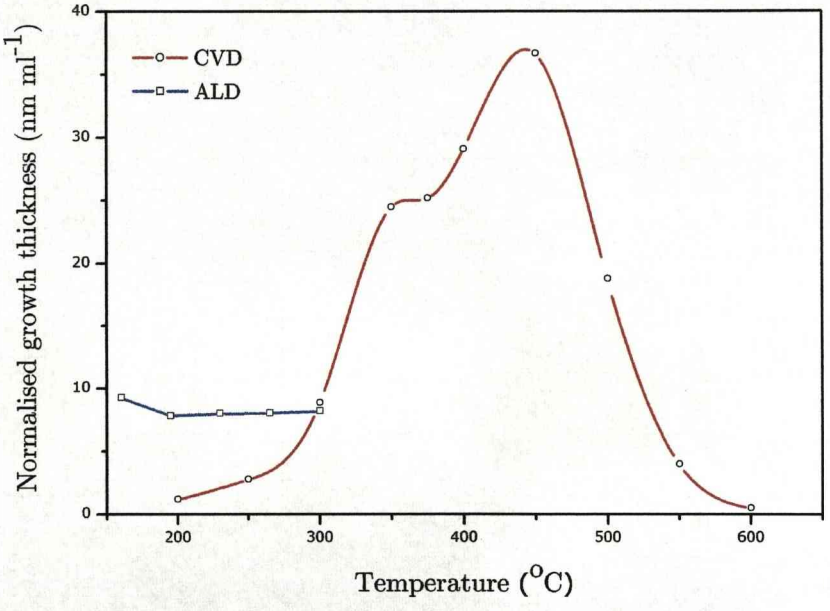

Figure 4.2. Variation of growth rate with substrate temperature for $LaAlO_3$ films grown using $[LaAl(OPr^i)_6(Pr^iOH)]_2$ by liquid injection MOCVD and ALD

Within the substrate temperature range of 200°C - 450°C, the MOCVD growth rate is seen to increase. This temperature range corresponds to the region of kinetic-control in which film growth is dominated by thermal decomposition of the precursor on the substrate and in the

boundary layer close to the substrate. The oxide growth rate reaches a maximum of 0.925 μm/ hr at ~ 450°C. At substrate temperatures of 450°C – 600°C however the oxide growth rate decreases rapidly due to thermal depletion of the precursor onto the reactor walls.

The growth rate of $LaAlO_x$ in ALD remains constant at ~ 0.035μm/hr over the temperature range 160°C – 300°C, indicating that the precursor is thermally stable up to 300°C. At substrate temperatures below 200°C, no growth was evident in the absence of water. The variation of oxide growth rate with precursor volume injected per ALD cycle is shown in Figure 4.3. In self-limiting ALD, the oxide growth rate per cycle would be expected to increase with increased injected precursor volume until surface-saturation is achieved [20] at which point the growth rate should become constant. In this case however, $LaAlO_x$ growth is clearly not self-limiting. This may be due to the surface decomposition of the [OPr^i] ligand, *via* elimination of a β-hydrogen. This would generate reactive surface [OH] sites, which would preclude self-limiting growth. Alternatively, the lack of self-limiting growth may also be due to the presence of residual adsorbed water inside the modified MOCVD reactor that had not been fully removed during the purge step.

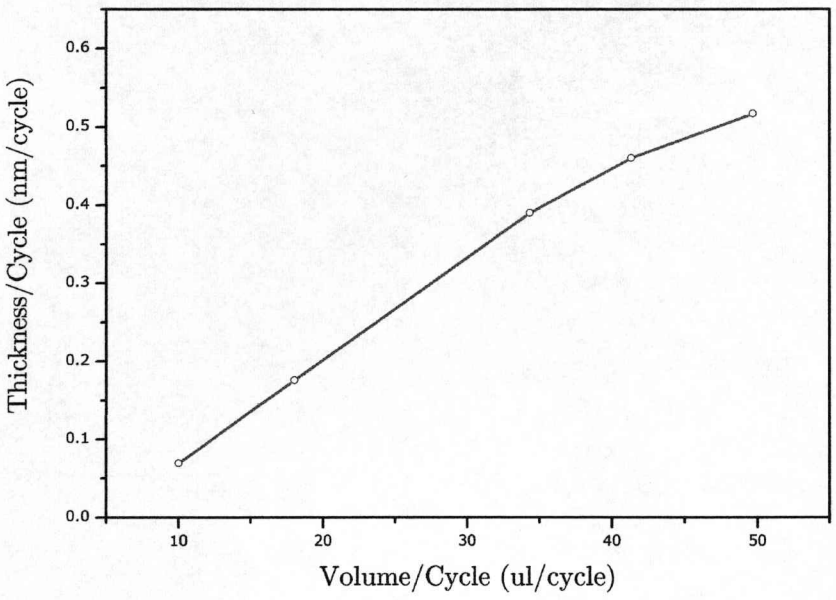

Figure 4.3. Variation of growth rate with precursor solution pulse length for $LaAlO_3$ films grown by liquid injection ALD using $[LaAl(OPr^i)_6(Pr^iOH)]_2$

The nominal composition (at%) of the $LaAlO_x$ films was determined by Auger Electron spectroscopy (AES) and the results are presented in Table 4.1. The results show that all the films are of high purity with no carbon detected. The estimated C detection limit is 0.5 at%. The La / Al ratio shows a marked variation with deposition temperature in the $LaAlO_x$ films grown by MOCVD. The samples grown in the temperature range of 200-375°C show an excess of La (ratios 1.25-2.60) whilst films grown above 450°C were relatively deficient in La (La/Al ~0.5-0.8). This trend is entirely consistent with earlier composition data (XPS) for $LaAlO_x$ films grown by MOCVD,[21] and may be due to thermal decomposition of the precursor in the gas-phase, leading to partial

separation of the La and Al components and pre-deposition of involatile La-oxide. A similar effect has been observed in $SrTa_2O_6$ films grown by liquid injection MOCVD using $[Sr\{Ta(OEt)_5(dmae)\}_2]$ where the films became Sr deficient at substrate temperatures above 400°C. The $LaAlO_x$ films grown at 300°C and 450°C are closest to the target 1:1:3 stoichiometry of $LaAlO_3$, with stoichiometries of $La_{1.1}Al_{0.89}O_3$ and $La_{0.92}Al_{1.1}O_3$, respectively.

The $LaAlO_x$ films grown by ALD are all La deficient, with the La/Al ratio varying from 0.50 – 0.61 over the growth temperature range of 160°C – 300°C. As gas phase reactions are negligible in ALD, the precursor is likely to remain intact until reaching the growth surface. It is therefore not surprising that there is little variation in the La / Al ratio, although the reason for the La deficiency in the films might be speculated that some La is lost via transport of a ligand complex.

Table 4.1. Auger electron spectroscopy data showing the composition (at%) of $LaAlO_x$ films deposited by liquid injection MOCVD and ALD using $[LaAl(OPr^i)_6(Pr^iOH)]_2$

	Sample	*Deposition temperature (°C)*	*La*	*Al*	*O*	*La /Al*
MOCVD	1	250	27.1	10.4	62.4	2.60
	2	300	22.2	17.9	60.0	1.24
	3	350	26.1	10.4	63.4	2.5
	4	350	27.8	10.7	61.5	2.6
	5	375	23.7	14.8	61.5	1.60
	6	450	18.5	22.6	58.9	0.82
	8	500	13.0	27.2	59.9	0.48
ALD	7	160	14.0	27.8	58.2	0.50
	8	180	13.1	24.2	62.7	0.54
	9	200	15.3	26.1	58.7	0.59
	10	300	14.5	23.6	61.9	0.61

Figure 4.4(a) shows a scanning electron micrograph of the as-grown films deposited by MOCVD below 450°C. In this range the morphology was generally uniform. The surface was essentially smooth and exhibited a featureless cross section. Additional topographical SEM investigation of films grown at 250°C by ALD (not shown here) demonstrated that the films had similar uniform and featureless morphologies.

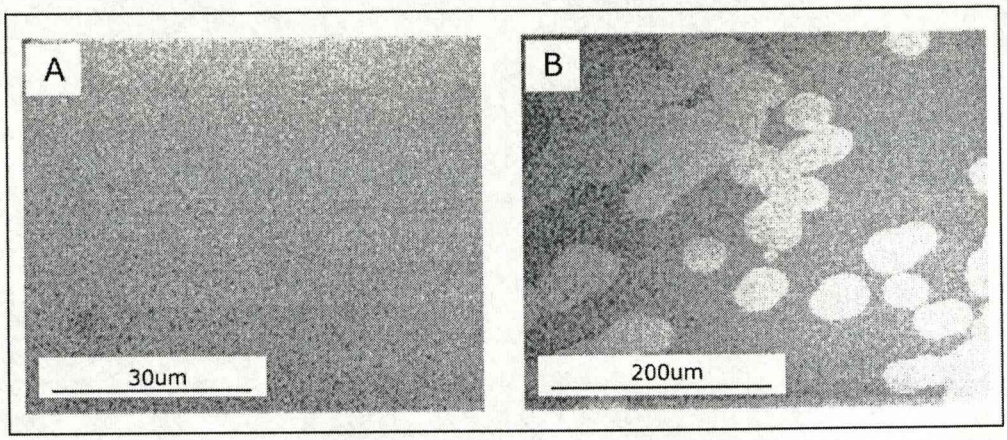

Figure 4.4 Scanning electron micrographs of: surface of lanthanum aluminate film grown by MOCVD at (a) 350°C and (b) surface of the same film after annealing in air at 850°C for 15 min

Subsequent annealing of a film grown at 350°C by MOCVD in air at 850°C for 15 minutes produced a surface which exhibited circular areas of lighter contrast as shown in figure 4.4(b). Energy dispersive X-ray analysis of these features showed no significant discernable change in composition compared with the surrounding film on the micrometer scale. However further investigation of the nanoscale compositional variation was made using medium energy ion scattering and is discussed in section 4.

Atomic force microscopy (AFM) was used to investigate the variation in nanostructure of these films after annealing. Figure 5(a) shows an AFM image of an MOCVD-grown film deposited at a growth temperature of 350°C. The surface roughness (rms) was estimated to be 0.840 nm. After annealing (Figure 4.5b) the rms value of 2.478 nm was recorded and significant roughening of the film was observed in addition to a

coarsening of the more particulate nanostructures observed on the surface. This was coupled with an increase in the 'rippling' microstructure of the film that contributes to the overall measured rugosity. A similar roughening effect was observed after annealing for ALD-grown films (T_g = 250°C) at 900°C in air for 15 minutes where the RMS value increased from 0.860 to 2.885 nm.

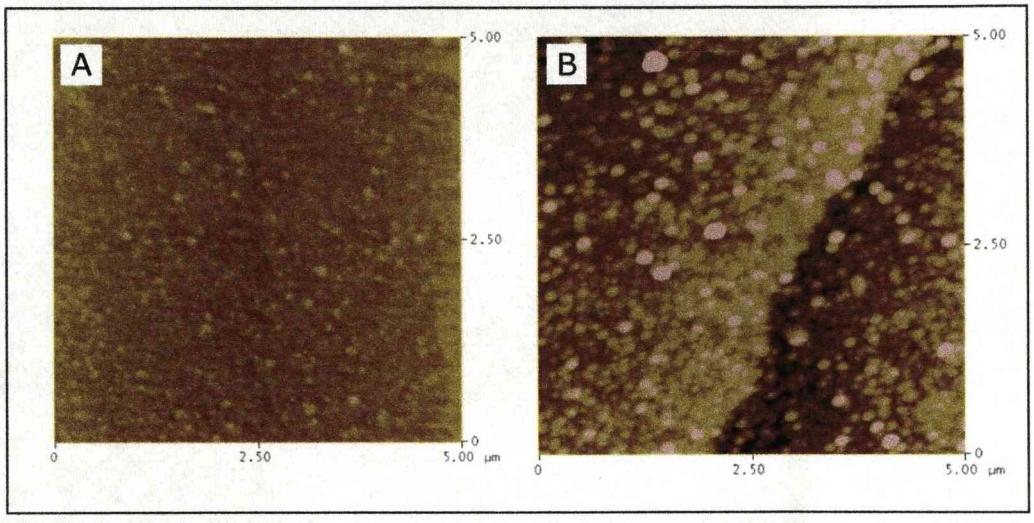

Figure 4.5 Atomic force micrographs of: (a) surface of lanthanum aluminate film grown by MOCVD at 350°C (R_{max} 28.3nm) and (b) surface of the same film after annealing in air at 850°C for 15 min (R_{max} 28.9nm)

In order to reduce electrical leakage currents and inhibit the formation of a low-κ interfacial layer during CMOS processing, it is desirable for a dielectric film to remain amorphous. This is because they must be thermodynamically stable to be compatible with present day process schemes (up to 1000°C for 5 seconds) [22]. To investigate thermodynamic stability, annealing studies were carried out in which films were

subjected to temperatures ranging from 750-900°C for 15 minutes. X-ray diffraction (XRD) analysis was used to determine the crystalline structure of the as-grown and annealed MOCVD films. Figure 4.6 shows the XRD pattern of a thicker $LaAlO_x$ film, (120nm) grown at a substrate temperature of 350°C. The sample was annealed in air over the temperature range of 750° to 900°C. The as-grown sample exhibits a broad background devoid of any crystalline diffraction features except for a peak at 33° arising from the (200) reflection from the Si(100) substrate.

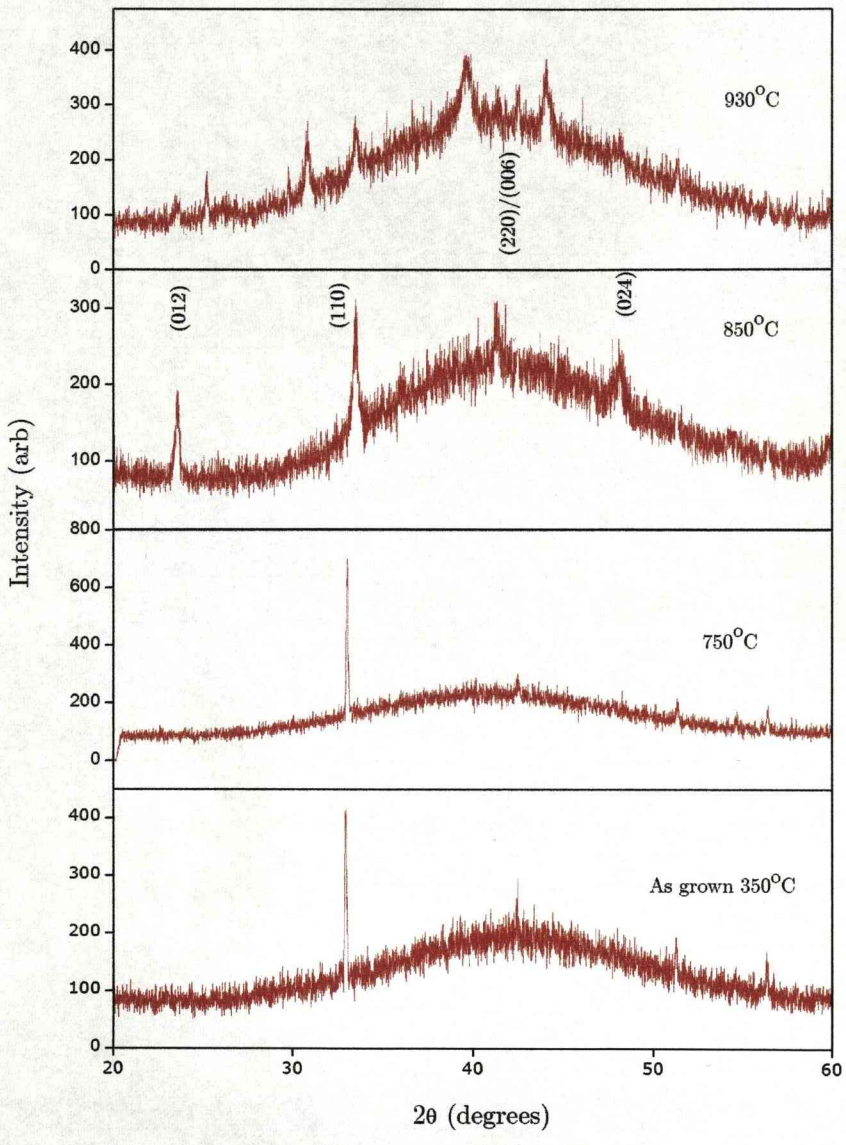

Figure 4.6 θ - 2θ X-ray diffraction data for a $LaAlO_x$ film (La/Al = 2.6) grown by MOCVD at a substrate temperature of 350°C and then annealed in air at 750°, 850° and 930°C (Substrate Si (100))

Annealing at 750°C did not significantly alter the diffraction pattern of the amorphous-like thin film. However, annealing at the higher

temperature of 850°C resulted in a set of polycrystalline diffraction features attributed to the (012), (110), (220) and (024) reflections characteristic of the $LaAlO_3$ rhombohedral perovskite phase (JCPDS, 85-1071). After annealing at higher temperatures, the film consists of two or more different phases. At 930°C the X-ray diffraction features of an alumina – like phase (ICSD database, 99783) become apparent in addition to the perovskite related diffraction pattern. It is not clear whether this film is a mixed phase or whether the film becomes stratified into two separate layers. No heteroepitaxial orientation was observed with respect to the Si (100) substrate.

The ALD grown films were too thin for the practical use of XRD to effectively explore annealing effects. Instead, ion scattering experiments were employed to investigate the crystallisation of $LaAlO_3$ films during annealing and any inter-diffusion between the film and silicon substrate. This was done using medium energy ion scattering (MEIS) at the Daresbury CCLRC facility (described in chapter 3). A 200 keV He^+ ion beam was employed with a current of up to 200 nA and a dose per data set of 5 μC. The angle and energy of the scattered ions were determined using a state-of-the-art toroidal electrostatic energy analyzer with position-sensitive detector. This allows the simultaneous collection of ions from a 24° range of scattering angles and with a range of energies equal to 2% of the pass energy. Using the scattering geometry described, the mass of lanthanum (138.90 amu) is sufficiently greater than the other constituent elements to enable only the lanthanum depth distribution to be profiled without interference. Figure 4.7 shows the scattered ion

energy spectrum displayed as a function of annealing temperature. Due to the inelastic scattering processes that the scattered He^+ undergo as a function of depth below the sample surface, the energy distribution gives an effective depth profile of the target atoms. In this case, a La depth profile is obtained which clearly shows the thickness of the oxide film. After annealing above 850°C inter-diffusion between the $LaAlO_x$ film and the silicon substrate is observed, coincident with the onset of crystallisation. The interface between the lanthanum distribution within the film and the silicon (denoted by↓) diffuses progressively into the silicon. The same effect is seen in the aluminium distribution (also denoted by ↓) but the profile is overlaid by the silicon profile because of the similar atomic masses of the two elements (Al 26.98amu Si 28.08amu).

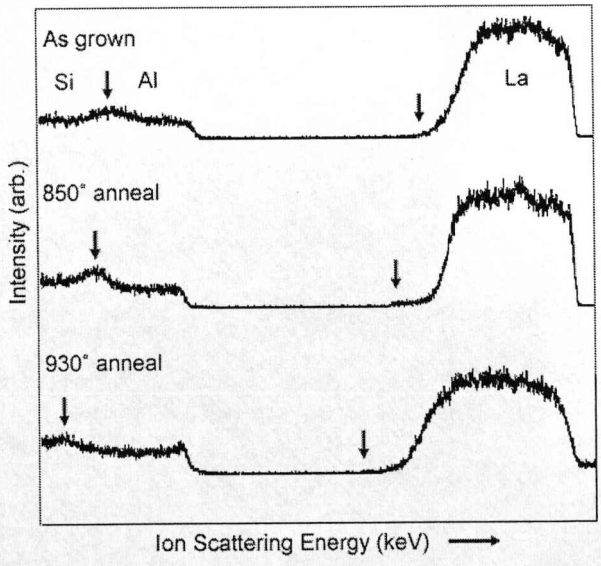

Figure 4.7 MEIS energy spectrum of a $LaAlO_x$ film showing the depth distributions of La, Al and Si as a function of annealing temperature. The arrows (↓) denote the interfaces of the La and Al distributions with the Si substrate

In summary, the experimental data shows that using the precursor $[LaAl(OPr^i)_6(Pr^iOH)]_2$ deposits $LaAlO_3$ films with low impurity content. Moreover, the smooth morphology and the high purity of the films suggest that they may be potential compliant layers for compound semiconductors, such as GaN, even though epitaxial recrystallisation was not achieved via simple air annealing. What follows is a set of experiments designed to determine the stability of GaN grown on $LaAlO_3$ thin films.

4.3 GaN/$LaAlO_3$/Si (111)

The previous sections considered the deposition of $LaAlO_3$ on Si(100) substrates. However, the prospect of wurtzitic GaN epitaxy is favoured by the use of substrates having six-fold rotational symmetry e.g. on Si(111). Westinghouse researchers were the first to demonstrate Si epitaxy on $LaAlO_3$(111) [23]. More recently, other groups have also been successful in depositing silicon on $LaAlO_3$ with an abrupt, reaction free interface [2].

There has been little previous work on the use of $LaAlO_3$ as a compliant layer for GaN epitaxy, which is surprising, as it possess many of the characteristics for a successful compliant layer. $LaAlO_3$ is hexagonal in structure, with a lattice constant of a= 3.793Å, giving rise to a lattice mismatch of around 3% with hexagonal GaN.

Although, the single-source precursor $[LaAl(OPr^i)_6(Pr^iOH)]_2$ did not readily form stoichiometric $LaAlO_3$ layers, it is nevertheless important to

determine the stability of the aluminate layer with respect to the Si substrate and GaN overlayer during exposure to nitride growth conditions. Therefore, films with stoichiometries close to 1:1 were selected for a subsequent investigation of the effects of gallium nitride deposition.

GaN layers were grown via molecular beam epitaxy (MBE) employing 'on-surface' ammonia cracking as a nitrogen source [24]. GaN films of thicknesses in the range of 80 to 100nm were deposited at a substrate temperature of 850°C. It was anticipated that in-situ annealing of the $LaAlO_3$ film in NH_3 during ramping to the nitride growth temperature would promote crystallisation of the amorphous aluminate layer to the required rhombohedral perovskite phase. Following this process, approximately 100nm of gallium nitride was deposited.

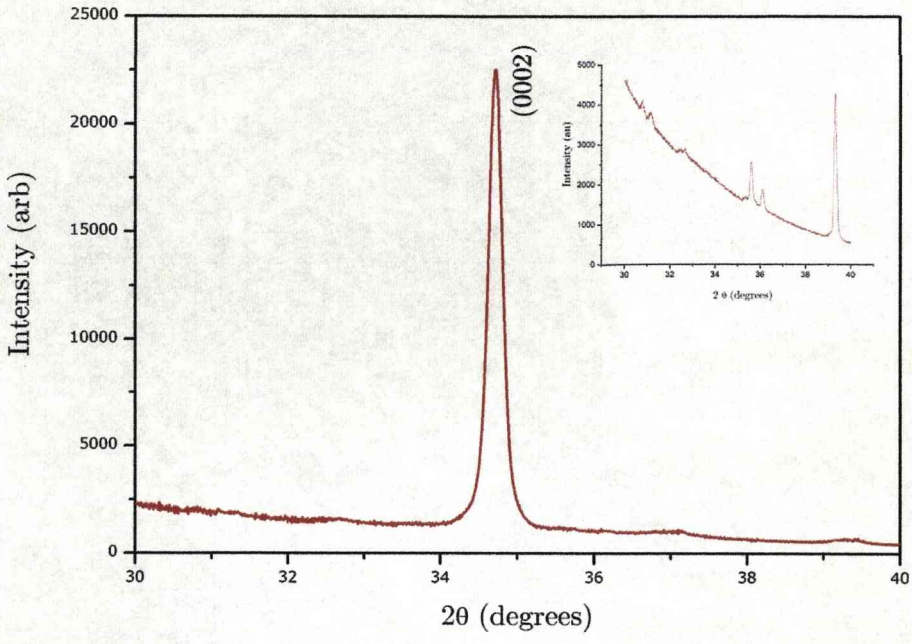

Figure 4.8 Θ - 2Θ X-ray diffraction data for GaN deposited on a MOCVD grown $LaAlO_3$ film

Figure 4.8 shows the X-ray diffraction analysis of a GaN/$LaAlO_3$/Si(111) sample where $LaAlO_3$ has a thickness of 17nm and the GaN 86nm. As the GaN(0002) diffraction feature occurs on the sharply decreasing intensity (inset) of the Si(111) peak at ~ 28° (2θ), the background has been subtracted.

The X-ray diffraction spectrum shows a predominant peak at 34.4° that corresponds to that of the 0002 peak of GaN. The nitride layer is clearly fibre textured along the c-axis of the crystal structure. The (0002) peak is coincident with the $LaAlO_3$ (110) reflection, which may contribute to the observed FWHM of 0.22° (792 arcsec). Hence, this strongly suggests

that the in-situ annealing has formed the desired perovskite phase for the $LaAlO_3$.

The SEM micrographs shown in Figure 4.9 illustrate the highly polycrystalline nature of the GaN layers. The columnar structure of the nitride, coupled with a relatively low nucleation density leads to a high density of pores in the layer. However, even at a thickness in the order of 100nm the GaN crystallites are beginning to show evidence of coalescence (marked by white arrows).

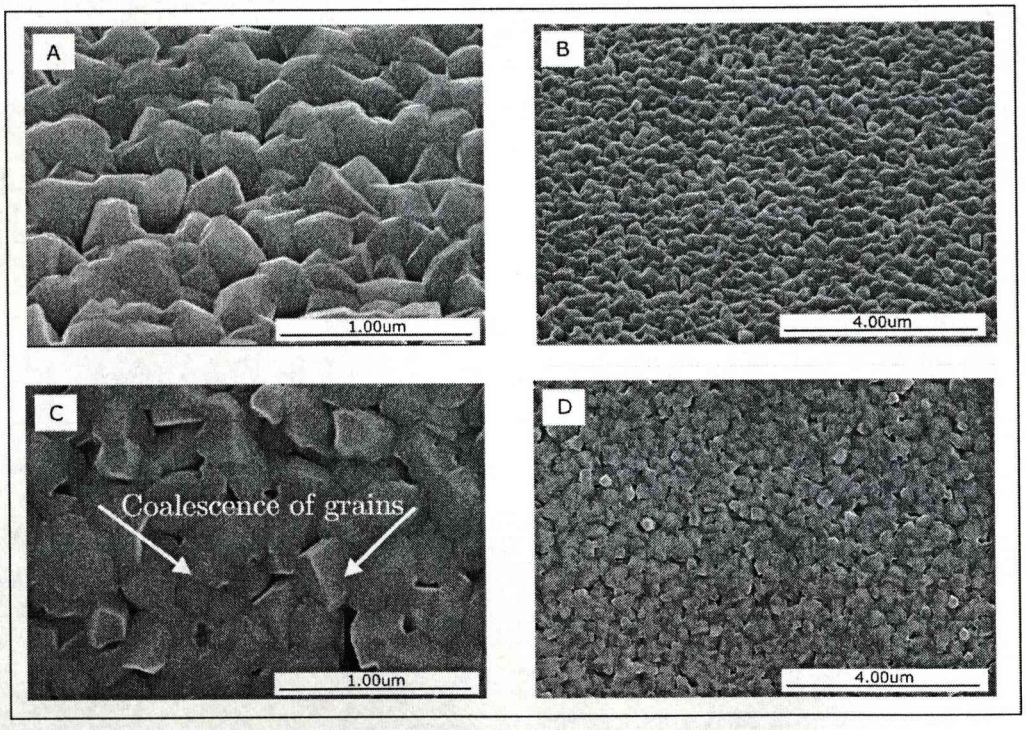

Figure 4.9 Scanning electron micrographs of $GaN/LaAlO_3/Si(111)$ (a) and (b) 45° tilt (c) and (d) parallel to the beam

A sample was prepared for cross sectional TEM so that selective area diffraction patterns could be resolved (Figure 4.10). This result supports the XRD data as the polycrystalline nature of the film is clearly evident from the rings and arcing of the SAD pattern. There is however an abrupt interface between the $LaAlO_3$ layer and the overlying GaN. This indicates that there is minimal chemical interaction or interdiffusion between the layers.

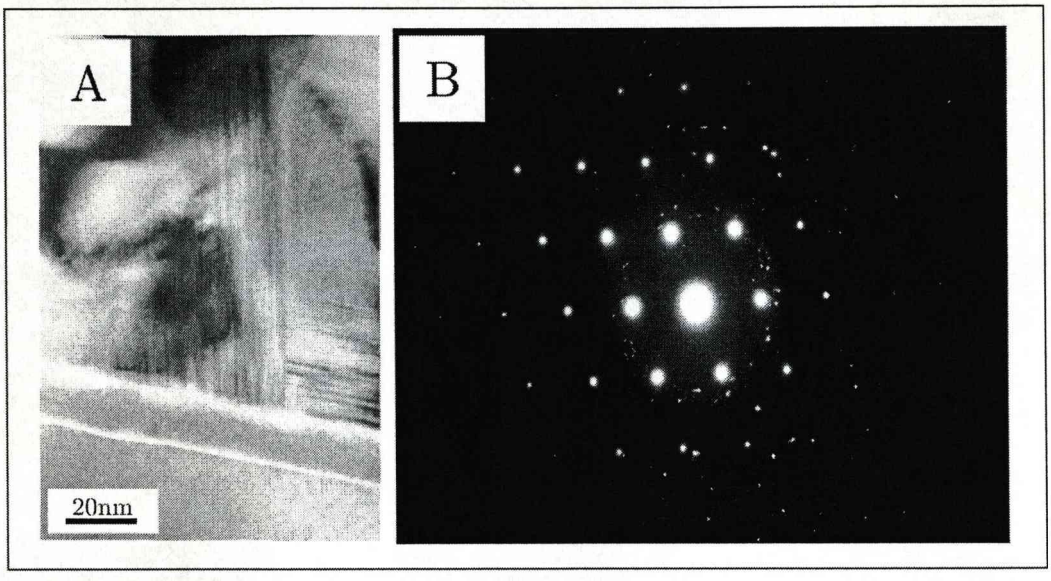

Figure 4.10 (a) Cross-sectional bright field image of GaN/$LaAlO_3$/Si(111) (b) Selective area diffraction pattern

If the epitaxial relationship between the GaN and $LaAlO_3$ layer is to be realized, the aluminate layer requires improvement. Firstly, the stoichiometry of the films needs to be addressed. This can be done by careful tailoring of the growth conditions. Secondly, the adverse interfacial interactions between the $LaAlO_3$ and the Si substrate must be suppressed. This could be done by inserting a more electropositive

interfacial layer between the $LaAlO_3$ and Si substrate. This would compete effectively with the silicon for the interfacial oxide and stabilise the interface through the formation of a direct Si-M bond.

One possible candidate material for this process brings us back to the initial Motorola work whereby a SrO/STO layer was deposited to form epitaxial GaAs overlayers. SrO layers have commonly been employed for the growth of STO on Si. Sr is highly electropositive which helps to suppress the unwanted formation of a silicate layer, providing a route to a stable interface free from amorphous silicon dioxide. Although STO is a poor compliant substrate for GaN, it can be used as a secondary compliant layer or graded layer with $LaAlO_3$ to obviate the mismatch between the Si and GaN.

4.4 SrO/STO/Si(111)

Within the COSMOS project, development of the SrO 'seed layer' was the responsibility of Qinetiq. For the purposes of this thesis some of that work is reported here as it is relevant to the future optimisation of any rare earth aluminate compliant layers. The oxide is both the interfacial template layer and the subsequent epitaxial layer. The SrO forms the initial template layer to the silicon substrate and is followed by an epitaxial strontium titanate layer. Strontium oxide is unstable in air and reacts with moisture and carbon dioxide to form strontium carbonate and strontium hydroxide. This makes post-deposition studies on the SrO template very difficult. Therefore deposition of the SrO and STO layers

were carried out sequentially in an MOCVD reactor. Deposition studies were made over a range of temperatures from 400°C up to 850°C in a nitrogen carrier gas and a pressure of 20 Torr.

The key issue for the compliant layer is the formation of a template epitaxial monolayer of SrO. This template effectively provides the buffer layer for the subsequent epitaxial STO film. However, since this layer is not air stable it is impossible to evaluate this step in isolation. Layers of 'SrO' are converted to strontium carbonate on exposure to air. In thicker layers of SrO (>10nm) this process can be observed as a change in colour of the deposited layer taking place within seconds of its removal of the material from the inert atmosphere within the kit into the laboratory atmosphere.

A range of temperatures were explored to give the thin layer of SrO required. The best temperatures appeared to be the lower ones where re-oxidation of the substrate was minimised prior to SrO deposition. It is also likely that based on the evidence from other CVD oxide materials, that the amount of carbon in the films is reduced to a minimum by the use of the lowest possible temperatures at this stage. Typical temperatures for the deposition of the SrO were around 400-450 ° C. Optimisation of the SrO deposition conditions were based on the subsequent analysis of the STO film and the effects of the changes in the SrO template deposition conditions on it.

Following the deposition of the SrO, the wafer was heated to around 850 ° C, the maximum temperature achievable in the current deposition apparatus. The object of this step was to assist the deposition of any native oxide formed during the first phase of the process and to promote the formation of an epi-template for the deposition of the STO. Deposition of stoichiometric STO was then carried out at 600°C. The layers ranged in thickness from a few nm up to approximately 100nm.

In the best cases, the resultant layers were very smooth with some evidence of epitaxial growth on parts of the wafer (Figure 4.11). The key processing steps are those leading to the formation of the epitaxial SrO template on the silicon surface and then the subsequent nucleation and growth of the STO. Although the best SrO appears to be deposited at relatively low temperatures, it seems likely that subsequent processing where the remaining silicon oxide is desorbed and the SrO takes up the desired epitaxial arrangement on the surface would be assisted by the use of higher temperatures. Similarly the achievement of lower background levels of oxygen and moisture in the deposition kits during this stage would be beneficial in reducing the need for high temperatures.

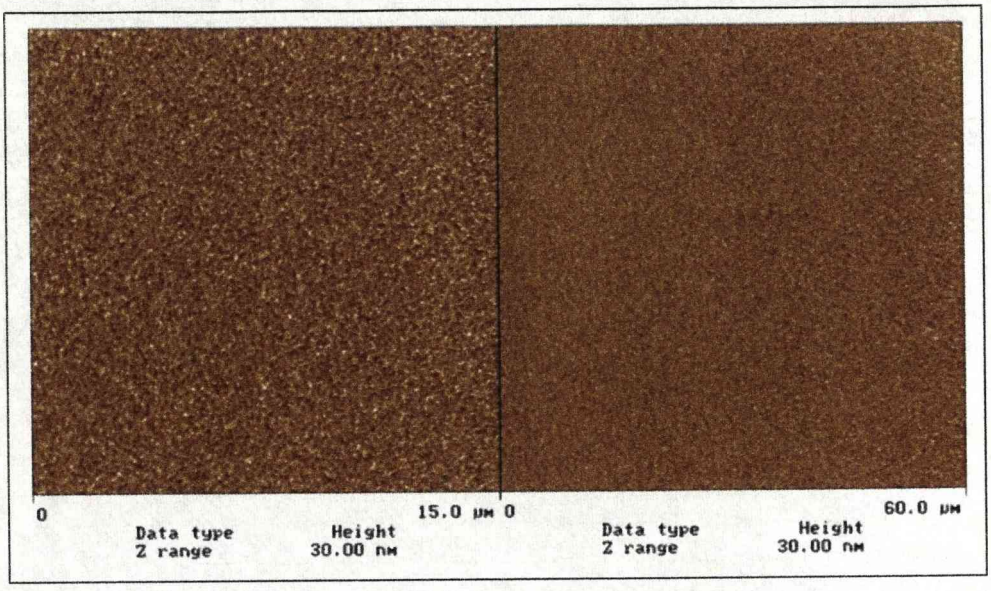

Figure 4.11 AFM of SrO/STO (courtesy of Qinetiq)

Initially, films were deposited in the absence of oxygen particularly during the initial SrO deposition. This was done to try and limit any oxidation/re-oxidation of the silicon substrate prior to the commencement of the deposition. However although the strontium precursor ($Sr(thd)_2$) used contains oxygen sufficient in principle to provide 'SrO', in many cases of the CVD of oxides additional oxygen needs to be added to the system to reduce or remove the carbon from the film. Carbon in the interface region between the silicon and the oxide layers might be expected to hinder the process of desorption of the interfacial oxide, by the formation of silicon carbide. Previously the CVD of STO using isotopic labelling of the precursors has been reported. Whilst titanium precursors tended to retain the oxygen from the precursor, the strontium precursors did not. Most of the oxygen in this case was derived from the oxygen gas added to the gas flows. In order to

explore the role of oxygen further, experiments were carried out where oxygen was added at various different stages in the process. The conditions used are shown in table 4.2

Table 4.2 Conditions used for depositions of SrO/STO.

Process	Conditions
'Oxygen free'	No oxygen in any part of the process
'Oxygen deficient start'	Oxygen on after SrO deposition started.
	On for anneal.
	On for STO deposition
'SrO oxygen'	Oxygen on as growth of SrO starts
	Off for anneal
	Off for STO
'Optimum oxygen'	Oxygen on for the SrO deposition
	Off for the anneal
	On for the strontium titanate
No anneal	As oxygen deficient start but no anneal after SrO deposition.

The 'optimum oxygen' process gave the consistent results in terms of the morphology and crystallinity of the deposited films. Uniformity across the 100mm diameter wafer was good but TEM analysis of the interface

showed that the process of forming an epitaxial compliant layer had not been successful over the whole wafer (Figure 4.12).

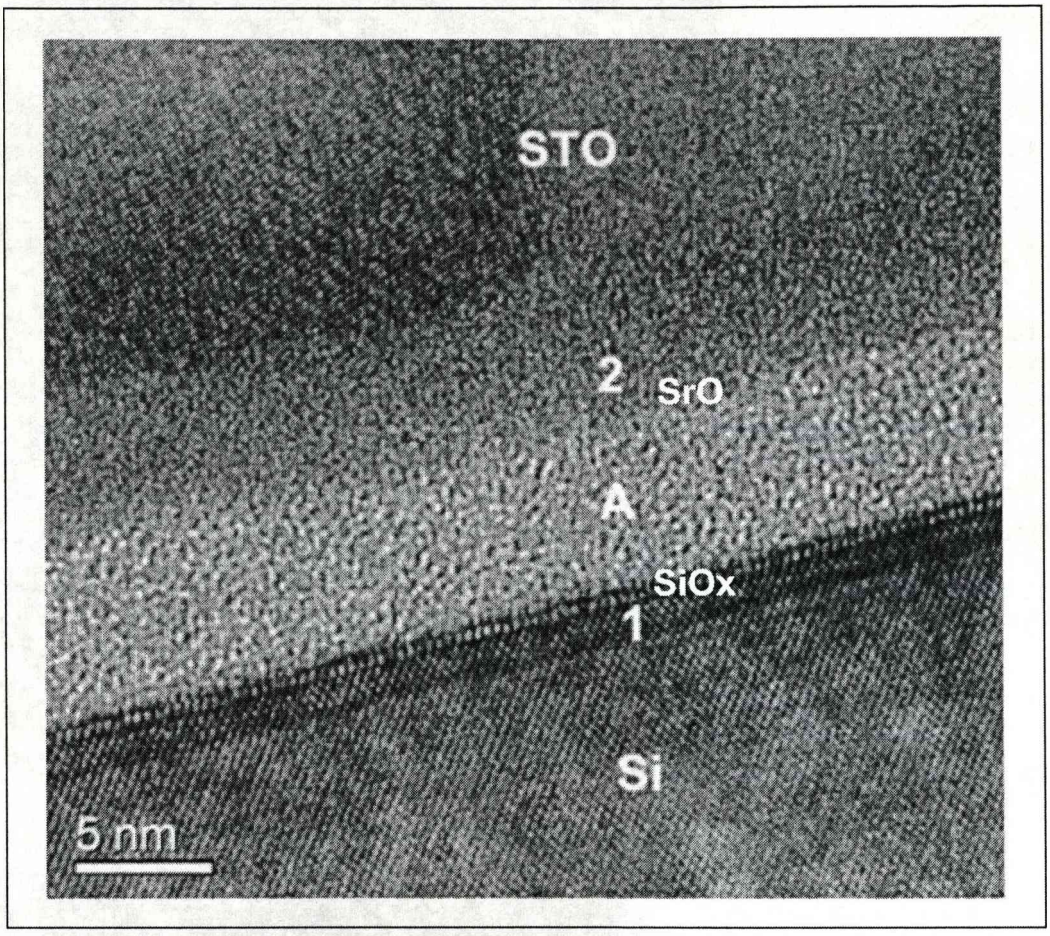

Figure 4.12 TEM micrograph of SrO/STO/Si interface (courtesy of Qinetiq)

Although wafer scale epitaxy was not achieved there were large areas of the films were there was an epitaxial relationship between substrate and the STO overlayer.

4.5 High-κ Dielectric properties

Lanthanum aluminate is a high-k dielectric material which is a useful property for some buffer layer schemes. To determine the dielectric properties of the $LaAlO_3$ films deposited in this work, metal gate electrodes were fabricated by the shadow mask technique [25]. The method involves the thermal evaporation of aluminium to form MOS capacitors ($Al/LaAlO_3/n\text{-}Si$) with an effective area of 4.9×10^{-4} cm^2. The capacitance-voltage (C-V) measurements reported here were made by Pouvanart Taechakumput in the Department of Electrical and Electronic Engineering.

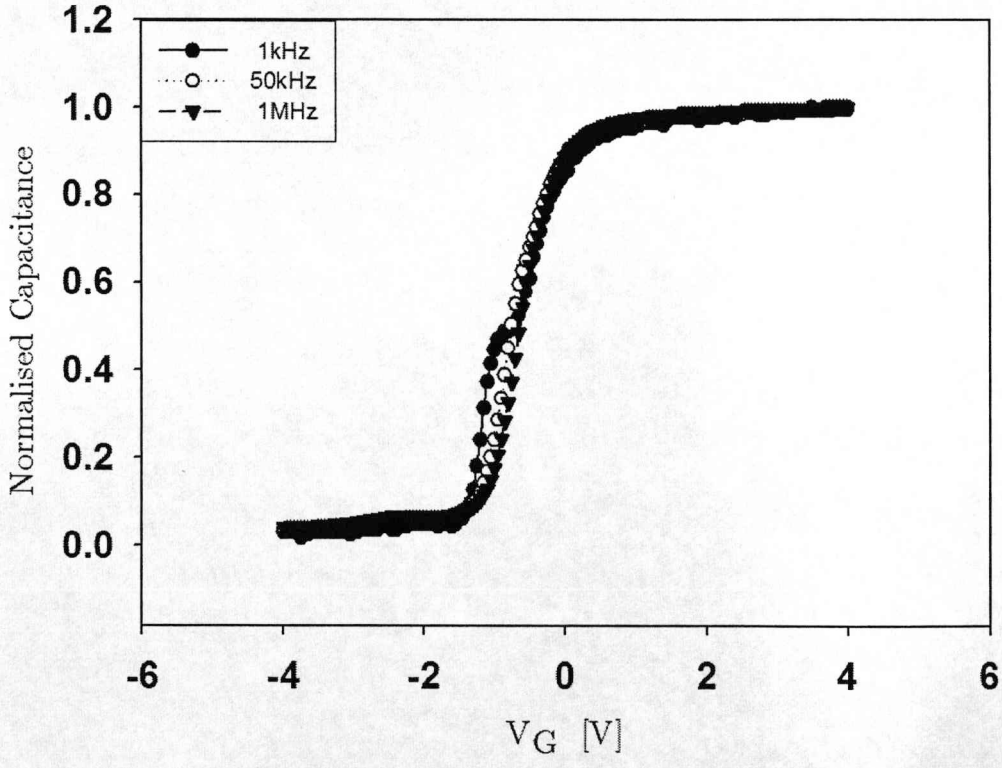

Figure 4.13 Capacitance-voltage curves of $Al/LaAlO_3/n\text{-}Si$ MOS capacitor structures with a $LaAlO_x$ film (La/Al = 0.54) grown at 180°C by liquid injection ALD

Figure 4.13 shows the normalised C-V characteristics at various frequencies for a film grown by ALD at a growth temperature of 180° and a thickness of 28nm.

Similar *C-V* characteristics were obtained for an MOCVD-grown film (data not shown) The doping density, determined from the C-V data, was found to be 8.18×10^{14} cm^{-3}. The calculated doping density was then further used to evaluate the experimental flatband voltage (V_{FB}), which was found to be -0.93V. In the present case, the flatband voltage shift (ΔV_{FB}) from its ideal value (-0.8) is diminutive indicating a small amount of fixed charge in the oxide. A noticeable shoulder on the lower frequency (1k Hz) C-V curve was observed at a gate bias of ~ -1V. This feature can be attributed to interface states, which respond at lower frequencies and may originate from La-Al diffusion and the subsequent interfacial layer mixing with SiO_2 layer during deposition. However, it is likely that post-metallization annealing in forming gas would reduce these traps according to time and temperature cycle followed. The extracted permittivity (κ) value from strong accumulation was found to be κ~11. Using the series capacitance model, the extracted permittivity (κ) of the $LaAlO_3$ layer was 13, which was consistent with a previous study. This value was calculated assuming the thickness of the SiO_2 interlayer was in the order of 1.5nm.

Figure 4.14 shows a comparison of the leakage current of the MOCVD and ALD deposited films. The range of leakage current was similar for

both samples for V_G from 0 to 20 V. However at low V_G in the range 1 to 7 V the MOCVD exhibited higher leakage currents. For example, the leakage current density (J) at 1V was 7 x 10^{-8} A.cm $^{-2}$ for the ALD film whereas J was 2 x 10^{-8}A.cm^{-2} for the MOCVD film at the same voltage.

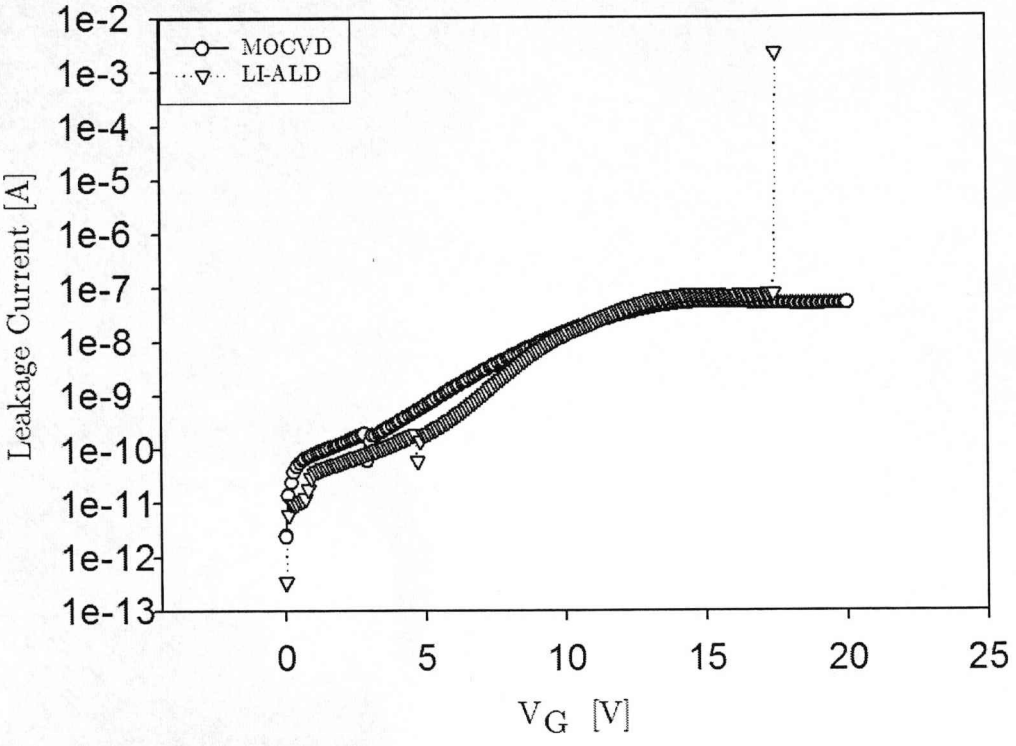

Figure 4.14 A comparison of I-V characteristics between the samples deposited by MOCVD (45nm La/Al = 2.5) and ALD (28nm La/Al = 0.54), under electron injection from the substrate

These electrical characteristics establish that the $LaAlO_3$ films are high-κ dielectrics (e.g. $\kappa > 3.9$ of SiO_2) and meet the first requirement for a suitable insulating compliant layer. As outlined previously, the second requirement which must be fulfilled, concerns the lattice structure and morphology of the material. The initial results which were presented in section 4.2 provide preliminary evidence that $LaAlO_3$ possess the

appropriate lattice structure and morphology required for it to be a successful compliant layer for the deposition of epitaxial GaN.

4.6 $PrAlO_3$/Si (100)

A further step was taken to investigate another rare earth aluminate as a candidate compliant layer for epitaxial GaN and as a possible high-κ dielectric material. Cerium, the first element in line of the lanthanide series, was discounted on the basis of the large mismatch between the $CeAlO_3$ crystal structure and that of Si. Praseodymium aluminate, on the other hand, produces a relatively small lattice mismatch with Si and was therefore considered to be a potentially more suitable material [3]. The following section describes the work carried out to evaluate $PrAlO_3$ as a high-κ dielectric and compliant layer for GaN.

The "single-source" precursor $[Pr(OPr^i)_6(Pr^iOH)]_2$ was used to deposit thin films of $PrAlO_3$ by liquid injection MOCVD and ALD (precursor supplied by Epichem Ltd.). The data obtain from thermogravimetric analysis (TGA) for $[PrAl(OPr^i)_6(Pr^iOH)]_2$ is shown Figure 4.15. The data shows that $[PrAl(OPr^i)_6(Pr^iOH)]_2$ evaporates in the temperature range 200 – 380°C and that the complex leaves relatively little residue (~2.5%). Similarly to $[La(OPr^i)_6(Pr^iOH)]_2$, a shoulder in the TGA curve is present at 200-250°C which is attributable to the loss of the weakly coordinating Pr^iOH ligand from the complex. (Theoretical weight loss of Pr^iOH from $[PrAl(OPr^i)_6(Pr^iOH)]_2$ = 10.32%.)

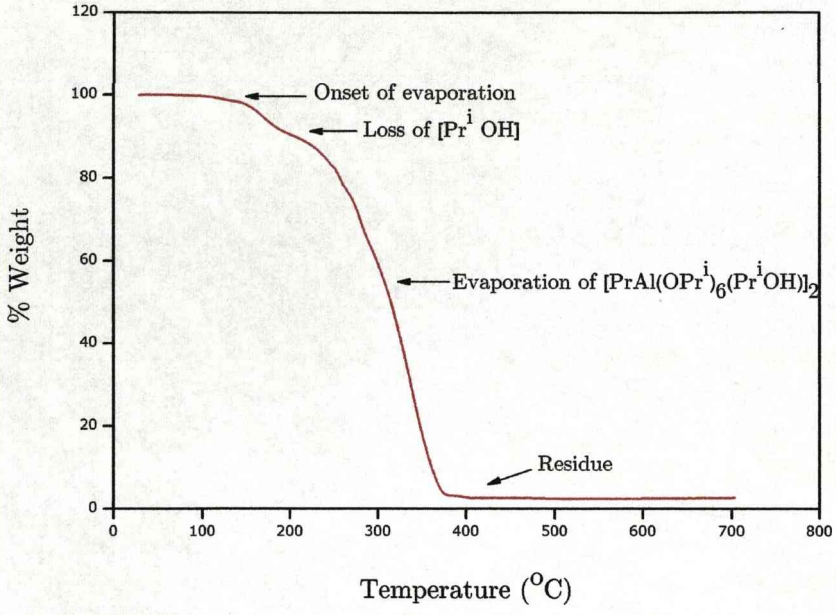

Figure 4.15 Thermogravimetric analysis of $[PrAl(OPr^i)_6(Pr^iOH)]_2$

The effects of growth temperature on the growth rate for $PrAlO_x$ by liquid injection MOCVD, is presented in Figure 4.16. As found with $LaAlO_3$, the MOCVD curve for $PrAlO_x$ exhibits an increase in the temperature range of 250-450°C. This corresponds to the region of kinetic control in which the film growth is dominated by thermal decomposition of the precursor onto the substrate. The oxide growth rate reaches a maximum at 450°C before decreasing rapidly due to thermal depletion of the precursor in the gas phase and on the reactor walls.

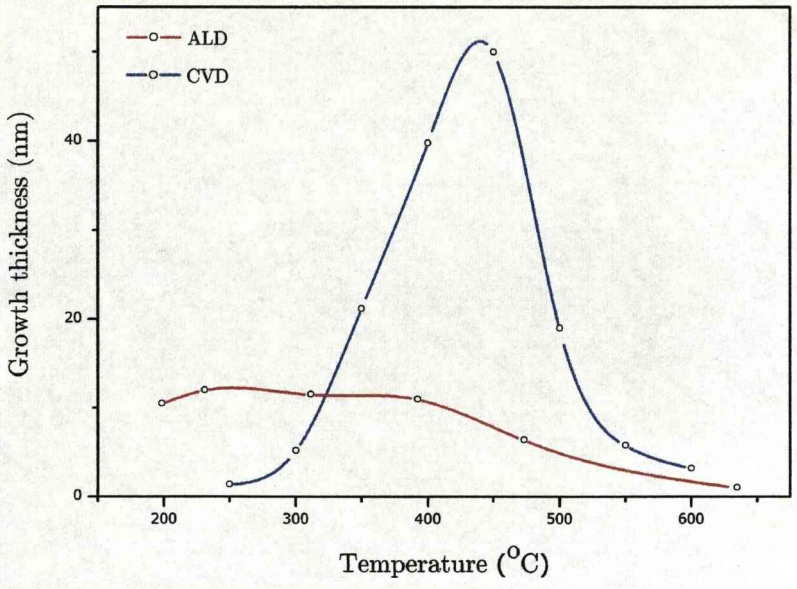

Figure 4.16 Variation of growth rate with substrate temperature films grown by liquid injection MOCVD and ALD using $[PrAl(OPr^i)_6(Pr^iOH)]_2$

Like $LaAlO_3$, the maximum $PrAlO_3$ growth rate from the analogous precursor $[PrAl(O^iPr)_6(Pr^iOH)]_2$ (0.924μm/hr) occurs at 450°C. However the maximum growth rate of $PrAlO_3$ is significantly higher than that for $LaAlO_3$. This apparent trend of increasing growth rate across the lanthanide series is most likely due to the extra volatility associated with the decreasing size of the lanthanide metal. The temperature for the onset of growth increases across the series, indicating an increase in thermal stability as the size of the lanthanide decreases. The effect of growth temperature on the growth rate for $PrAlO_x$ deposited by liquid injection ALD (Figure 4.16) shows that the growth rate remains relatively constant over the temperature range 180-300°C (≈ 0.23 nm/cycle). The growth rate is then seen to decreases at 350°C probably

due to desorption from the substrate surface. This indicates that the precursor is thermally stable up to 350°C.

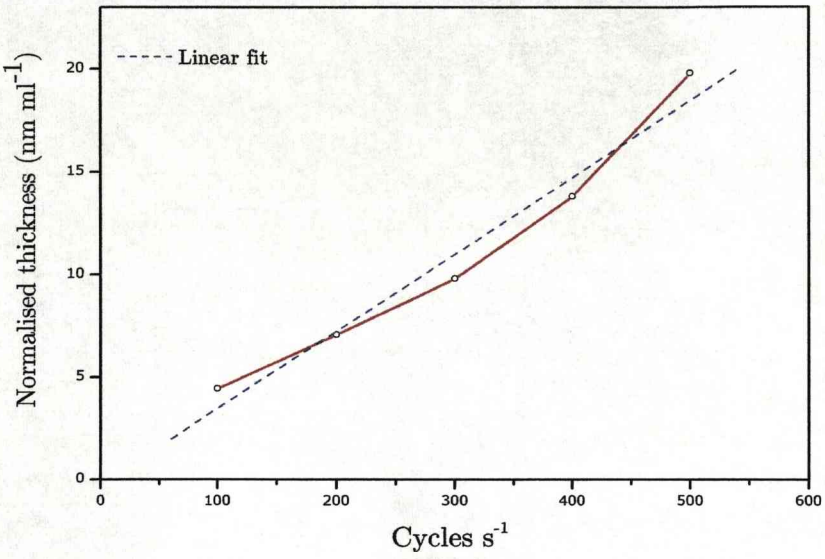

Figure 4.17 Variation of film thickness with number of ALD cycles for $PrAlO_x$ films grown by liquid injection ALD using $[PrAl(OPr^i)_6(Pr^iOH)]_2$

As can be seen from Figure 4.17 the growth rate of $PrAlO_x$ has a linear relationship with the number of ALD cycles, showing that the deposition of the material is highly controllable. However, like $LaAlO_3$ self-limiting growth did not occur for $PrAlO_3$ as the growth rate increased with injected volume of precursor/cycle.

The nominal compositions of the $PrAlO_x$ films were determined by Auger Electron spectroscopy (AES) and the data is shown in Table 4.3. All the films were of a high purity with no carbon detected (C estimated detection limit of 0.5 at%). The data show that the films grown by ALD

were all Pr deficient, the Pr/Al ratio varying between 0.56 and 0.71. A similar compositional effect was observed in the $LaAlO_x$ films deposited by liquid injection ALD in which La/Al ratios ranged from 0.50 to 0.61 (Table 4.3). The reason for the lanthanide deficiency is not known, but at the relatively low growth temperatures used in ALD (180 – 350 °C), it is unlikely to be due to thermal decomposition of the precursor. Rather, it is possible that the lanthanide deficiency is intrinsic to the deposition process itself; however detailed mechanistic study is beyond the scope of this thesis.

Table 4.3. Auger electron spectroscopy data showing the composition (at%) of $PrAlO_x$ films deposited by liquid injection MOCVD and ALD using $[PrAl(OPr^i)_6(Pr^iOH)]_2$

	Sample	*Deposition temperature (°C)*	*Pr*	*Al*	*O*	*Pr / Al*
MOCVD	11	250	21.2	12.5	66.3	1.70
	12	300	24.6	11.1	64.4	2.22
	13	350	23.1	13.2	63.8	1.75
	14	450	20.3	10.4	69.3	1.95
	15	500	22.7	29.9	47.3	0.76
ALD	16	180	15.0	26.8	58.2	0.56
	17	250	12.3	17.3	70.4	0.71
	18	300	14.5	25.1	60.4	0.58

The MOCVD grown films follow a different pattern with respect to temperature. All films grown below 500°C are praseodymium rich, with an almost constant Pr/Al ratio of 2:1 (Table 4.3). This is most likely due to the presence of both the Pr^{3+} and Pr^{4+} oxidation states in the deposited materials, as Pr^{3+} is readily oxidized to Pr^{4+}.

Samples of $PrAlO_x$ film grown by MOCVD at 500°C and 450°C, respectively, were annealed in air over the temperature range 700° to 900°C. This was carried out in order to assess the extent to which leakage currents could be reduced and the formation of a low-κ interfacial layer during CMOS processing inhibited. It is desirable for the dielectric film to remain amorphous up to relatively high temperature. The X-ray diffraction data of the as-grown samples (Figure 4.18) only exhibits a broad fluorescence background devoid of any crystalline diffraction features (except for a peak at 33° arising from the (200) reflection from the Si(100) substrate). Even after subsequent annealing at 900°C, the film remained amorphous which is in contrast to the results seen for $LaAlO_3$.

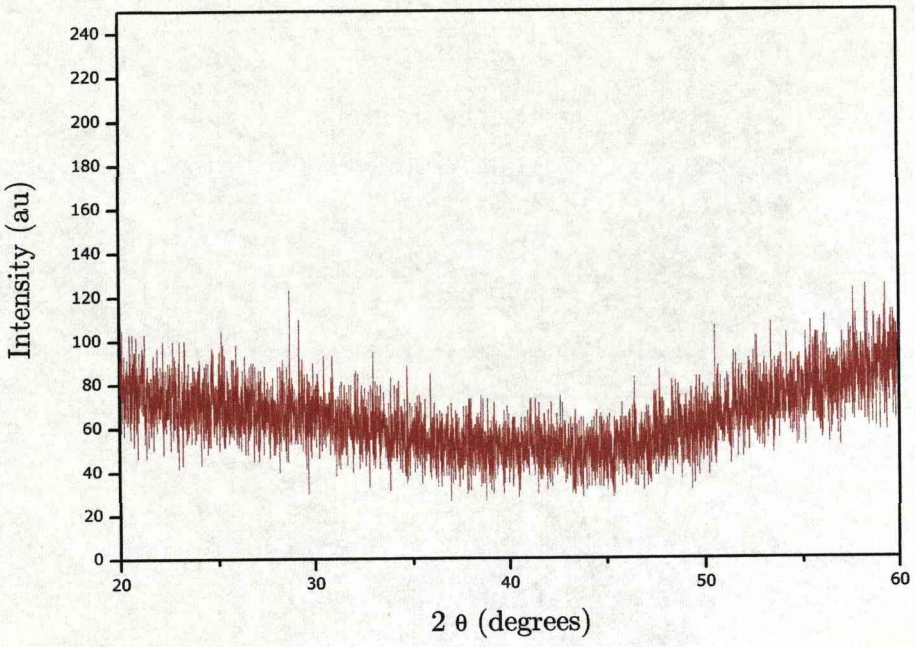

Figure 4.18 Θ - 2Θ X-ray diffraction data for a $PrAlO_3$ film grown by MOCVD on Si (100) at a substrate temperature of 500°C (Si (100) substrate)

Scanning electron microscopy (SEM) was also carried out on the $PrAlO_x$ films. This showed that the as-grown films had a featureless morphology (not shown here). The $PrAlO_x$ retained a featureless morphology even after annealing at 900°C in air for 15 min. Medium energy ion scattering (MEIS) was employed to investigate the effect of annealing on the composition and crystallinity of samples of the $PrAlO_x$ films. The samples were aligned to the ion beam along the [100] channeling direction of the silicon substrate and the electrostatic energy analyzer was positioned to record data along the [111] blocking direction.

The mass of Pr (140.90amu) is sufficiently greater than Al and O to enable the Pr depth distribution to be profiled without interference using

this geometry. Figure 4.19 shows the scattered ion energy distribution from a $PrAlO_x$ film deposited by ALD at 350°C. The thickness of the as-deposited layer in Figure 4.19 is estimated to be 7nm. After annealing at 900°C for 15 minutes in dry air, the Pr distribution reduces in intensity but broadens in thickness. This is indicative of some inter-diffusion with the Si substrate and the same trend is evident from the broadened Al distribution. Any crystallisation of the layer would usually be accompanied by the formation of an intense surface blocking feature due to registration of the Pr atoms within an ordered phase. However no evidence of this is seen in Figure 4.19, even after annealing at above 1000°C. This is consistent with the X-ray diffraction observations described above. The resistance of the $PrAlO_x$ films to crystallization is anticipated because of the relatively high content of glass forming elements such as Al and Si after annealing. The effect of incorporating these elements within the dielectric layer is clearly to suppress the electrical permittivity, which is discussed later in section 4.7.

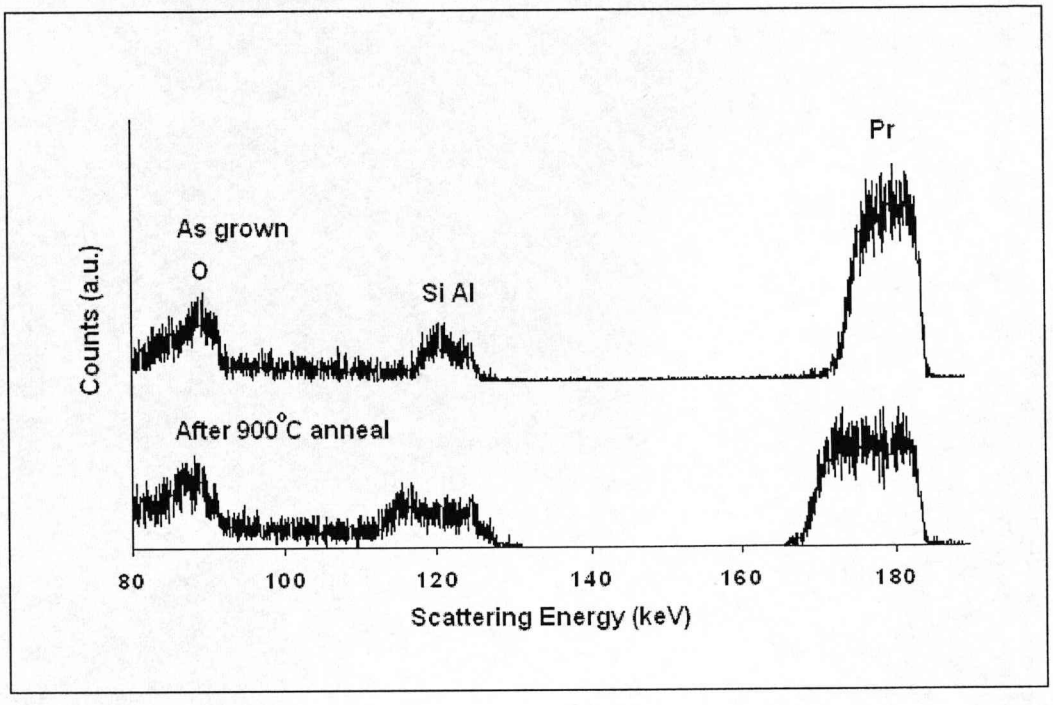

Figure 4.19. Medium energy ion scattering spectrum of $PrAlO_3$ film, as grown and after annealing at 900◦C in dry air for 15min

A set of experiments were conducted to ascertain the viability of $PrAlO_3$ as a compliant layer for the deposition of epitaxial GaN.

4.7 GaN/$PrAlO_3$/Si (111)

For consistency with the $LaAlO_3$ studies, an investigation of the deposition of GaN on $PrAlO_3$/Si(111) substrates was made. GaN films of thicknesses in the range of 50 to 120nm were deposited at a substrate temperature of 850°C.

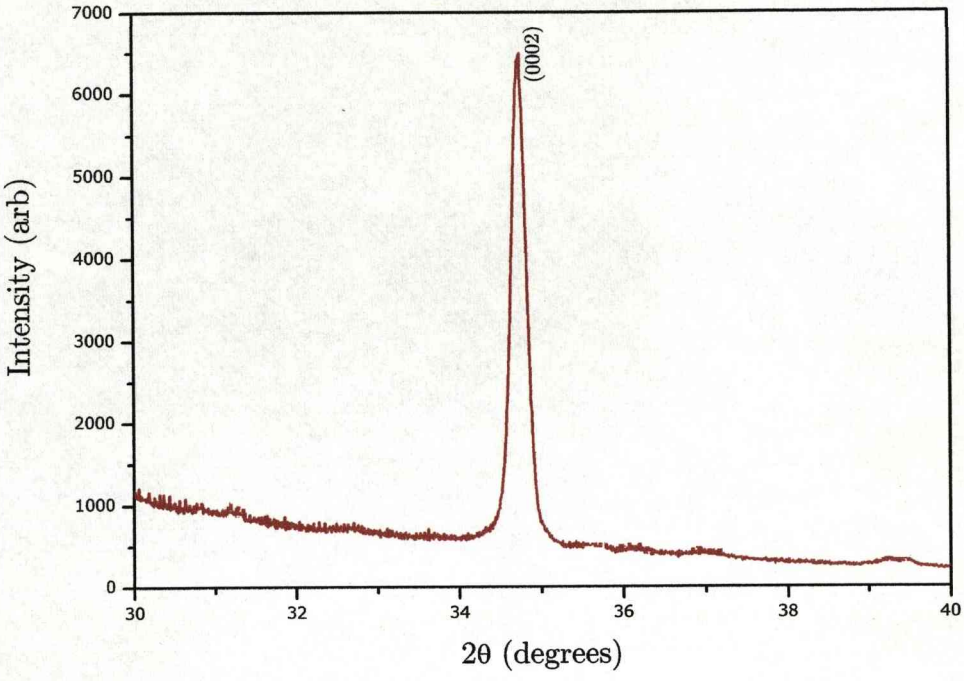

Figure 4.20 X-ray diffraction spectroscopy of GaN/$PrAlO_3$/Si(111)

Figure 4.20 shows the X-ray diffraction spectrum of the GaN/$PrAlO_3$/Si(111) sample which has a predominant peak at 34.4°, which corresponds to the (0002) reflection of GaN. The absence of other GaN diffraction features indicates that the nitride layer is clearly fibre textured along the c-axis of the crystal structure. The (0002) peak position is coincident with the $PrAlO_3$ (110) reflection which may contribute to the observed FWHM of 0.196°(706 arcsec).

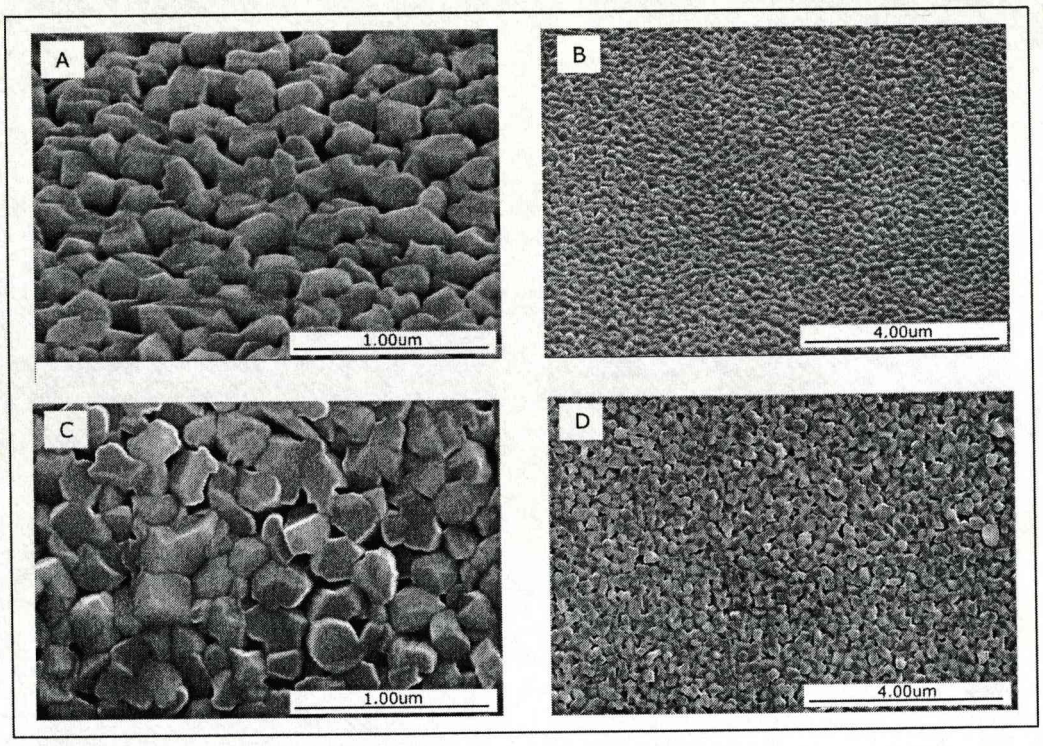

Figure 4.21 Scanning electron microscopy of GaN/$PrAlO_3$/Si(111)

The SEM micrographs shown in Figure 4.21 illustrate the highly polycrystalline nature of the GaN layers. The columnar structure of the nitride, coupled with a relatively low nucleation density leads to a high density of pores in the layer.

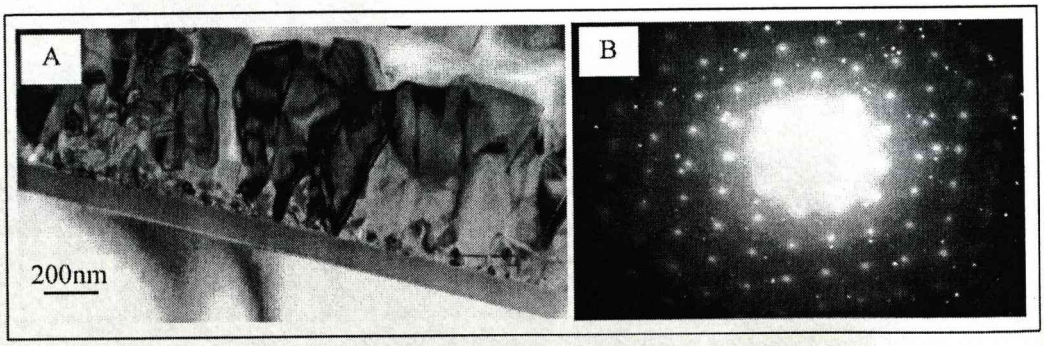

Figure 4.22 (a) Cross-sectional bright field TEM image (b) Selective area diffraction pattern of GaN/$PrAlO_3$/Si(111)

However, even at a thickness in the order of 100nm the GaN crystallites are beginning to show evidence of coalescence.

A sample of this specimen was prepared for cross sectional TEM (Figure 4.22). The mis-oriented spots are attributed to the small grains at the interface of the GaN layer with the $PrAlO_3$. The spots are characteristic of the high nucleation of the crystallites but these are over grown by the faster growing (0002) planes of GaN.

4.8 High-κ dielectric properties

The dielectric properties of the $PrAlO_x$ films, were investigated through the fabrication of Al/ $PrAlO_x$ /n-type Si(100) MOS capacitor (MOSC) structures (courtesy of Pouvanart Taechakumput, Departm ent of Electrical and Electronic Engineering). Figure 4.23 compares as-grown and post metallization annealed (PMA) capacitance-voltage (*C-V*) characteristics of the MOSCs. The samples were deposited by liquid injection MOCVD at 500°C, with a Pr/Al ratio of 0.76, yielding a physical thickness of 95nm. The *C-V* curves before PMA exhibited a significant hysteresis (~2.66V) in an anti-clockwise direction. This indicates significant positive charge trapping. Despite this, the C-V curves did show a steep transition from accumulation to inversion indicative of a low interface state density. After PMA, the hysteresis was reduced to a low level (~ 0.04V), but interface states may have been created, which is evident from the stretch out of the *C-V* curves. The relative permittivity calculated from the accumulation capacitance was ~12, assuming a 1nm of interlayer.

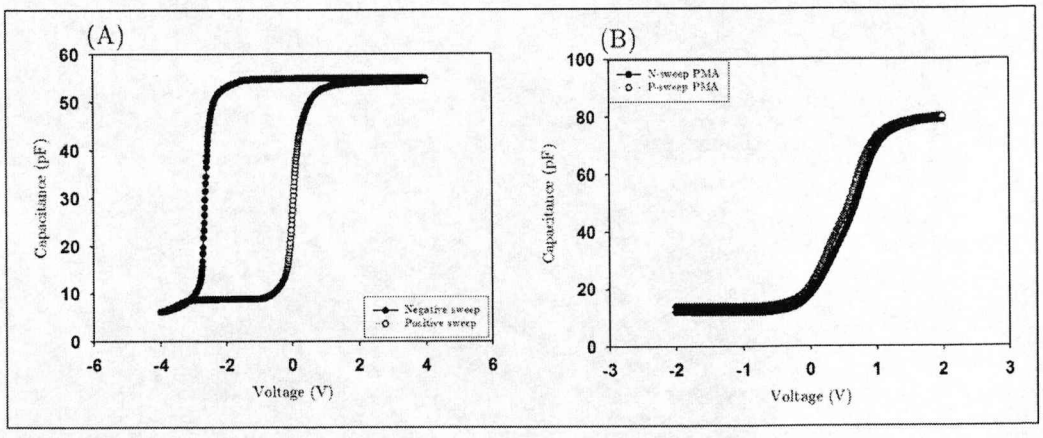

Figure 4.23 As-grown and post metallization annealed (PMA) capacitance-voltage (*C-V*) characteristics of the MOSCs

Figure 4.24 shows, normalized *C-V* curves for the liquid injected ALD $PrAlO_x$ films, with a Pr/Al ratio of 0.71. A significant anti-clockwise hysteresis (~1.30V) was observed in the as-grown sample. The relative permittivity obtained from the accumulation capacitance was ~14 (assuming a 1nm interlayer). After a subsequent PMA in forming gas, the resulting capacitance data of these films indicated a reduction in dielectric constant to ~7. The reduction in the measured capacitance and hysteresis after PMA may due to a removal of some trapped hydroxyls $(OH)^-$ in the dielectric. This has been reported to cause increases in the dielectric constant at lower frequencies and can also act as potential trapping sites.[26] The as-grown $PrAlO_x$ films responded well to the forming gas treatment, reducing the hysteresis to a negligible level. The fixed oxide trap charge density (N_{ot}), assumed to be located near the oxide-semiconductor interface, can be evaluated considering that $N_{ot}=(C_{acc}\times\Delta V_{FB})/(qA)$, where C_{acc} is the accumulation oxide capacitance, ΔV_{FB} is the hysteresis width taken from the extracted flatband voltage of

both sweeps, q is the electron charge and A is the effective electrode area.

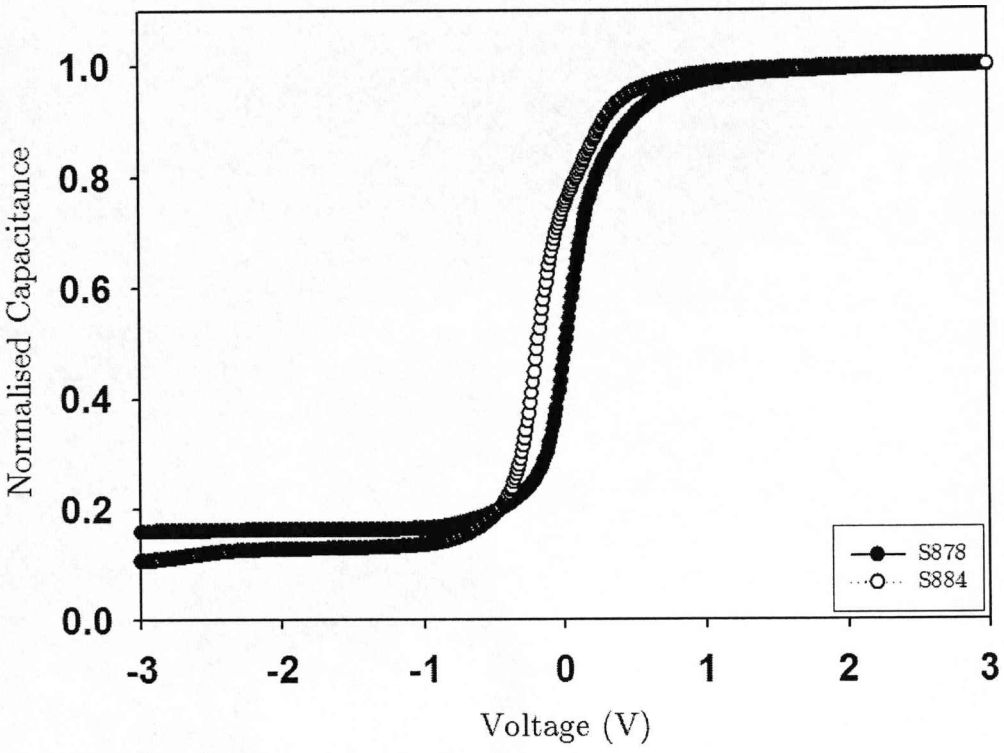

Figure 4.24. Normalized *C-V* curves for the liquid injected ALD $PrAlO_x$ films, with a Pr/Al ratio of 0.71

The positive oxide trapped charge in the as-grown samples (density of 10^{12} cm^{-2}) was reduced in both cases to negative 4×10^{10} cm^{-2} the current-voltage characteristics of both as-grown films are depicted in Figure 4.25. The leakage current density at 1 $MVcm^{-1}$ was 10^{-6} Acm^{-2} for the MOCVD film and only 2×10^{-7} Acm^{-2} for the ALD film. These values were an order

of magnitude higher than previous studies[26] but are comparable with other high-κ dielectrics such as Pr-silicates[27] and HfO_2[28].

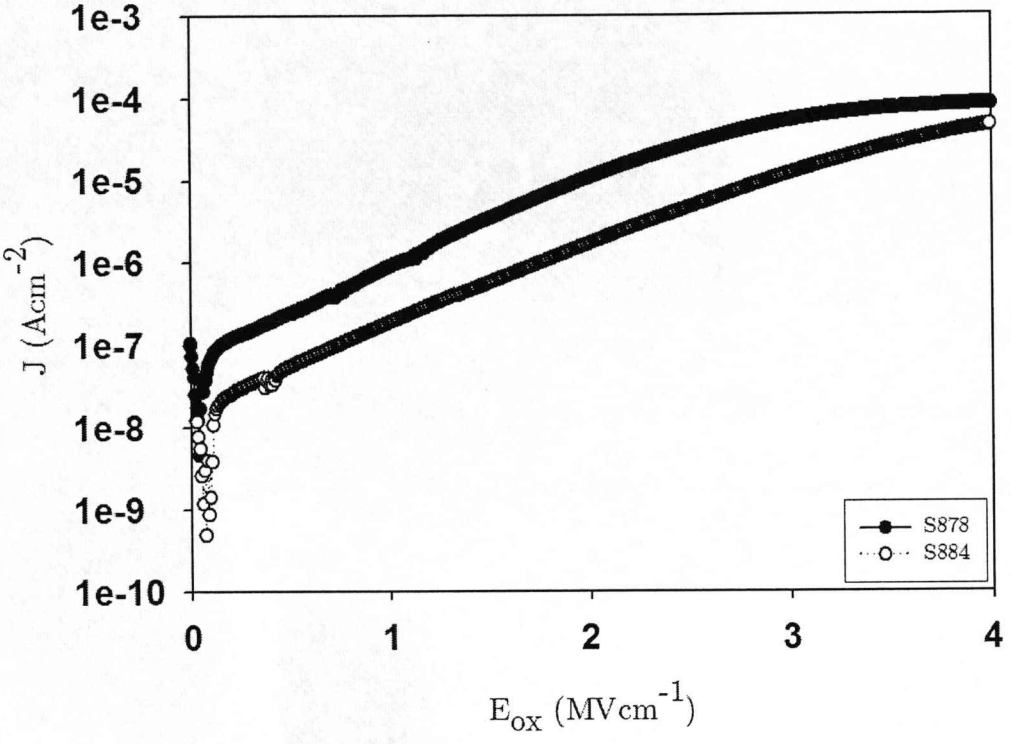

Figure 4.25. A plot of current density (J) versus electric field across the oxide (E_{ox}) for MOCVD (S878) and ALD (S884)

4.9 Conclusions

The deposition of lanthanum aluminate by MOCVD and ALD has been demonstrated using a single source precursor for the first time The single-source alkoxide precursor $[MAl(OPr^i)_6(PriOH)]_2$ (M= La or Pr) forms films which are amorphous as-deposited by MOCVD or ALD in the temperature range 150°C to 600°C. Although the as-deposited films are non-stoichiometric (from the perovskite composition), annealing in

air can be used to crystallize the films at temperatures between 750° and 850°C. After annealing the films exhibit a polycrystalline microstructure and some interaction is indicated between the film and the silicon substrate. Capacitance-voltage measurements show that the permittivity of the film is 13 for $LaAlO_3$ and 14 for $PrAlO_3$ at strong accumulation. The leakage current densities of the $LaAlO_3$ films are 7×10^{-8} A cm^{-2} at 1V for ALD and 2×10^{-7} A cm^{-2} at 1V for MOCVD grown films.

The growth of gallium nitride on the polycrystalline films of both lanthanum- and praseodymium aluminate has been investigated. The growth of GaN is textured in the [0001] direction and the interface between the oxide and GaN is observed to be abrupt which is indicative of a minimal chemical interaction or inter diffusion. These results suggest that if adverse interfacial interactions can be suppressed (eg. by a SrO seed layer) a better epitaxial orientation might be achieved in the aluminate and nitride overlayer.

References:

1. Motorola patent. J.M.Finder, K.Eisenbeiser, J.Ramdani, R. Droopad, W.J.Ooms Patent No. US655946 B1 2003]

2. Thin Films and Heterostructures for Oxide Electronics By Satishchandra B. Ogale, Inc NetLibrary. Pg 67.

3. Liu L. and Edgar J.H. 2002 *Material Science and Engineering. R* **37** 61.

4. J.Roberts 2006 *Rep.Prog.Phys.* **69** 327-396

5. C. M. Carlson, J. C. Price, P. A. Parilla, D. S. Ginley, D. Niles, R. D. Blaugher, A. Goyal, M. Paranthaman, D. M. Kroeger and D. K. Christen, Physica C, 1998, **304**, 82.

6. V. Sandu, J. Jaklovszky, D. Miu, D. Dragulinescu, C. Grigoriu and M. C. Bunescu, J. Mater. Sci. Lett., 1994, **13**, 1222.

7. E. Sader, H. Schmidt, K. Hradil and W. Wersing, Semicond. Sci. Technol., 1991, **4**, 371.

8. A. E. Lee, C. E. Platt, J. F. Burch, R. W. Simon, J. P. Goral and M. M. Aljassim, Appl. Phys. Lett., 1990, **57**, 2019.

9. S. S. Shoup, M. Paranthaman, D. B. Beach, E. D. Specht and R. K. Williams, J. Mater. Res., 1997, **12**, 1017.

10. H. Ichinose, H. Katsuki and M. Nagano, J. Cryst. Growth, 1994, **144**, 59.

11. H. Ichinose, Y. Shiwa and M. Nagano, Jpn. J. Appl. Phys., Part 2, 1994, **33**, 5907.

12. A. A. Molodyk, I. E. Korsakov, M. A. Novojilov, I. E. Graboy, A. R. Kaul and G. Wahl, Chem. Vap. Deposition, 2000, **6**, 133.

13. G. Malandrino, I. L. Fragala and P. Scardi, Chem. Mater., 1998, **10**, 3765.

14. M. V. Cabanas, C. V. Ragel, F. Conde, J. M. Gonzalez-Calbet and M. Vallet-Regi, Solid State Ionics, 1997, **101**, 191.

15. G. Malandrino, A. Frassica and I. L. Fragala, Chem. Vap. Deposition, 1997, **3**, 306.

16. M. Nieminen, M. Putkonen and L. Niinisto, Appl. Surf. Sci., 2001, **174**, 155

17. M. Nieminen, T. Sajavaara, E. Rauhala, M. Putkonen and L. Niinisto, J. Mater. Chem., 2001, **11**, 2340.

18. B. S. Lim, A. Rahtu, P. de Rouffignac and R. G. Gordon, Appl. Phys. Lett., 2004, 84, 3957.

19. G. Malandrino, I. L. Fragala and P. Scardi, Chem. Mater., 1998, 10, 3765.

20. M. LeskelaΥ and M. Ritala, in Handbook of Thin Film Materials, vol. 1, ed. H. S. Nalwa, Academic Press, San Diego, 2001.

21. T. D. Manning, Y. F. Loo, A. C. Jones, H. C. Aspinall, P. R. Chalker, J. F. Bickley, L. M. Smith and G. W. Critchlow, J. Mater. Chem., 2005, 15, 3384.

22. High dielectric constant Materials. Part III. Springer Berlin Heidelberg 2005.

23. T.L.Chu, M.H.Francombe, G.A.Gruber, J.J.Oberly and R.L.Tallman. Report No AFCRL-65-574. Westinghouse Research Laborarories, Pittsburg, 1965. Pp 31-34.

24. A. N. Alexeev, B. A. Borisov, V. P. Chaly, D. M. Demidov, A. L. Dudin, D. M. Krasovitsky, Yu. V. Pogorelsky, A. P. Shkurko, I. A. Sokolov, M. V. Stepanov and A. L. Ter-Martirosyan, MRS Internet J. Nitride Semicond. Res. 4, 6 **1999** 1

25. G. Vellianitis, G. Apostolopoulos, G. Mavrou, K. Argyropoulos, A. Dimoulas, J. C. Hooker, T. Conard and M. Butcher, Mater. Sci. Eng., B, 2004, 109, 85.

26. de Rouffignac, P.; Gordon, R. G. *Chem. Vap. Deposition* **2006**, *12*, 152.

27. Lupina, G.; Schroeder, T.; Dabrowski, J.; Ch, W.; Mane, A. U.; Mussig, H. J.; Hoffmann, P.; Schmeisser, D. *J. Appl. Phys.* **2006**, *99*, 114109.

28. NiinistoΥ, J.; Putkonen, M.; NiinistoΥ, L.; Stoll, S. L.; Kukli, K.; Sajavaara, T.; Ritala, M.; LeskelaΥ, M. *J. Mater. Chem.* **2005**, *15*, 2271.

Chapter 5 Lanthanum Nitride and Scandium Nitride

Overview

This chapter investigates the development of the rocksalt structured nitrides, lanthanum nitride and scandium nitride for compliant layers. The rationale for this is based on the concept of a graded $La_xSc_{1-x}N$ layer between the gallium nitride and the silicon substrate. A novel approach to the MOCVD of these nitrides is proposed using silylamide-based precursors. The process exploits a gas-phase transamination reaction but was found to be highly sensitive to in-situ oxygen contamination. Also, the thermodynamic stability of LaN favoured rapid decomposition to La_2O_3 after exposure to the ambient atmosphere.

A second approach to the formation of ScN and LaN was developed using molecular beam epitaxy. In the case of ScN, it was found that epitaxially oriented films could be deposited onto Si(111) substrates. These compliant layers were subsequently used as substrates for epitaxial GaN growth on the silicon substrates. Scanning transmission electron microscopy has been used to investigate the microstructure of the interface between the nitride and silicon.

Chapter 5

Lanthanum Nitride and Scandium Nitride

5.1 Background and rationale

When considering compliant layer candidates for GaN epitaxy, it is logical to consider a range of stoichiometric nitrides. The rationale for this is simple: by either using ammonia or atomic nitrogen for the GaN growth, it is practically easier to use a different cation(or cations) for the preliminary buffer layer (e.g. TiN, TaN etc). In this respect, lanthanum nitride (LaN) and scandium nitride (ScN) have been previously identified as candidates for GaN epitaxy[1]. The chapter is structured as follows: Section 5.2 outlines some key crystallographic and electrical properties of LaN and ScN as a basis for assessing their value as interface materials for GaN epitaxy. Section 5.3 outlines why a graded LaN and ScN buffer layer was targeted. The remaining sections describe the outcomes of the deposition of the nitride layers along with the techniques used to deposit the films.

5.2 Interface structures for GaN/ScN/Si (111)

ScN is a group III transition metal nitride, which has a rock-salt structure [2]. It is one of the least well researched of the transition metal nitrides, but in common with the others is known to have some potentially useful properties, such as high hardness and high thermal stability [3]. Recent interest in this material is mainly due to new data on its electronic properties and also the realisation of the possible

combination with GaN [4]. Early studies suggested that ScN was a semimetal [5], but further research revealed that it is a semiconductor with a direct band gap of 2.1eV[6]. The interest in its potential as a compliant layer is due to its lattice constant, which lies between 0.4500 and 0.4505nm[4]. The (111) surface of ScN has an inter-atomic spacing of 0.3146nm, which is close to that for hexagonal GaN (0.3189nm) and thus gives rise to a low lattice mismatch value of 0.1%. Moreover, the slightly smaller lattice parameter of ScN relative to GaN introduces a degree of compressive strain. This strain can be exploited to offset the tensile strain arising from the thermal mismatch between the Si substrate and the GaN epilayer. Ideally, this mitigation of strain could help to reduce the likelihood of cracking of the GaN - a common problem in other epitaxial buffer layer systems.

ScN deposition has previously been investigated using a variety of methods, including CVD [7], MBE [8-9] and magnetron sputtering [10]. To date, MBE has been the most commonly used technique for depositing ScN films. A detailed account and discussion of the previous literature on ScN deposition by the MBE method is available in chapter 2 of this thesis.

As stated above, ScN comprises a rock salt crystal structure in which the number of anions equals the number of cations is equal. These crystals are often referred to as AX compounds, whereby A and X denote the cation and anion respectively. The coordination number of both the cation and anions is six and therefore the cation-anion ratio r_c/r_a should lie in the range 0.4 to 0.7. The actual Sc/N ratio is 0.5, since the ionic

radii are Sc^{3+} 0.75Å and N^{-3} 1.5Å. The unit cell for this crystal is shown in Figure 1. The ScN crystal structure can be considered in terms of two interpenetrating Face Centred Cubic (FCC) lattices, one composed of cations and the other anions. The lattice parameter a = 4.50Å and therefore the minimum distance between lattice points ($a\sqrt{2}/2$), which is the distance between cations in {111} planes, is 3.18 Å (see Figure 5.2).

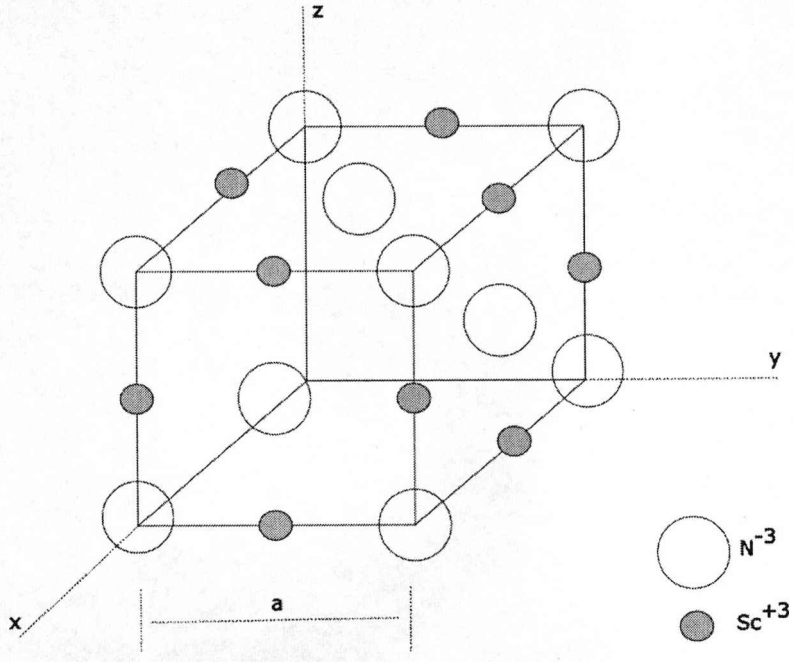

Figure 5.1. The unit cell of scandium nitride

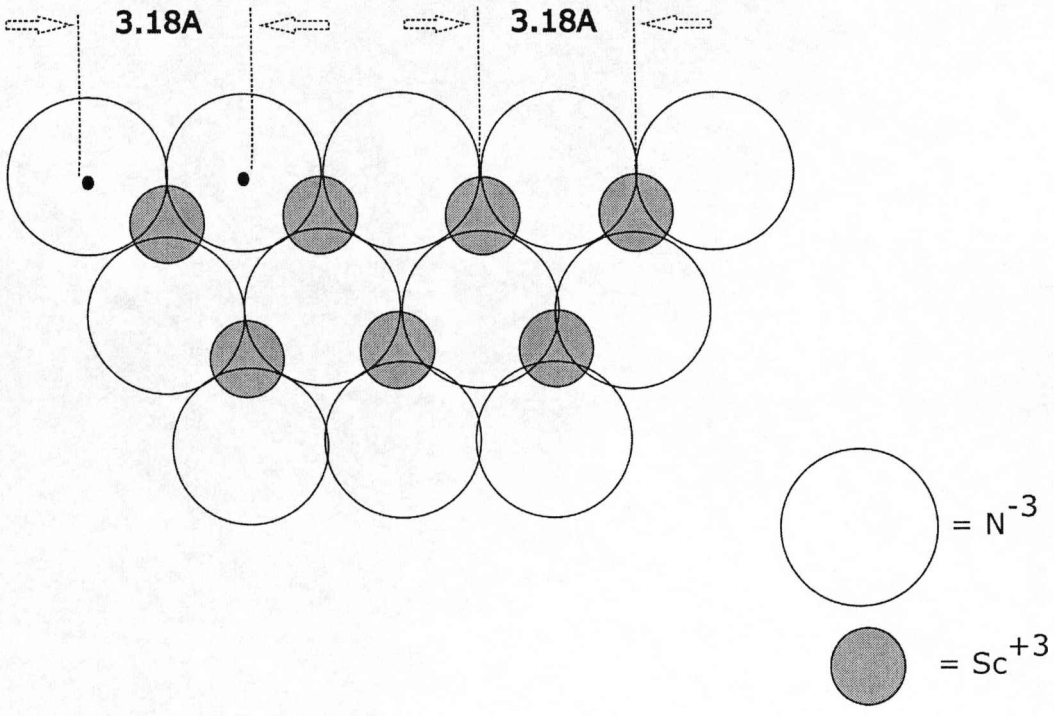

Figure 5.2. Distance between lattice points in the {111}planes of ScN

The close–packed planes in ScN are composed of large N^{-3} anions. As these planes are stacked on top of each other, small interstitial sites are created in which the Sc^{3+} cations can reside. Two different forms of interstitial positions exist, namely tetrahedral or octahedral (Figure 5.2). Since the coordination number for ScN is 6, the cations take up the octahedral positions. The closest distance between lattice points (3.18Å) is the same for both anions and cations. The position of the anions relative to the cation for the (100) plane is shown in Figure 5.3 (The relative sizes of both ions have been drawn to scale). The unit cell for ScN showing the (100) with the <100> normal to the plane of the paper is shown in Figure 5.3.

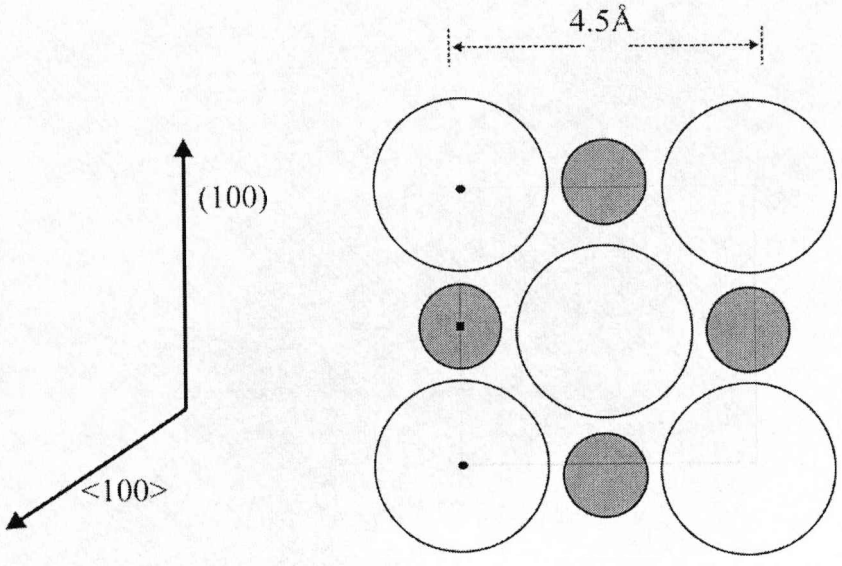

Figure 5.3 Unit cell for ScN showing the (100) with the <100> normal to the plane. The relative size of anions and cations are drawn to scale; ● and ■ represent the lattice points.

Silicon has a diamond FCC-like unit cell crystal structure in which each Si atom bonds to four other Si atoms and these bonds are totally covalent. The lattice is cubic and is basically the FCC lattice with four extra atoms internally positioned at the tetrahedral positions. This results in a maximum packing density of 34% compared with 74% in the simple FCC unit cell. The lattice parameter a = 5.43Å and therefore the nearest distance between lattice points is given by $a\sqrt{2}/2$ = 3.8Å, this also occur on the {111} planes.

Epitaxial ScN films have been reported to be grown on (111) orientated Si substrates by MBE using ammonia as a reactive nitrogen source. X-ray diffraction techniques have been used to study the relative crystallography of the substrate and the film. Moram and co–workers [11]

reported that the principal orientation of ScN with respect to the (111) Si substrate is $(111)_{ScN}//(111)_{Si}$ with an in-plane rotation of 60°. The smallest lattice mismatch between Si substrates and ScN films would occur when ScN(111) and Si(111) planes are stacked in an AB arrangement. In this case, the percentage mismatch is calculated using equation 5.1 (below).

$$\left[\frac{(a_{Si}\sqrt{2}/2) - (a_{ScN}\sqrt{2}/2)}{(a_{ScN}\sqrt{2}/2)}\right] \times 100 \qquad \text{(equ. 5.1)}$$

$$= \left[\frac{(3.8 - 3.18)}{3.18}\right] \times 100$$

$$= 19\ \%$$

Figure 5.4 represents a schematic diagram of the lattice mismatch which occurs between ScN(111) and Si(111).

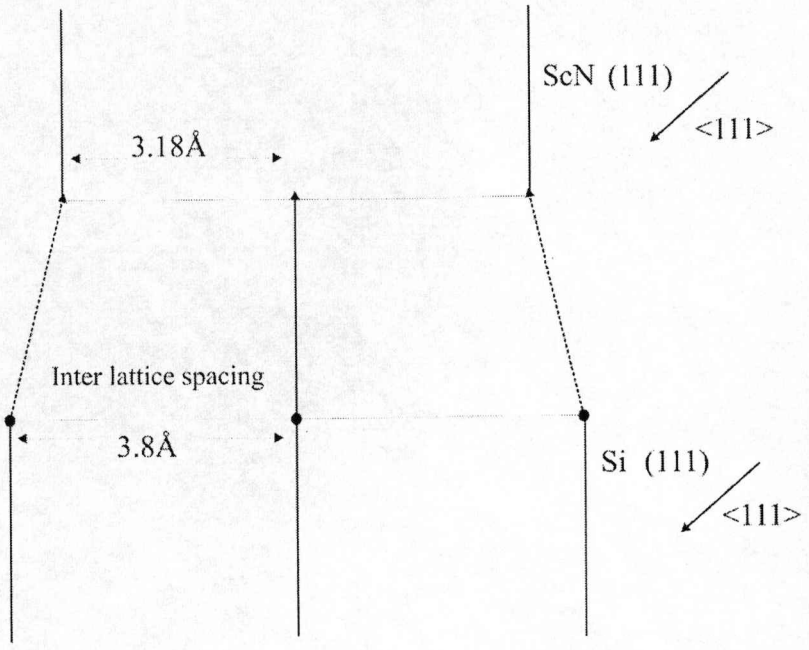

Figure 5.4 Schematic diagram of lattice mismatch for ScN(111)//Si(111)

From Figure 5.4 it is clear that atoms close to the surface of the Si (111) surface would experience compression due to the lattice mismatch, whereas those of the substrate would be under tension. Studies using high-resolution transmission electron microscopy (HRTEM) techniques have revealed this kind of strain contrast and associated dislocations at the interfaces of many different systems [12]. The strain induced by lattice mismatch can result in irregularities in the crystal structure leading to edge, screw or mixed dislocations. The stresses caused by dislocations are complex and their full discussion is beyond the scope of the present work. However, the dislocation density (τ) has been shown to be related to the plastic deformation ρ by equation 5.2

$$\tau \propto \rho^{1/2} \qquad \text{(equ.5.2)}$$

The plastic deformation at the interface is related to the degree of mismatch of the lattice planes and stacking faults associated with the interface. Similar mismatch considerations can be applied to the deposition of any subsequent layers onto the ScN, for example GaN. The small lattice mismatch between ScN and GaN (<1%) should act to minimise stress, strain, dislocation and deformation and it is for this primary reason that ScN has been selected here as a compliant layer for the deposition of GaN on Si substrates.

The lattice mismatch is clearly of primary importance since the crystalline quality of the heterostructures may be decisive in determining the physical properties of the epilayer. The atomic bonding at the interface determines the difference in crystal symmetry and lattice constants generally lead to an anisotropic lattice epitaxial alignment, lattice mismatch accommodation and defect density. These factors are all interrelated and inherently complex, but many studies have shown that the relative crystallographic orientation can be determined. X-ray and electron diffraction techniques have been used to investigate crystal orientation and high-resolution transmission electron microscopy has been used to image these interfaces in some detail [13]. The differences in crystal symmetry and lattice constants generally lead to an anisotropic lattice mismatch acco mmodation where the misfit strain is relieved by misfit dislocations. The quest to identify candidate crystal structures

with the appropriate electronic properties and sufficiently close lattice matches required to reduce these effects is a matter of ongoing research.

5.3 Graded LaN/ScN layers

LaN has a cubic crystal structure with a lattice constant of 0.5294nm. This is very close to that of Si (0.5430nm) and gives rise to a lattice mismatch as little as 1.6%. There is still however a large mismatch between the LaN and GaN (19%). One way to reduce lattice mismatching and also therefore to reduce defects in thin film heterostructures (section 5.2), is to employ a graded approach to compliant layer deposition. Theoretically, a graded layer has the advantage of introducing strain gradually, thus providing the opportunity for any dislocations to move. This progressive introduction of strain has the effect of extending individual misfit dislocations, in turn eliminating their threading segments. The overall result of this is to reduce the density of dislocations that may penetrate into the epilayer.

The chosen materials for the graded compliant layer used in this work are LaN and ScN. The rationale behind this choice is that these rock salt nitrides provide sufficient diversity of lattice parameters within their respective cubic structures. LaN is closer to the Si substrate in lattice constant, 0.530nm whilst ScN is closer to the GaN epilayer in lattice constant, 0.450nm. These two materials are also significantly less electropositive than silicon so will form nitrides in preference to SiN. This will improve the crystal growth as SiN is amorphous and disrupts the epitaxial relationship between substrate and epilayer.

5.4 LaN thin film growth using MOCVD

Prior to conducting experimental LaN growth studies by the MOCVD technique, some modifications to the Electrogas reactor (detailed in Chapter 3) were required. This involved reconfiguring the reactor from an oxide to a nitride reactor. This entailed the porting of an NH_3 gas line in through the reactor manifold system. To ensure the safe handling of NH_3, an ammonia scrubber and detector system had to be fitted to the exhaust system. Other minor modifications were also required to the reactor geometry before the LaN deposition studies could be made.

A La-alkylsilylamido precursor, of the type $La[N(SiMe_3)_2]_3$ was reacted with NH_3 was used to deposit LaN. The growth parameters are shown in Table 5.1. This method was chosen because a sequential transamination reaction should occur prior to film growth leading to an intermediate which breaks down to give the required rare earth nitride on the Si substrate (Scheme 1). The 'Scheme 1' transamination approach is analogous with that employed successfully for the MOCVD of TiN, Zr_3N_4 and Hf_3N_4 using $M[NR_2]_4$ precursors with a large excess of NH_3[14]. Additional recent studies have also demonstrated successful MOCVD growth of Zn_3N_2 using $Zn[N(SiMe_3)_2]_2$ and NH_3 at 275-400°C [15].

$$Ln[N(SiMe_3)_2]_3 + 3NH_3 \longrightarrow Ln[NH_2]_3 + 3(Me_3Si)2NH\uparrow$$

$$Ln[NH_2]_3 \longrightarrow LnN + 3H_2\uparrow$$

(Scheme 1)

Scheme 1. Proposed transamination of $Ln[N(SiMe_3)_2]_3$ precursors

Table 5.1 Growth conditions used for the deposit of LaN by liquid injection MOCVD using $La[N(SiMe_3)_2]_3$

Substrate temperature	150-600°C (Si 111)
Evaporator temperature	160-180°C
Pressure	1-10mbar
Solvent	Toluene
Concentration	0.05M
Argon flow	400 sccm
Ammonia flow	50 sccm
Run time	40min

Deposition of LaN using the 'Scheme 1' transamination reaction involved experiments using a range of substrate, evaporator and fore line temperatures (Table 5.1). Throughout experimentation, reactor pressures were maintained in the range 1-10mbar; NH_3 flow was set to 50sccm and the high-flow Ar carrier gas was maintained at 400 sccm. To achieve the successful transport of the precursor it was necessary to heat the precursor bubbler in order to increase the vapour pressure. It was also necessary to heat the lines from the bubbler to the deposition zone to prevent condensation.

The experimental set up outlined above facilitated the successful transport and decomposition of the precursor onto the Si substrate. However, subsequent EDAX analysis of films deposited at temperatures

ranging from 150-450°C show that they are predominantly composed of La and O. The films were also contaminated with small levels of Si at deposition temperatures up to ~450-500 ° C. At higher temperatures, the films became black in colour, showed reasonable conductivity and contained a high Si content. It seems likely that these films contain a significant lanthanum silicate or possibly lanthanum silicide phase, which is electrically conductive. None of the films analysed showed any evidence for significant levels of N, although it should be noted that the EDAX technique is rather insensitive to such lighter elements and post–deposition exposure of the films to air had occurred. Auger analysis carried out on the same films (Table 5.2) reaffirms this finding. Table 5.2 also demonstrates that the La films have stoichiometries close to that of the sesquioxide and notably that there is no carbon contamination. XRD was also carried out, but due to the thin nature of the films the phase of the La was difficult to ascertain. However, what the XRD measurements do suggest is that the films may have some amorphous content.

Table 5.2 Auger electron microscopy data showing the composition (at%) La films deposited by liquid injection MOCVD using $La[N(SiMe_3)_2]_3$

Sample Label	*Deposition temperature (°C)*	*Etch Time (S)*	*La*	*O*
8	200	10	35.9	64.1
		30	37.2	62.8
		180	36.3	63.7
		300	37.3	62.7
9	200	30	35.1	64.9
		90	35.3	64.7
		180	35.5	64.5
		300	40.7	59.3
16	300	30	37.0	63.0
		60	37.0	63.0
		120	36.7	63.3
		180	36.1	63.9
		300	36.9	63.1

The overall evidence from these results suggests that the transamination reaction was successful. The results demonstrating the low temperature of deposition and the absence of C in the films are particularly promising. They suggest that the transamination reaction between the NH_3 and the lanthanum tris-silylamide proceeds to form a reactive intermediate with the probable formation of a molecule with La-NH_2

bonds. The original hypothesis (see Scheme 1) anticipated the subsequent break down of this intermediate to give the desired LaN, in a manner similar to the established reaction to give TiN. However, the results imply that in the case of the highly reactive La, the intermediate reacts rapidly with trace levels of O containing species in the gas phase, resulting in the formation of the oxide. Alternatively, it is plausible that observed oxide formation was an artefact of leakage in the CVD reactor, which had originally been developed for handling oxide precursors. This possibly reduced the integrity of the equipment and, despite comprehensive leak checking prior to growth runs, small levels of O contamination may not have been eliminated.

Despite yielding some unexpected results, the analyses clearly demonstrate that the process was successful at relatively low temperatures (<200°C), with La_2O_3 deposition observed below 300°C. Such temperatures are considerably lower than those commonly required in CVD deposition of oxide thin films [16]. Indeed, the possibility that the process adopted in the present study may be successfully applied at near–room temperatures should be considered. The wider significance of this observation should not be understated. Firstly, it indicates a possible new route to low temperature deposition of high-κ dielectric thin films. Secondly, the transamination mechanism may be applicable to other transition and rare earth metal oxides, in particular Pr_2O_3. Finally, it should be noted that La_2O_3 also has lattice parameters (4.511Å cubic and 3.9373Å hexagonal) which deem it a potential buffer layer for the growth of epitaxial GaN.

SEM analysis conducted on the La_2O_3 films deposited at substrate temperatures of 200°C and 300°C (Figure 5.6) provides evidence for a significant transition in surface morphology with temperature. The micrograph for the 300°C-grown film (Figure 5.6a) depicts an essentially smooth film containing bubbles distributed sporadically across the surface. These bubbles burst upon contact with the electron beam. EDAX analysis of the burst bubbles show that the Si peak increased suggesting that they had left a hole in the film. In contrast, the film grown at 300°C contained a much more textured surface (Figure 5.6b) which remained stable when placed under the electron beam. The surface roughness of the 200°C deposited film was determined using Atomic Force Microscopy (AFM). Figure 7a shows a scan size of 1.61μm taken at a z range of 100nm, from which the surface roughness was estimated to be 1.273nm. Figure 7b depicts a scan at the z range of 400nm and height 20nm which provides a surface roughness estimation of 1.291nm.

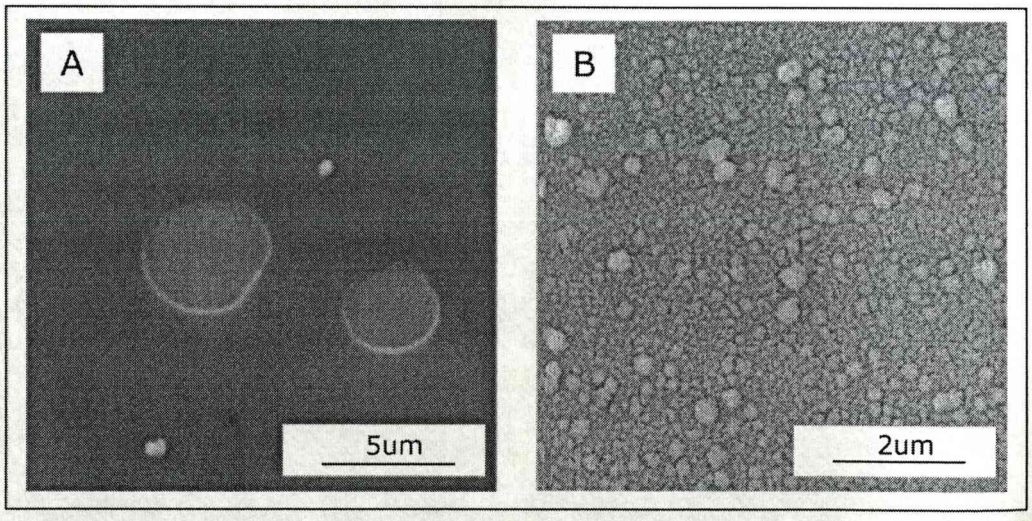

Figure 5.6. SEM micrograph of lanthanum oxide film at 300 °C and lanthanum oxide film at 200 °C

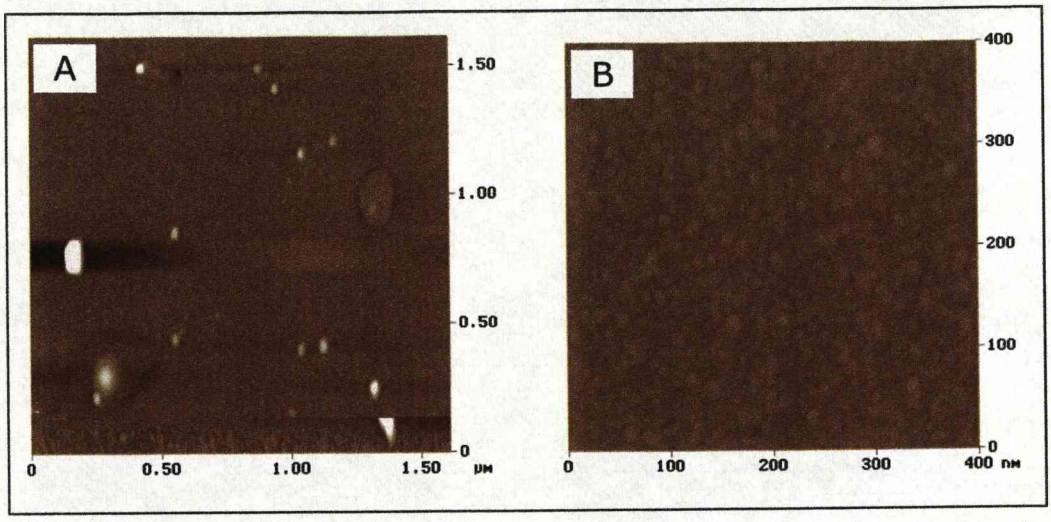

Figure 5.7. Atomic force micrograph of (a) z range 100nm and scan size 1.61μm and (b) z range 400nm and height 20nm

5.6 Molecular Beam Epitaxy of Lanthanum Nitride on Si (111)

Due to the clear difficulties in depositing LaN by CVD techniques, LaN molecular beam epitaxy (MBE) growth runs were carried out in order to assess the stability of the LaN films. An effusion cell containing 99.995% pure La was used as the La source, employing cell temperatures of 1300° to 1400°C. The Si (111) wafers were heated in-situ to 950°C to clean the surface prior to the nitride growth. LaN films were then deposited by employing an 'on-surface' ammonia cracking process at a growth temperature of 800°C. Both LaN and LaN capped with GaN layers were grown, with LaN layers ranging from 20 to 100nm.

However, this deposition procedure produced La films which, when taken out and exposed to air, were observed to change colour over a period of a few minutes. EDAX analysis was carried out on the films and the results

are shown in Figure 5.8. The EDAX clearly shows that once again only La and O are present in the film. This suggests that there is a general stability problem for 'LaN' in the presence of air. Consequently, it was decided to explore this contention further by conducting X-ray analysis on a commercially available sample of LaN powder (source). The results of this analysis (not shown here) suggest that the best fit to the obtained diffraction trace was lanthanum oxide or hydroxide.

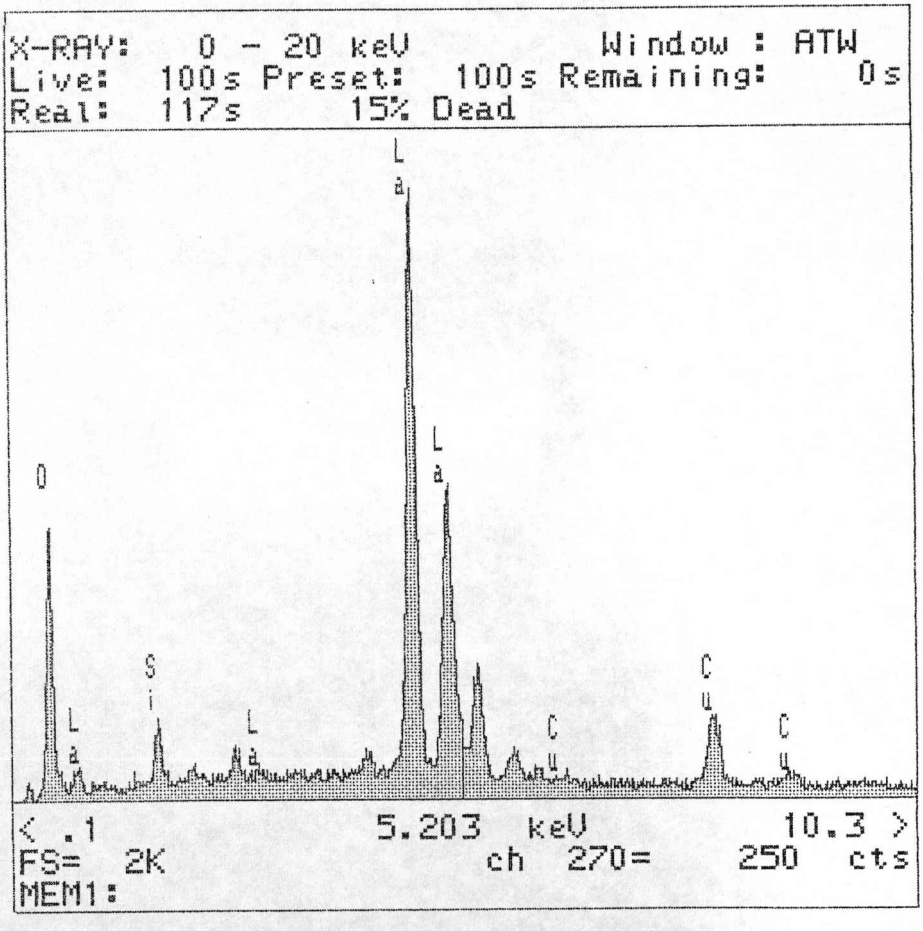

Figure 5.8 EDAX analysis of lanthanum film

An important conclusion from these studies is that LaN appears to be unstable when exposed to air. In this respect, it is difficult to verify whether the successful deposition of this material by CVD- and ALD-type processes is possible, since even if LaN is produced by the reaction it will be degraded to the oxide on exposure to air. However, if it were possible to cap the LaN with a ScN layer in the same system, then the it may be feasible to produce the proposed graded buffer layer. Before MOCVD studies of ScN could begin, preliminary investigations were carried out to ascertain whether or not it would suffer the same drawbacks as LaN. To assess the stability of ScN, it was decided to employ MBE to deposit the thin films, thus ensuring growth within a high integrity environment without any unwanted oxygen species being present.

5.7 Molecular beam epitaxy of Scandium Nitride on Si (111)

The initial MBE growth studies of the ScN thin films were conducted at the University of Liverpool as part of collaborative research with Cambridge University [11]. The assistance of Dr Tim Joyce is acknowledged with the MBE growth studies. Before evaluating the compliancy of the ScN for GaN epitaxy and its potential use as a cap for LaN, the MBE deposition parameters had to be optimised and the resulting film structure characterised.

ScN was deposited on Si (111) substrates using the MBE system described in Chapter 3. For these experiments, a Sc effusion cell, (99.995%) was used as the Sc source. The cell temperatures for the Sc

were systematically varied between 1300 and 1400°C. NH_3 was used as the N source (99.999%) and was passed through a purifying filter before admission to the growth chamber. The Si substrates were annealed at 950°C for 1h in UHV prior to growth in order to volatilise any native oxide that may have been present on the Si surface. The wafer was rotated at 60rpm throughout growth to produce an even film deposition. A range of substrate growth temperatures between 600 and 1000°C were investigated to identify the optimum growth temperature. All films had a thickness of 225± 15nm using a deposition rate of 100nm h^{-1}.

XRD was employed to determine the orientation relationships between the film and substrate. Figure 5.9(a) shows the integrated intensity under the ScN (111) peak versus the film growth temperature and (b) shows a plot of the full width at half maximum (FWHM) of the rocking curve (ω-scan) across the (111) ScN peak. The results reveal that the trend in film crystallinity varies with deposition temperature and that the optimum ScN growth temperature lies around 850°C.

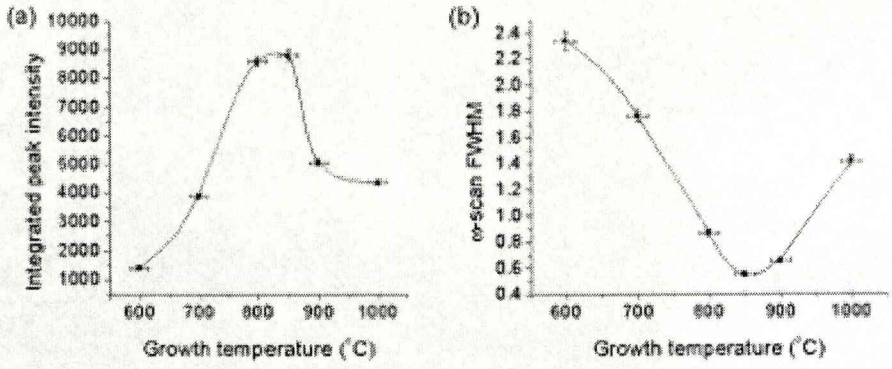

Figure 5.9. (a) Plot of the integrated intensity under the ScN (111) peak) versus film growth temperature. (b) Plot of the full width at half maximum (FWHM) of the rocking curve (ω-scan) across the (111) ScN peak[11]

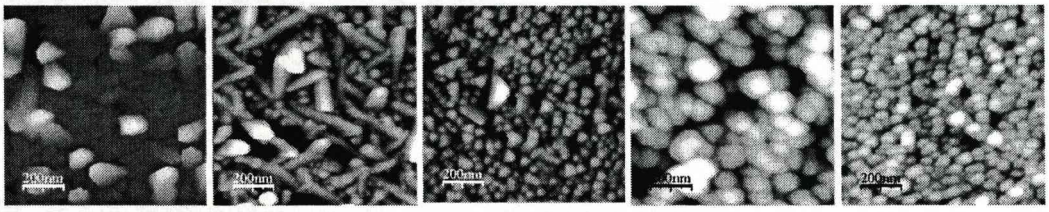

Figure. 5.10. AFM images of ScN films grown at (a) 600°C, (b) 700°C, (c) 800°C, (d) 900°C and (e) 1000°C[11]

The deposition temperature was found to not only affect the crystallinity of the films but also their surface morphology. AFM was used to elucidate the influence of crystallinity on surface morphology and Figure 5.10 illustrates four micrographs of films grown in the temperature range of 600 to 1000°C. It is clear that uniform growth was limited to temperatures above 800°C. The same affect on morphology is seen if films were grown under low NH_3 flow rates. This is caused by the occurrence of Sc-rich growth at low temperatures due to the limited NH_3

cracking efficiency. It can therefore be stated that the films grown at the optimal temperature of 850°C are likely to have been grown under near-stoichiometric conditions. Derived surface roughness values also decrease with increasing growth temperature (Figure 5.11), which is attributable to an increase in the adatom mobility.

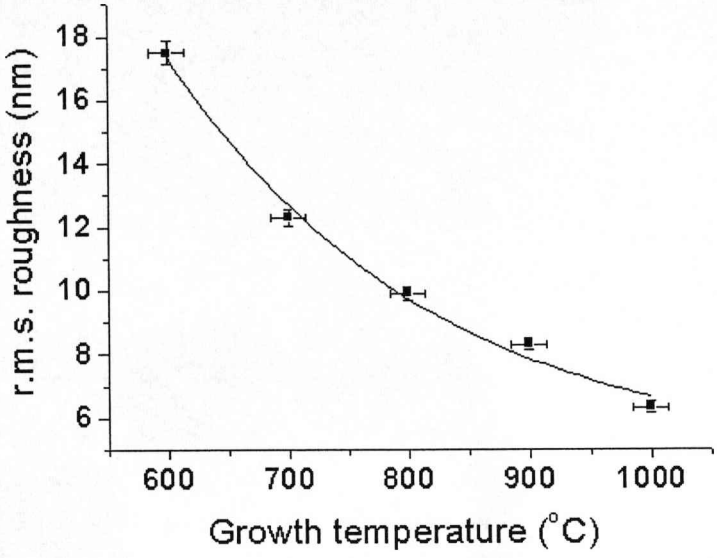

Figure 5.11. Plot of rms surface roughness versus growth temperature. Line represents a first-order exponential fit

Figure 5.12 presents a TEM cross-sectional image of a ScN film deposited at the optimised temperature. A columnar structure is apparent, within which individual columns are clearly outlined with sharp facets. It has been demonstrated previously that ScN films with a (111) surface have much lower adatom mobility than films with a (100) surface [17]. This relatively low adatom mobility arises from the high density of dangling bonds on the (111) surface, which causes the formation of the columnar microstructure [18]. Although columnar in structure, the grown films were

of a high crystallinity as demonstrated from the single crystal pattern of the selective area diffraction (SAD) shown in Figure 5.12(b). A number of SAD patterns were taken across the interface region of the film and substrate and no other ScN orientation were observed. The SAD patterns demonstrate an epitaxial relationship between the ScN and Si substrate, which is described by $(111)_{ScN}//(111)_{Si}$ and $[1\ \bar{1}0]_{ScN}//[0\ \bar{1}1]_{Si}$.

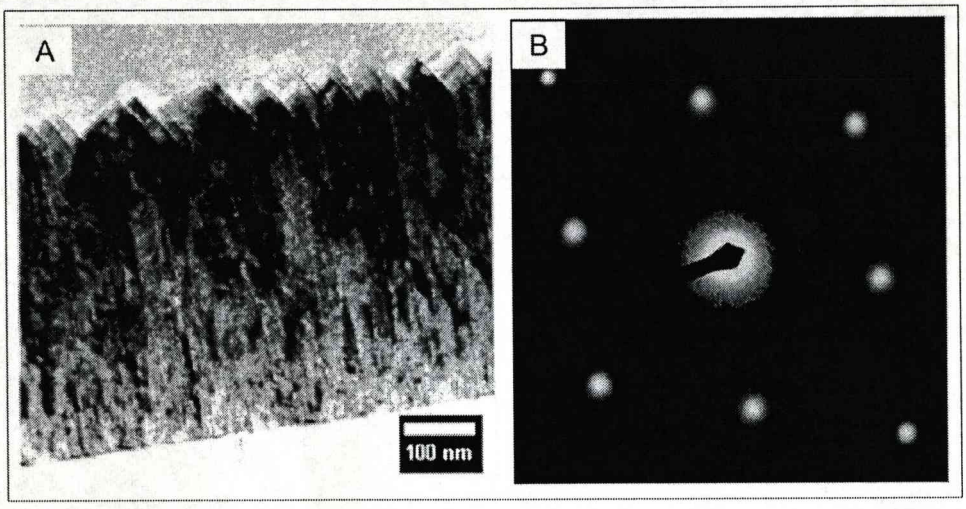

Figure 5.12. (a) Cross-sectional TEM bright field image of a ScN layer grown at 850°C. (b) Selected area diffraction pattern along the [01 $\bar{1}$] zone axis

5.8 GaN/ScN/Si(111) MBE

Having addressed the question of optimisation and stability of the ScN buffer layer deposition, MBE growth runs were carried out to determine their viability as compliant layers for the deposition of epitaxial GaN. ScN films were grown at the optimised temperature of 850°C, with film thicknesses ranging from 20 to 40nm. ScN growth was initiated using one to two monolayers of Sc before admitting NH_3 at a flow rate of

40sccm. Upon reaching the desired thickness of deposited ScN, the Sc cell was shuttered off, the Ga cell shutter then opened, and GaN growth initiated at a deposition temperature of 850°C. The GaN growth was continued until the epilayers obtained thicknesses in the order of 50 to 500 nm. TEM and XRD techniques were employed to resolve film microstructure and crystallinity of the films, SEM to study GaN micro-morphology.

The XRD pattern of a GaN/ScN/Si sample is shown in figure 5.13. The sample consists of ScN and GaN layers of thickness of 25nm and 500nm respectively. Only one reflection, at 34.4° (2θ), is observed. The coincidence of the GaN (0002) reflection is difficult to discern from the XRD pattern since it occurs close to this value of the ScN(111) layer (34.7°). However, Raman analysis for the same film shows clearly the presence of the GaN over layer (Figure 5.14). The FWHM of the GaN Raman peak, observed at 565cm^{-1} (E_2 mode), provides a good indication of the crystalline quality of the material. Figure 5.15 shows a TEM cross-sectional image of the sample in which the GaN/ScN layers are viewed from the Si <110> direction. SAD measurements of this cross-section indicate the following orientations: GaN [0001] // Si [111] and GaN(1 $\bar{1}$00) // Si(11 $\bar{2}$).

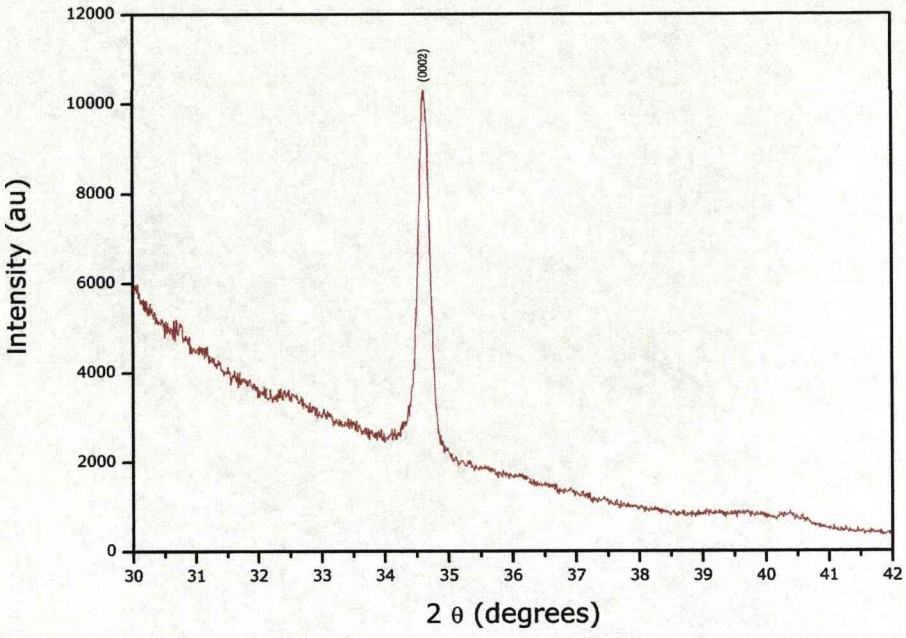

Figure 5.13 X-ray diffraction analysis of a GaN/ScN/Si (111) film

Figure 5.14 shows the Raman spectrum of a GaN layer on a ScN/Si (111) substrate. The face centered cubic symmetry of the scandium nitride rock salt structure makes any first-order Raman transition symmetry forbidden, however the *q*-selection rule is relaxed in the presence of defects. Consequently the Raman spectrum reflects a weighted phonon density of states which is a maximum towards the zone edges. A broad band of intensity with peaks at 361, 382 and 426cm^{-1} was attributed to the LA/TA phonon range. A further peak at 630cm^{-1} was assigned to the TO/LO optical phonon range. These assignments are consistent with those of Zheng et al [19] who have recently reported Raman measurements on ScN bulk crystals grown via a resublimation method. Similarly, Travaglini et al [20] have published values of 354 and 413cm^{-1} for the acoustic phonon spectrum of ScN and 676cm^{-1} for the optical phonon range.

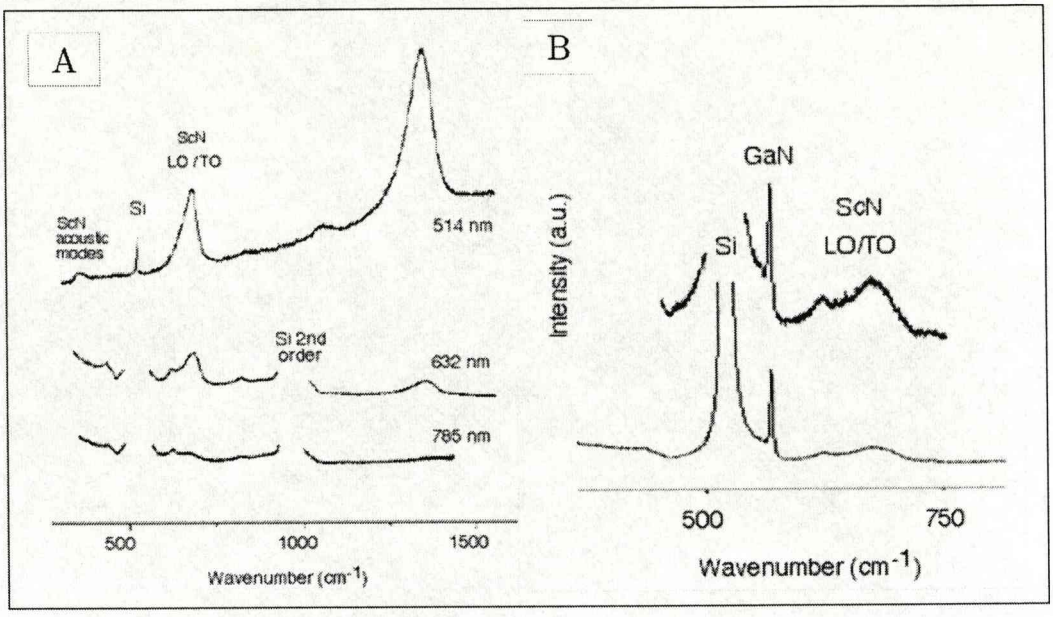

Figure 5.14. Raman analysis of (a) a ScN buffer layer on silicon measured at 514, 632 and 785nm excitation; (b) a GaN/ScN/Si(111) film

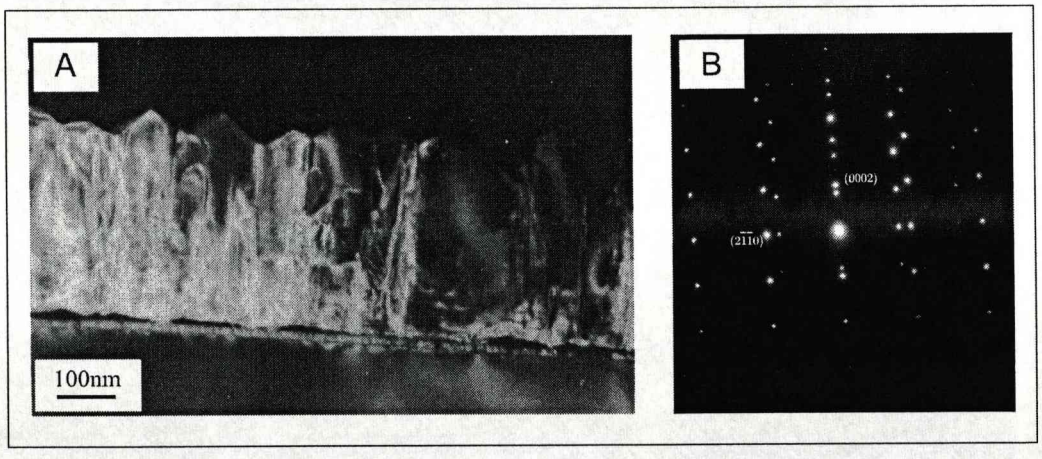

Figure 5.15. (a) Cross-sectional TEM image of GaN/ScN layers and (b) Selective area diffraction pattern.

In order to evaluate the nano-metre scale chemical structure of the interface, scanning transmission electron microscopy (STEM) was carried out on this sample (Figure 5.16). The first image (Figure 5.16a) shows a bright field image, highlighting the columnar microstructure of the ScN

layer. As previously stated, such columnar growth in the GaN layer is due to the low adatom mobility. A second layer is observed running through the interface between the GaN and ScN, above which is the GaN, that also has a columnar growth habit with a column diameter of 160nm±30nm. Elemental mapping using EDX analysis was used to ascertain the composition of each layer. It shows that the seam running through the GaN/ScN interface is oxygen rich and accompanies delaminating of the GaN epilayer from the ScN. Although the elemental mapping only shows the presence of O and no other element in the interface, it is unlikely that this is the case. If the layer comprised only of Oxygen gas it would escape out of the film again back up the GaN grain boundaries. Therefore it is more likely to be a solid Sc_xO_x or $Ga_XSc_xO_x$ layer, which may explain why spalling of the film is observed with increasing GaN layer thickness.

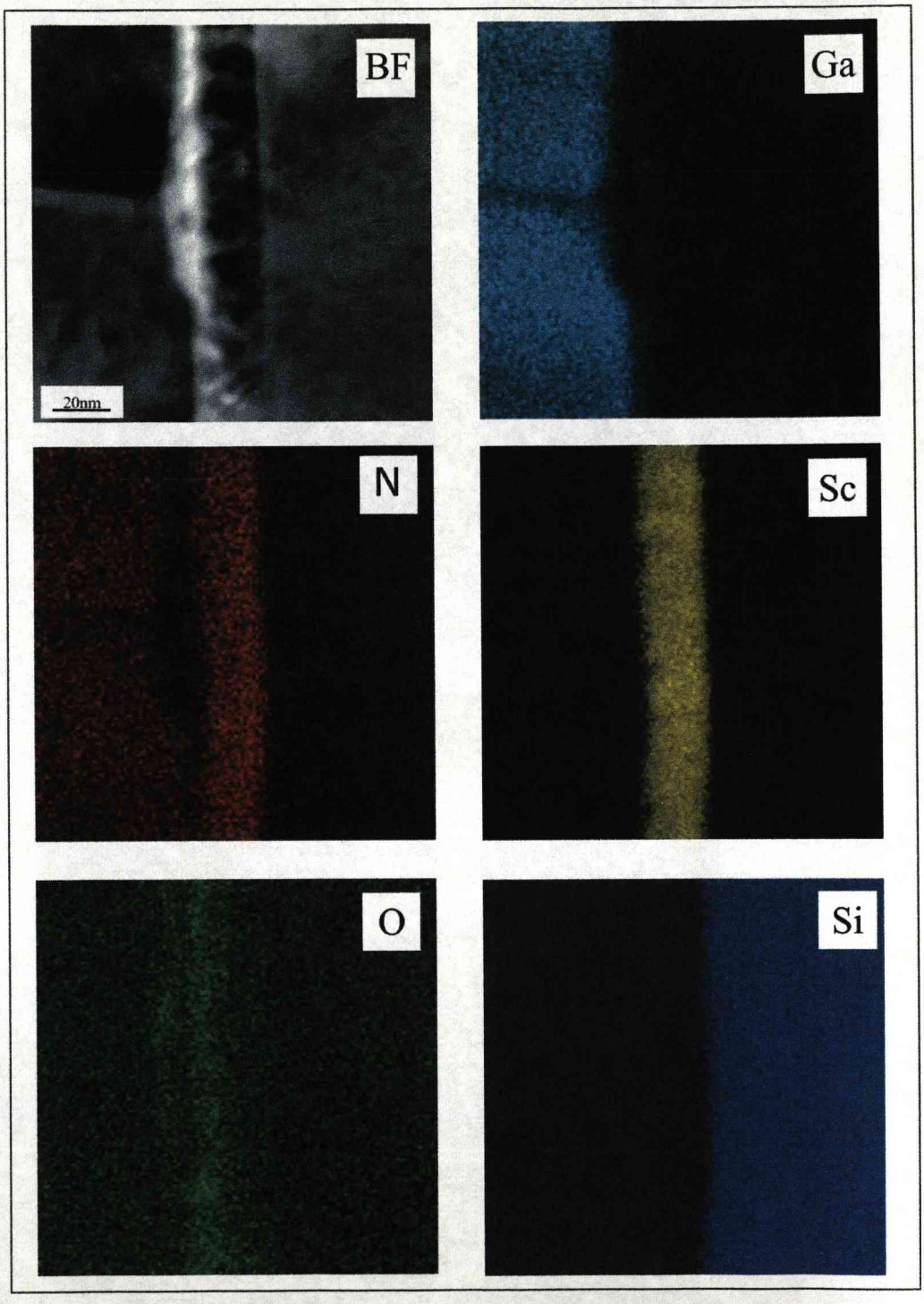

Figure 5.16. STEM bright field image and elemental mapping of a GaN/ScN/Si film

1.9 MOCVD growth of ScN

Having demonstrated the possibility of successfully depositing epitaxial GaN on ScN, without the instability problems found to exist for LaN, it is now desirable to investigate an alternative - MOCVD - growth route for ScN. Initial attempts to deposit ScN from the Sc analogue of the La precursor involved demonstration of the transport of the precursor from a bubbler to the deposition zone. The expected gas-phase transamination between $Sc[N(SiMe_3)_2]_3$ and NH_3 is shown in scheme 2.

$$Sc[N(SiMe_3)_2]2\ (NH_2) + (Me_3Si)2NH$$

$$Sc[N(SiMe_3)_2]\ (NH_2)2 + (Me_3Si)2NH$$

$$Sc(NH_2)3 + (Me_3Si)2NH$$

$$Sc(NH_2)3 \rightarrow ScN$$

(Scheme 2)

Scheme 2. Gas-phase transamination.

To investigate transportation of the precursor an initial set of standard reactor parameters were chosen which employed a vaporiser temperature of 170°C. A reactor vessel pressure of 1 mbar was used with a flow of argon carrier gas of $500cm^3/min$. Under these conditions, the $[ScCl_2\{N(SiMe)_3\}_2(THF)]$ precursor was observed to decompose in the vaporiser, suggesting that the thermal stability of the precursor again required a lower vaporiser temperature. Subsequently, lower vaporiser temperatures were systematically reduced down to a lower limit of 50°C. For these experiments a reactor vessel pressure of 1 mbar was used

throughout, together with a flow of argon carrier gas of 500cm^3/min. In each case, the $[ScCl_2\{N(SiMe)_3\}_2(THF)]$ decomposed in the vaporiser leaving a residual by-product. Attempts were then made to deposit films using the vaporiser at room temperature with a maximum chamber pressure of 3 mbar coupled with a maximum argon flow rate of 1000cm^3/min. At injection rates up to 4 cm^3/h the $[ScCl_2\{N(SiMe)_3\}_2(THF)]$ was still found to condense in the vaporiser. Upon conclusion of these experiments, samples of $[ScCl_2\{N(SiMe)_3\}_2(THF)]$ in toluene solution were observed to decompose in the flask over a period of 3 to 4 days.

Given the low vapour pressures of the precursor, a final attempt was made to deposit a film by heating the bubbler and lines. Under these growth parameters very thin films were observed to be deposited on to the Si substrates. Unfortunately, AES analysis revealed that the films had formed the oxide rather than the nitride. Due to the thin nature of the films, XRD analysis was unsuitable for the determination of the phase of the films.

In summary, these investigations indicate that the Sc precursor has insufficient volatility coupled with poor stability. In part, the failure to deposit nitride films is partly attributable to the reactor geometry and the lack of integrity of the equipment, which probably contributed to small amounts of oxygen contamination. For both La and Sc, the formation of the oxide in preference to the nitride is borne out by the thermodynamic data for the enthalpies and free energies of formation

(Table 5.3). One practical implication of this is that the production of graded layers composed of LaN and ScN will probably require the application of high-integrity, custom designed MOCVD reactor systems.

Table 5.3. Enthalpies and free energies of formation of scandium oxide and nitride

Compound	ΔH°_f *(kJ mol^{-1})*	ΔG°_f *(kJ mol^{-1})*
LaN	-304.2	-270.8
La_2O_3	-1793.8	-1254.2
ScN	-284.6	-253.2
Sc_2O_3	-1872.2	-1783

5.10 Conclusion

Experiments have been made to deposit LaN on Si(111) using a Ln-alkylsilylamido precursors of the type $La[N(SiMe_3)_2]_3$. It was hoped that a sequential transamination reaction would occur prior to film growth, which would lead to an intermediate that would yield the required rare earth nitride on the substrate. The transamination reaction is demonstrable as low temperature deposition is achieved and there is no sign of silicon or carbon present in the films. Unfortunately analysis of the films by AES shows that La_2O_3 had been deposited in preference to the nitride. This is due to the enthalpy and free energy of formation of the La which favours the oxide over the nitride. The lack of equipment integrity also hampers the nitride growth as it probably suffers small amounts of oxygen contamination. However the innate instability of the

La is proven as MBE growth studies show that the nitride spontaneously transforms to the oxide.

MBE studies for ScN have demonstrated that it does not suffer from the same stability issues as La. XRD analysis reveals that there is a trend in film crystallinity which varies with deposition temperature. The optimum growth temperature for ScN is around 850°C. Selective area diffraction patterns reveals an epitaxial relationship between the ScN and Si substrate, which is expressed as $(111)_{ScN}//(111)_{Si}$ and $[1\ \bar{1}0]_{ScN}//[0\ \bar{1}1]_{Si}$.

The growth of gallium nitride on optimized ScN layers has been explored. SAD measurements indicate that the following orientations occur in the structure: GaN [0001] // Si [111] and GaN(1 $\bar{1}$00) // Si(11 $\bar{2}$).

MOCVD studies have been investigated using the precursor $Sc[N(SiMe_3)_2]_3$ in the presence of NH_3 to deposit thin films of ScN. Regrettably the precursor has insufficient volatility and poor thermal stability. Again the oxide formation was favoured over the nitride probably due to air leaks in the equipment. If the deposition of ScN using this growth technique and precursor combination is to be realised, a high-integrity, custom designed MOCVD reactor system will be required.

References:

1 Liu L. and Edgar J.H. 2002 *Material Science and Engineering. R* **37** 61.

2 A.R.Smith, H.A.H.Al-Brithen and D.C.Ingram 2001 *Journal App.Phys.***V90**. 4

3 X. Bai, Doctoral Dissertation, Ohio University, November 2000; X. Bai and M. E. Kordesch, *Appl. Surf. Sci.* **175–176**, 499 2001

4 D. Gall, I. Petrov, P. Desjardins, J.E. Greene, Journal. Appl. Phys. 86 (1999) 5524.

5 R. Monnier, J. Rhyner, T. M. Rice, and D. D. Koelling, *Phys. Rev. B* **31**, 5554 (1985).

6 C. Stampfl, W. Mannstadt, R. Asahi, and A. J. Freeman, *Phys. Rev. B* **63**, 155106 (2001).

7 J.P. Dismukes, W.M. Yim, V.S. Ban, *J. Cryst. Growth* 13–14 (1972) 365.

8 H. Al-Brithen, A.R. Smith, *Appl. Phys. Lett.* 77 (2000) 2485.

9 T.D. Moustakas, R.J. Molnar, J.P. Dismukes, ECS Proc. 96–11 (1996) 197.

10 D. Gall, I. Petrov, L.D. Madsen, J.-E. Sundgren, J.E. Greene, *J. Vac. Sci. Technol.* A **16** (1998) 2411.

11 M.A. Moram, T.B. Joyce, P.R. Chalker, Z.H. Barber, C.J. Humphreys. *Applied Surface Science* **252** (2006) 8385–8387

12 J. O. Williams, E. S. Crawford, J. LL. Jenkins, T. L. NG, A. M. Patterson, M. D. Scott, B. Cockayne and P. J. Wright. J.Materials Science Letters **3** (1984) 189-193

13 F. Perjeru, X. Bai, M.I. Ortiz-Libreros, R. Higgins and M.E. Kordesch. *Applied Surface Science* **175-176** (2001) 490-494

14 R. Fix *et al, Chem. Mater.,* 1991, **3,** 1138

15 R. Fischer *et al. Chem. Vap. Deposition,* **2005**, *11,* 409

16 A. Abrutis, M. Lukosius, Z. Saltyte, R. Galvelis, P.K. Baumann, M. Schumacher, J. Lindner. Thin Solid Films Volume **516**, Issue 15 (2008) 4758-4764

17 Arthur R. Smith, Hamad A. H. Al-Brithen, David. C. Ingram, Daniel Gall, *J. Appl. Phys.* **90** (2001), p.1809

18 W. C. Oliver and G. M. Pharr, *J. Mater. Res.* **7** (1992) p.1564

19 Zheng Gu, J.H. Edgar, J. Pomeroy, M.Kuball and D.W. Coffey, J. Mater. Sci.: Mater. In Electronics 15 (2004) 555 – 559

20 G. Travaglini, F. Marabelli, R. Monnier, E. Kaldis and P. Wachter,Phys. Rev. B 34 (1986) 3876

Chapter 6 Zinc Oxide

Overview

The atomic arrangement of zinc oxide layers on silicon substrates is discussed. The effects of lattice mismatch and resulting polarity of the ZnO layer are both significant factors in the subsequent growth of gallium nitride and are considered here.

The MOCVD of zinc oxide onto silicon substrates using two precursors is presented, namely dimethyl zinc – tetrahydrofuran and bis(2,2,6,6-tetramethyl-3,5-heptanedionate) zinc. The microstructure of the resulting layers is investigated and found to be quite different for the two systems.

The subsequent molecular beam epitaxy of gallium nitride onto the various ZnO buffer layers is investigated. An adverse interaction of excessive free gallium is observed which, is a significant issue in the use of this oxide as a compliant buffer layer.

Chapter 6

Zinc Oxide

6.1 Background and rationale

The previous results chapters have focused on the use of closely lattice-matched monocrystalline/amorphous and graded compliant layers for the deposition of epitaxial GaN. However, if the requirement for close lattice matching to both substrate and target material is relaxed, then it should be possible to employ single material films as alternatives. One such material, zinc oxide (ZnO), has been the subject of intensive study over several decades in the opto-electronics industry [1]. ZnO is a wide band-gap II-VI semiconductor (E_g = 3.37 eV) with piezoelectric properties. A variety of applications for ZnO thin films already exist, including amongst others light emitting diodes [2], photodetectors [3], solar cells [4] and surface acoustic wave filters [5]. ZnO has been grown by a variety of techniques, including radiofrequency or magnetron sputtering [6,7], spray pyrolysis [8], MBE and MOCVD [9,10]. However, the MOCVD growth studies have proved to be relatively unsuccessful and as yet no attempt has been made to deposit ZnO on Si(111) substrates – both clear prerequisites for commercially viable GaN/ZnO/Si buffer layer technologies. Addressing these issues provides the background rationale for the experimental studies reported in this chapter.

The value of ZnO as a compliant layer rests on several characteristics of its lattice structure. These properties are dealt with in section 6.2, which

provides an initial detailed description of the ZnO lattice structure and subsequently outlines the possible interfaces that may result with the Si (111) substrate and the GaN overlayer.

6.2 Interface structures of GaN/ZnO/Si(111)

ZnO has a hexagonal wurtzite structure, which consists of two hexagonal-close-packed (hcp) interconnecting sublattices of Zn^{2+} and O^{2-}. Each Zn ion is surrounded by a tetrahedron of O ions and vice-versa. The tetrahedral coordination gives rise to polar symmetry along the hexagonal axis. The unit cell for this crystal is shown in Figure 6.1.

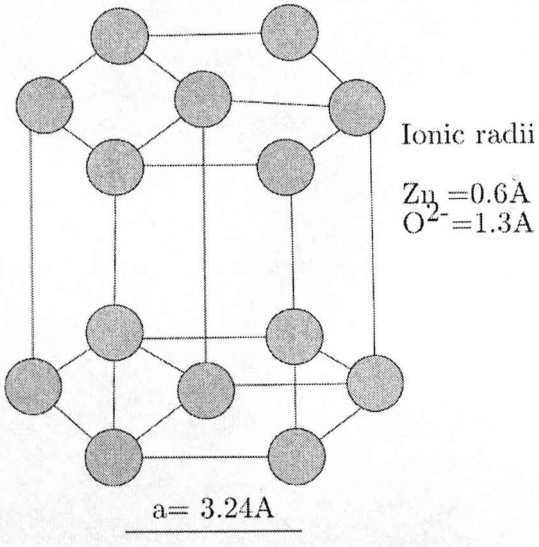

Figure 6.1. The unit cell of Zinc Oxide

The ZnO crystal has a hexagonal unit cell with two lattice parameters, a=3.24Å and c=5.20Å in the ratio of c/a=$\sqrt{8}/3$= 1.633. This wurtzite structure consists of triangularly arranged alternating bi-atomic close-packed (0001) planes, e.g. Zn and O pairs. Therefore the stacking

sequence of the (0001) plane is ABAB... in the <0001> direction. The structure lacks inversion symmetry and so gives rise to crystallographic polarity, which indicates the direction of the bonds. For example, if the structure is Zn-terminated then the direction would be <0001>, whereas for O terminated the direction would be <000 $\bar{1}$> (Figure 6.2).

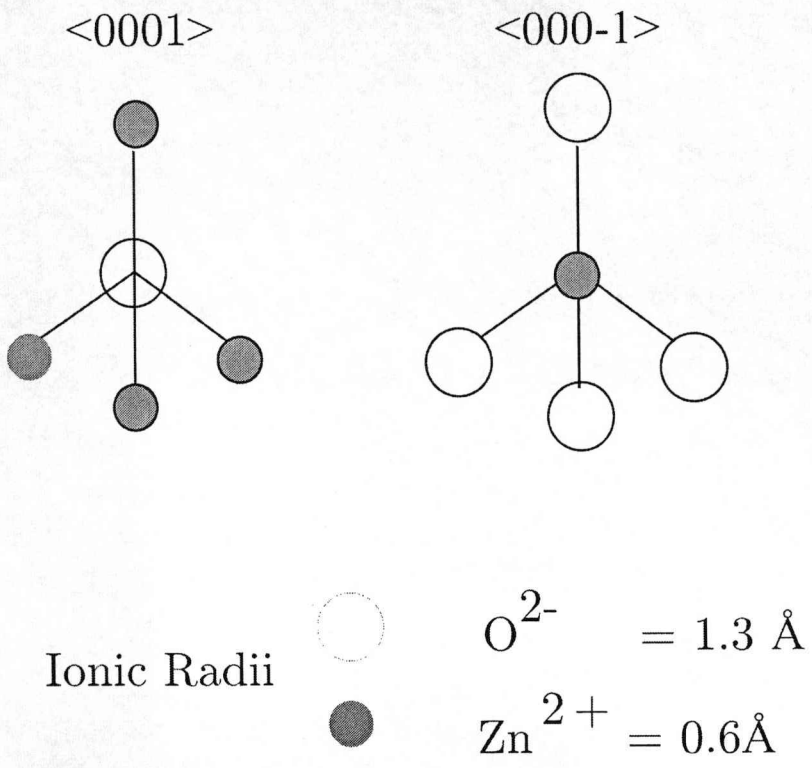

Figure 6.2. Zn and O terminated zinc oxide

As stated previously earlier, silicon consists of a diamond fcc-like structure, whereby each Si atom bonds to four other Si atoms. When considering the deposition of wurtzite ZnO onto a Si surface, one geometry is with its hexagonal basal plane perpendicular to the Si (111)

substrate. The orientation or polarity is either <0001> or <000 $\bar{1}$> growth direction. Figure 6.3 shows the two main polarities for ZnO.

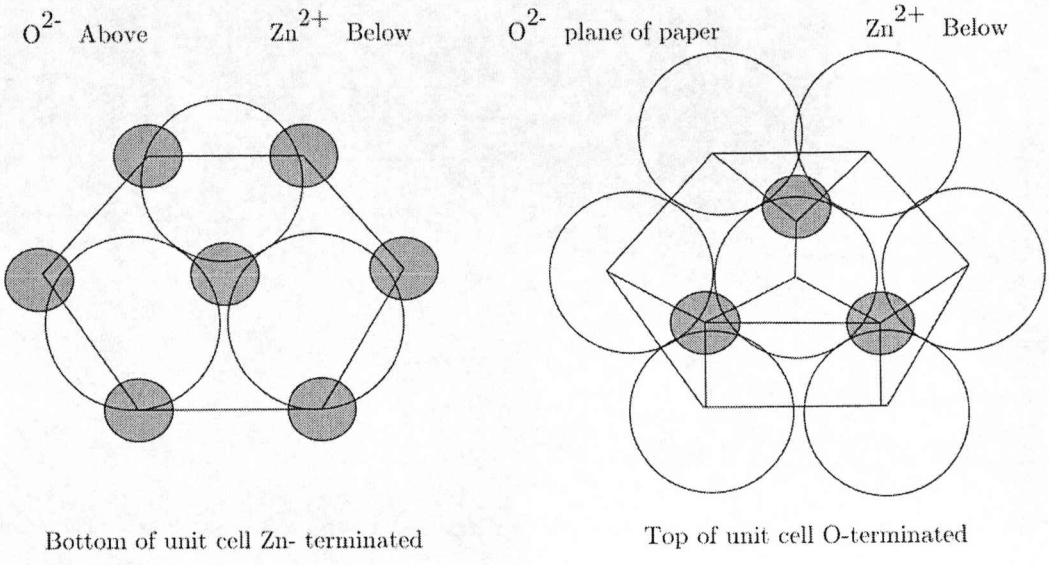

Figure 6.3. The two main orientations/polarity of ZnO

The stacking sequence for the hcp ZnO will be ABAB or ACAC with the basal plane (0001) or (000 $\bar{1}$), whereas for the fcc Si the sequence would be ABCABC. However, if using (111) Si the stacking sequence would then become ABAB. Therefore, if the assumption is made that Si is at "A" positions, the ZnO wurtzite unit cell can sit at "B" or "C" positions. If Si is at "B" then further stacking would be ABABAB or if C the ACACAC stacking would be observed. Figure 6.4 shows the plan view schematic of ZnO on Si (111).

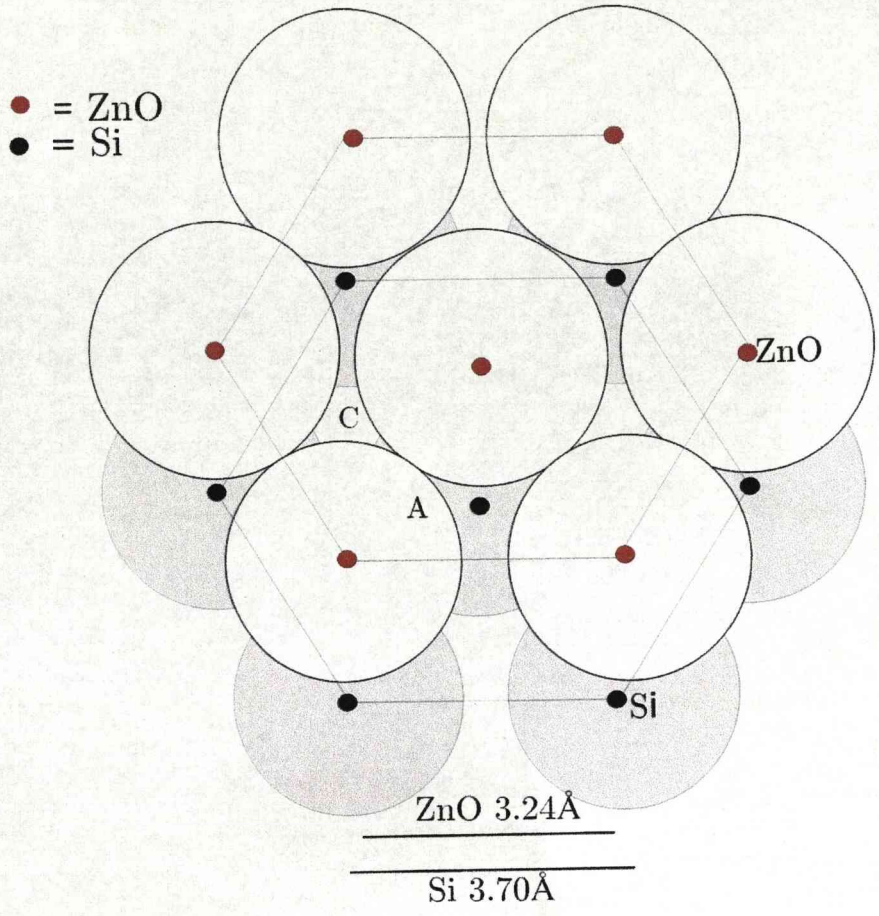

Figure 6.4. Plan view of ZnO on Si(111)

Equation 6.2 outlines the calculation of the theoretical lattice mismatch between ZnO and the underlying Si substrate. The interatomic spacing on the (111) plane of the Si is 3.8Å and the spacing for ZnO is 3.24Å, giving rise to an expected lattice mismatch between the two materials of 14%. Having established the theoretical lattice mismatch between the underlying Si and the ZnO, it is now necessary to resolve the mismatch between ZnO and the overlying GaN.

$$\left[\frac{(a_{Si\sqrt{}}2/2) - (a_{ZnO\sqrt{}}2/2)}{(a_{ZnO\sqrt{}}2/2)}\right] \times 100 \qquad \text{(equ. 6.2)}$$

$$= \left[\frac{(3.7 - 3.24)}{3.24}\right] \times 100$$

$$= 14\ \%$$

The lattice mismatch which arises from the GaN and ZnO interface is much smaller than that of the ZnO/Si(111) interface. The interatomic spacing of the GaN (3.19Å) and ZnO (3.24Å) gives rise to a lattice mismatch of 1.5% between the two materials. The stacking arrangement of GaN onto the ZnO compliant layer is ABABAB. Using the assumption that the ZnO is O-terminated, the first atoms to be deposited onto the ZnO would be Ga and the GaN would be N-terminated. This arrangement is illustrated in Figure 6.5.

This geometrical analysis leads to the working hypothesis that GaN/ZnO/Si may be successfully combined. In view of this, it was decided to test this idea by conducting experimental MOCVD growth studies.

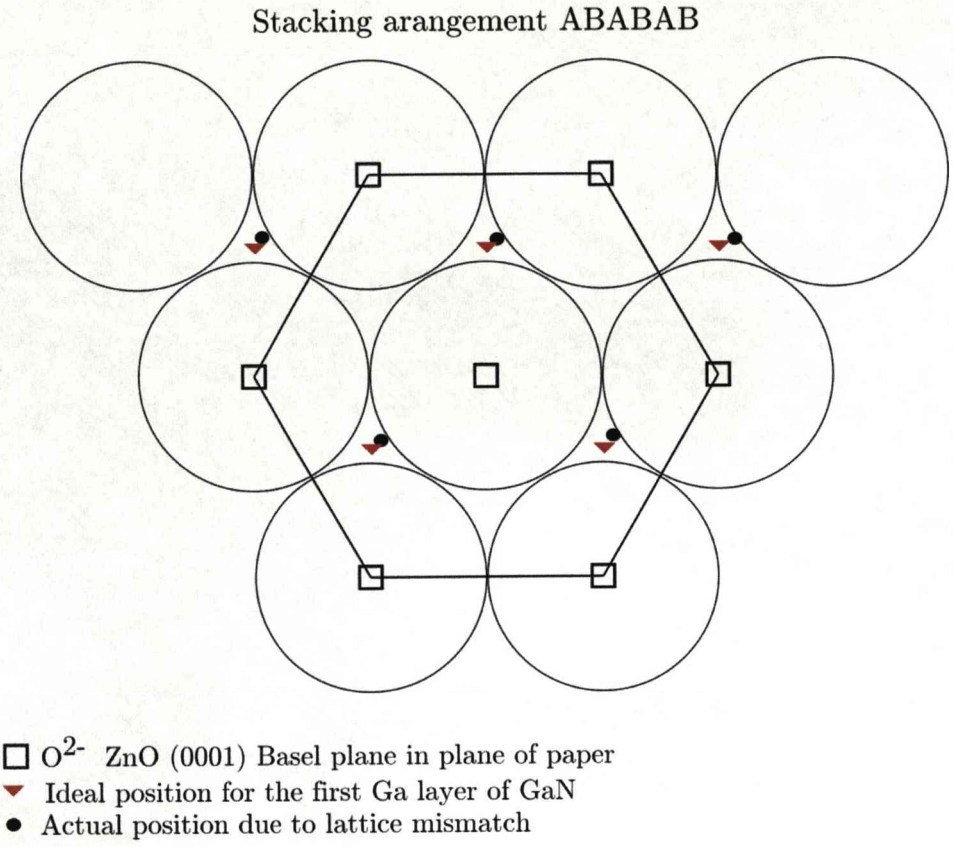

Figure 6.5. Plan view of GaN on ZnO.

6.3 Zinc Oxide MOCVD using dimethyl zinc – tetrahydrofuran

For a commercially viable [GaN / ZnO / Si] buffer layer technology, it is clearly desirable to develop an MOCVD process which is compatible with the existing GaN MOCVD technology. A number of precursors have previously been used for the MOCVD of ZnO, but many have drawbacks associated with them. For example, the β-diketonate $[Zn(thd)_2]$ (thd = 2,2,6,6-tetramethyheptane-3,5-dionate) [11] and the tetrameric complexes $[MeZn(OR)]_4$ [OR = OPr^i, OBu^t] [12] are both characterised by low vapour pressures, which in turn results in low ZnO growth rates. Dialkyl zinc

compounds, such as [Et_2Zn] [10] and [Me_2Zn] have also been commonly employed [13] with alcohol or water. Unfortunately, those compounds undergo serious pre-reactions with oxygen, leading to heavy particulate contamination that can cause blockages in the reactor inlet lines. Such pre-reactions can be minimised by the use of less reactive oxygen sources, such as N_2O [14] or NO_2 [15]. However, all of these sources have generally proved to be unsatisfactory, yielding only very low ZnO growth rates. In MOCVD, the use of Lewis-base adducts of group III and group II alkyls is a proven method for reducing pre-reaction with a highly reactive co-precursor such as the dialkyl compounds [16-17].

Table 6.1. Growth conditions used to deposit ZnO films by liquid injection MOCVD using [Me_2Zn(THF)]

Substrate Temperature	350-550°C on Si(111)
Evaporator Temperature	50°C
Reactor Pressure	5mbar
Precursor solution injection Rate	30cm^3 /hr
Solvent	nonane
Concentration	0.05M
Argon flow	200 cm^3min^{-1}
Oxygen flow	100 cm^3min^{-1}
Run time	10 min

It was therefore decided to investigate the deposition of ZnO by liquid injection MOCVD using the adduct [$Me_2Zn(THF)$] in the presence of O_2. The growth runs were conducted using the parameters set out in Table 6.1, and involved depositing ZnO films of variable thickness at a range of temperatures.

Figure 6.6 plots the relationship between the substrate temperature and the ZnO growth rate. It demonstrates that that the ZnO growth rate increases within the substrate temperature range of 350-495°C. This temperature range corresponds to the region of kinetic control, within which film growth is dominated by thermal decomposition of the precursor on the substrate. Above this kinetically controlled region of growth, there is a very narrow region of diffusion-controlled growth occupying the 495-525°C temperature range. The ZnO growth rate peaks at around 200nm within this diffusion-controlled region (Figure 6.6). The ZnO growth rate shows a steep decline with increasing temperature above 525°C, reflecting the thermal depletion of the precursor onto the reactor walls.

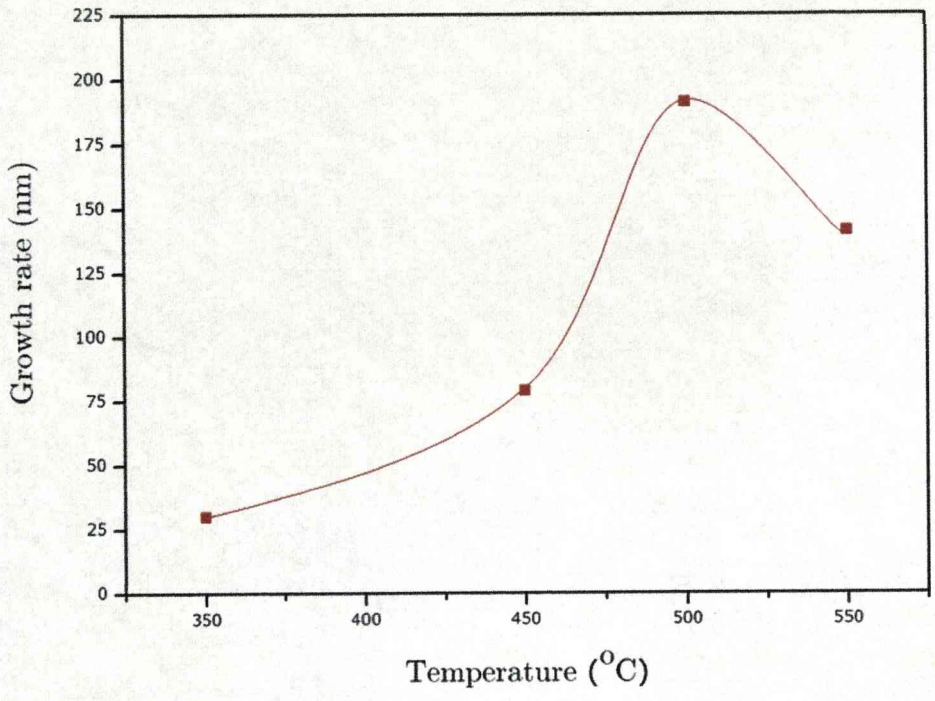

Figure 6.6. Variation of ZnO growth rate with substrate temperature

The composition of the MOCVD-grown ZnO films was determined using Auger Electron spectroscopy (AES), the results of which are presented in Table 6.2. The data suggests that the films are essentially stoichiometric ZnO, and that carbon is absent from the films at an estimated detection limit of ~0.5 at%. The purity of these films is highly comparable with previously published purity data for ZnO films grown from base-free R_2Zn precursors [12].

Table 6.2. Composition of the ZnO films (at %) determined by AES

Sample No.	*Growth temperature*	*Zn*	*O*	*Zn / O ratio*
1088	350°C	50.2	49.8	1.00
1090	500°C	50.0	50.0	1.00
1097	500°C	50.4	49.6	1.02
1099	450°C	51.5	48.5	1.06

The surface microstructure of a ZnO film deposited at 450°C is shown in the scanning electron micrograph in Figure 6.7(a). The image shows that the film consists of an array of truncated ZnO needles with an aspect ratio of length to diameter of less than one, which is consistent with a relatively low deposition rate at sub-optimal growth temperature. By comparison, the image of a ZnO film deposited at the growth temperature of 500°C is shown in Figure 6.7(b). This film has a microstructure consisting of a much higher aspect ratio (>50) nanowire-like morphology, with an average needle diameter of 17nm. A number of growth runs were performed to confirm that the nanowire aspect ratio can be adjusted significantly by varying the substrate temperature by only 50°C. The mechanism accounting for this radical change in growth habit can only be speculated; however previous work by Griffiths et al [18]

has shown that deposition from DMZ(THF) without any other oxygen source led to the deposition of ZnO. This would suggest that the terahydrofuran adduct is able to play some part in providing oxygen to the growing film. In the work presented here, oxygen was added during growth, however our hypothesis is that the adduct molecule influences the surface mobility of the DMZ adsorbate. It is suggested that the modified mobility leads to the formation of islands which subsequently act as nuclei for nanowire growth. A similar observation has been made by Quanchang Li et al [19] in the ALD growth of ZnO on silicon from diethyl zinc (DEZ) using water as an oxidant. They observed the formation of 100nm diameter ZnO islands, which were subsequently used to grow nanowire structures using a liquid phase process.

The narrow temperature window for nanowire growth might be explained in the following manner. At substrate temperatures above 550 ° C the DMZ(THF) precursor undergoes gas-phase decomposition and the THF by-product plays no part in the surface chemistry. Below 500 ° C the DMZ(THF) precursor adsorbs and the surface mobility is hampered by insufficient thermal energy. Only in the temperature range 450 ° C to 500 ° C is sufficient mobility achieved for the adsorbate to nucleate via a Frank – van der Merwe growth (see Chapter 2) type mechanism. Although speculative, this trade-off between competing growth processes is the only ready explanation to account for the growth habit and narrow temperature range observed here.

The high temperature sensitivity of the nanowire morphology may have important implications in nanotechnology of II-VI optoelectronic devices. This finding suggests that the morphology of ZnO grown by MOCVD is critically dependent on the growth temperature, due to variable nucleation rates, island growth and rate of island coalescence.

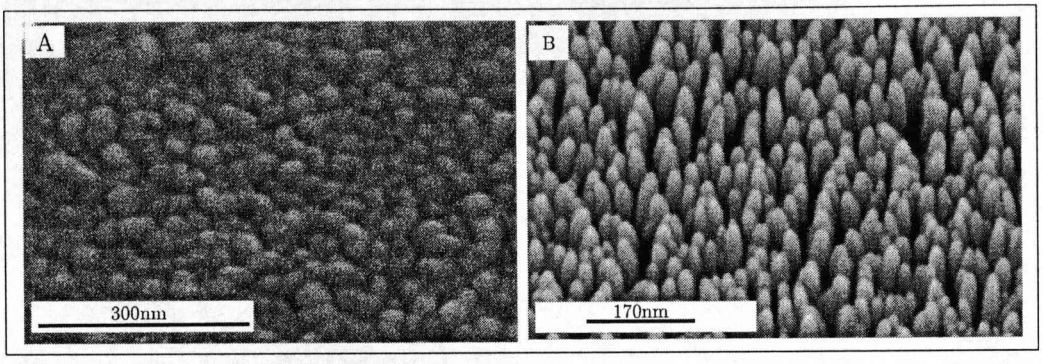

Figure 6.7. Scanning electron micrographs of ZnO films deposited at a) 450°C and b) 500°C

X-Ray Diffraction analysis was carried out in order to determine the crystallinity of the ZnO films grown at the optimised temperature of 500°C (Figure 6.8a). Only the (0002) reflection of the wurtzitic phase (P63mc) was observed to be present at a 2θ value of 34.44°. This suggests that the ZnO has highly preferred orientation with respect to the silicon substrate.

The feasibility of using these ZnO nanowires as a compliant layer for the deposition of epitaxial GaN was investigated using MBE. Depositional growth runs were undertaken using substrate temperatures in the range 600°C to 850°C.

6.4 Deposition of GaN on ZnO nanowires using [$Me_2Zn(THF)$]

Before investigating the deposition of GaN on the ZnO nanowires, it was thought to be prudent to investigate their thermal stability in vacuum because of concerns about sublimation. To achieve this, samples were annealed in a vacuum for 15 minutes at temperatures ranging from 600-800°C, and Energy Dispersive X-ray analysis (EDAX) was employed to determine the chemical composition and percentage of the films. For films annealed at 600 and 700°C there was no noticeable difference in the percentage of Zn to the as-grown Zn. However, upon annealing at 800°C the Zn started to marginally sublime. Based on this evidence it was decided to employ a nitrogen atom source for the deposition of GaN instead of ammonia which requires higher deposition temperatures to achieve on-surface 'cracking'. The decision to use a nitrogen atom source rather than ammonia source was aimed at lowering the GaN deposition temperature from 850°C to 600°C, thus enabling the ZnO layer to be capped with an LT-GaN layer and to minimise any sublimation of the ZnO.

Figure 6.8(b) shows the XRD features arising from one of the GaN films deposited onto the ZnO at a growth temperature of 500°C. The resulting GaN layer was approximately 100nm thick. It is clear from this figure that the diffraction pattern is dominated by a single reflection at 34.70° which was initially attributed to the (0002) peak of the hexagonal GaN phase. This peak value represents a slight shift from the original ZnO peak (34.44°) and was initially assumed that the GaN peak intensity was

simply superimposed on the (0002) reflection of the underlying ZnO nanowires. In fact this was found not to be the case after a cross-sectional sample of the film was investigated using TEM. Figure 6.9 presents the bright field micrograph for this sample, which was measured from the cross section oriented with the [11$\bar{2}$] zone-axis of the silicon substrate parallel to the electron-optic axis. The micrograph clearly shows that there are three distinct layers: (i) the silicon substrate; (ii) an intermediate layer; and (iii) the GaN layer. The GaN layer comprises of a nanoscale columnar structure with column widths in the order of ~40nm, which evolve from the interlayer microstructure.

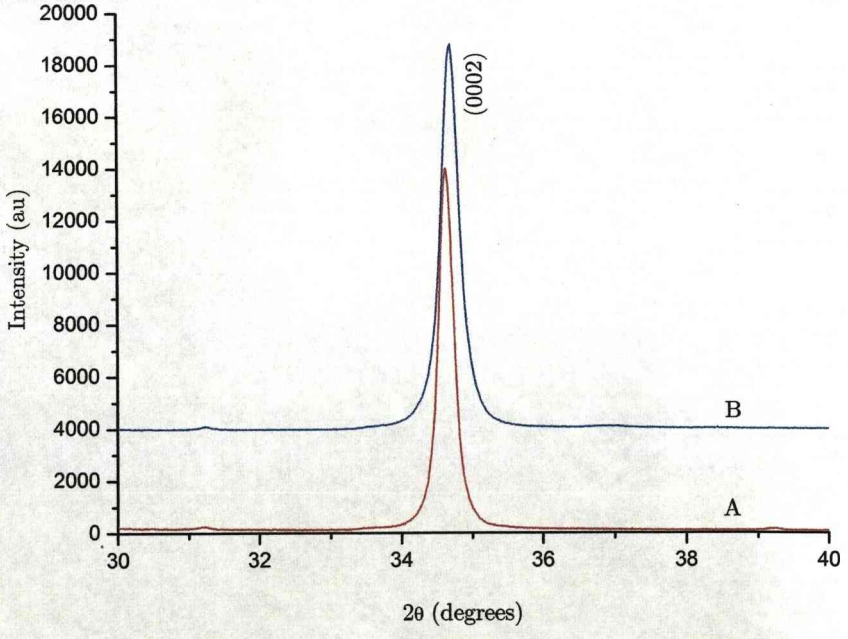

Figure 6.8. X-ray diffraction pattern of (a) ZnO film deposited at 600°C and (b) GaN/GaOx/Si(111)

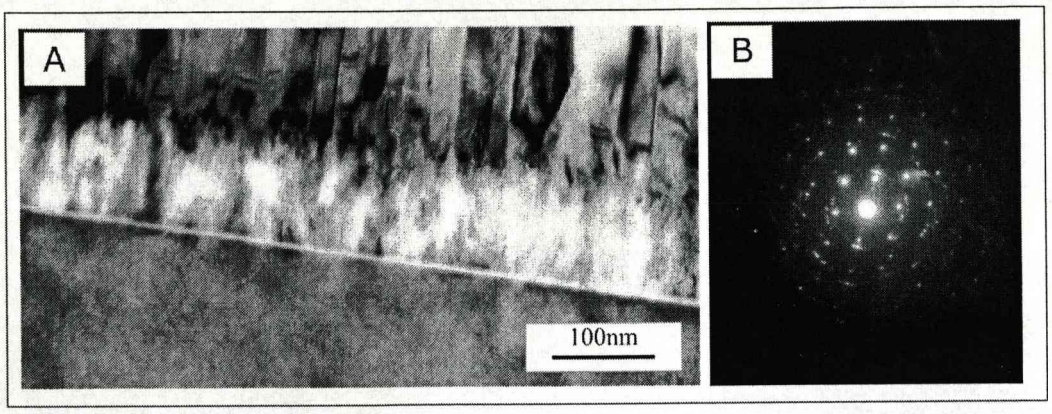

Figure 6.9. a) Bright field image of a $GaN/GaO_x/Si(111)$ sample prepared in cross-section and b) selective area diffraction of epi-layer and substrate.

Analysis of the nano-scale chemical composition was conducted using EDX in a STEM. The results of the EDX analysis soon revealed that the interlayer was composed predominantly of Ga and O instead of the ZnO stoichiometry expected. In order to substantiate this observation, samples of the same material were further analysed using Auger Electron Spectroscopy. The data from the AES analyses is shown in Table 6.3 and confirms that the intermediate layer was composed of GaO_x, with no evidence for the presence of Zn.

Table 6.3. AES data for the GaN film deposited onto the optimised Si(111) / ZnO substrate (arbitrary units)

Etch Time (s)	*N*	*O*	*Ga*
0	33	69	84
20	31	68	80
120	21	10	62
180	47	66	117
300	45	50	90
420	25	42	60
600	0	121	68
720	0	70	34
900	Si Substrate		

These results are rather surprising, given that several previous studies have demonstrated the successful MBE-based deposition of GaN onto ZnO buffer layers [20-21]. For example, when depositing GaN by MBE onto ZnO substrates, Xing Gu *et al* observed well-resolved ZnO and GaN peaks using high-resolution XRD, with no sign either of sublimation of the ZnO or the formation of a Ga_xZnO_y phase. One possible explanation for the contradiction between the results presented here and their study may be due to the morphology of the ZnO interlayers. In particular, the removal or conversion of the ZnO in this study could be attributable to the relatively high surface area of the three-dimensional nanorod structure of the ZnO compared with a two-dimensional film surface. The higher surface area of the nanorods makes them more susceptible to degradation under the fluxes of Ga and N in the MBE reactor. This may lead to rapid desorption of either a zinc or zinc-nitride species and the formation of GaO_x by an oxygen-nitrogen exchange reaction (shown schematically in Figure 6.10). Some support for the proposal for the

removal or conversion of the ZnO is provided by the observation that ZnO dissociates in NH_3 at temperatures above 650°C [22-23].

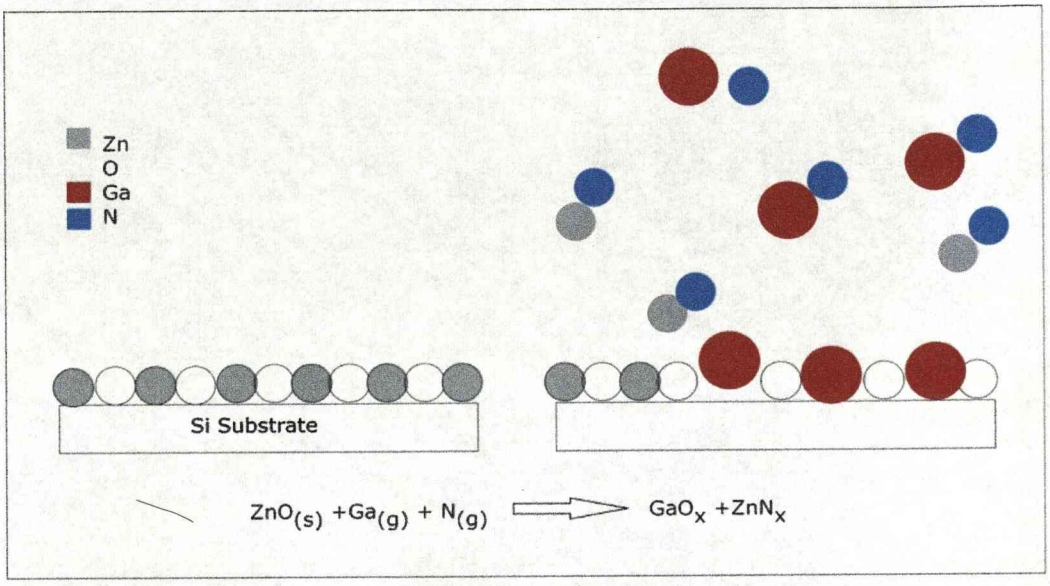

Figure 6.10 Schematic representation of the conversion of ZnO to GaO_x in the MBE process

It is intuitively somewhat surprising that all of the zinc detectable by AES, is 'lost' from the interlayer during the GaN deposition process. To establish the extent of the loss of zinc with a higher degree of sensitivity, a sample was analysed using sputtered neutral mass spectrometry (SNMS). The analysis was carried out using a commercial facility by Dr Simon Romani. A depth profile through the film / interlayer / substrate structure was made using a 10kV Ar^+ ion beam with a VG SIMS lab 3A. Depth profiles of Zn, Ga, O, C and Si were measured as shown in figure 6.11. The silicon interface is clearly defined by the onset of Si counts that occurs at ~125nm depth. This benchmarks the thickness of the GaN layer and the oxide at the interface between the film and substrate. More

significantly, the Zn profile indicates that the [Zn] concentration is reduced to only a few hundreds on an atomic percent (e.g. orders of magnitude less than the 50% expected). The Zn concentration was callibrated using RBS data of zinc standard material. Although the Zn is apparently efficiently etched from the interlayer, it is notable that virtually all of the oxygen from the original ZnO layer is incorporated into some type of GaO_x interfacial region.

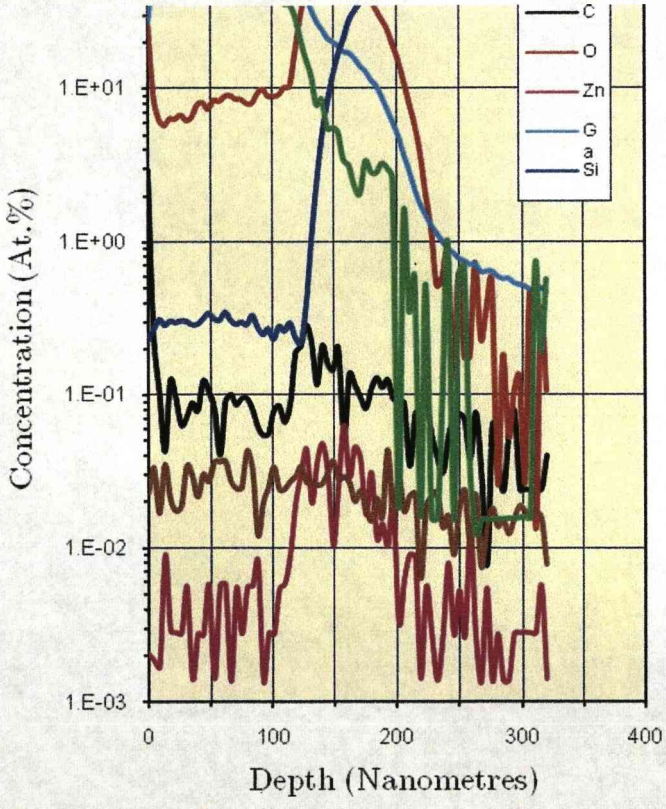

Figure 6.11 SNMS depth profile of elements in a film after GaN deposition on a ZnO/Si(111) substrate.

Based on this finding, it became apparent that an alternative precursor had to be chosen in order to facilitate the deposition of a two-

dimensional ZnO film. This forms the focus for the work described in the following sections.

6.5 Zinc oxide MOCVD using $Zn(thd)_2$ (thd=2,2,6,6-tetramethyl- 3,5-heptanedionato)

Liquid injection MOCVD of $Zn(thd)_2$ has been previously been investigated at the University of Liverpool for the purposes of depositing thin films of zinc ferrite.[24]. The earlier work also found that a dramatic variation in the morphology of binary ZnO occurs with varying substrate temperature. It was found that highly textured films could be deposited using this approach. On this basis, it was decided to investigate the heteroepitaxial deposition of ZnO on Si(111) using $Zn(thd)_2$ in order to prepare compliant buffer layers for subsequent MBE GaN deposition studies.

The growth parameter for ZnO deposition using $Zn(thd)_2$ are shown in Table 6.4

Table 6.4. Growth conditions used to deposit ZnO films by liquid injection MOCVD using $Zn(thd)_2$

Substrate Temperature	350-600°C on Si(111)
Evaporator Temperature	200°C
Reactor Pressure	5mbar
Precursor solution injection Rate	$30cm^3$ /hr
Solvent	heptane
Concentration	0.05M
Argon flow	200 cm^3min^{-1}
Oxygen flow	100 cm^3min^{-1}
Run time	10 min

Figure 6.12 shows the relationship between growth temperature and the ZnO growth rate using the $Zn(thd)_2$ precursor. The graph demonstrates that the ZnO growth rate increases with substrate temperature up to 600°C. Above this temperature the trend is reversed and the growth rate rapidly decreases. The data suggests that an optimal growth temperature of 600°C should be employed throughout the subsequent growth experiments. Using this optimal temperature, films of varying thickness in the range of 20-100nm were deposited.

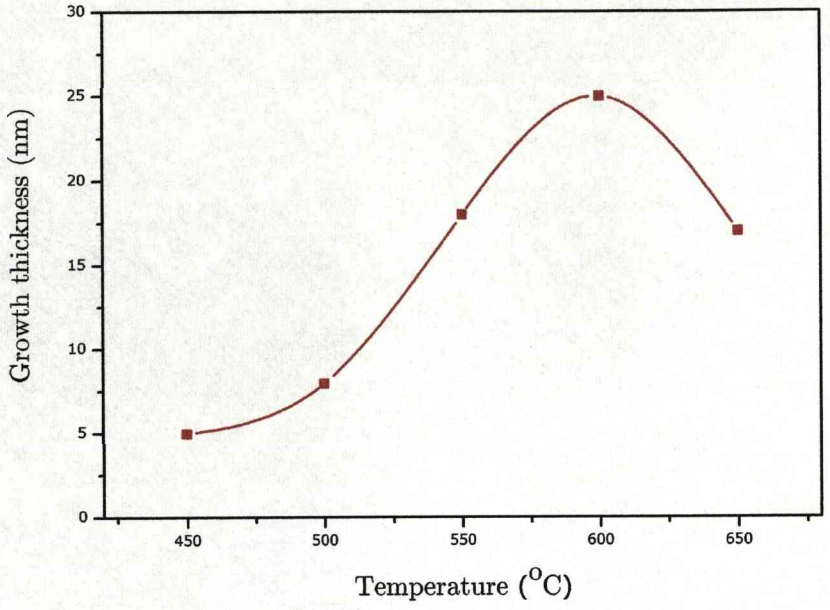

Figure 6.12. The growth rate of zinc oxide by MOCVD from the $Zn(thd)_2$ precursor

AES was used to determine the atomic composition of the films. The results of the AES are presented in Table 6.4.

Table 6.5. AES data for ZnO films deposited using $Zn(thd)_2$

Sample label	*Etch time (s)*	*O*	*Zn*
ZnO 86nm	20	48.8	51.2
	40	49.6	50.4
	60	49.6	50.4
	120	49.6	50.4
	240	49.6	50.4

An SEM micrograph of a ZnO film of thickness 92nm demonstrates a microstructure comprising of equiaxed grains of uniform dimensions of

approximately 250nm (Figure 6.13). XRD analysis of the same film (not shown here) showed only the ZnO (0002) reflection to be present (34.46°), pointing towards the ZnO as being polycrystalline in nature and having a preferred orientation with respect to the substrate.

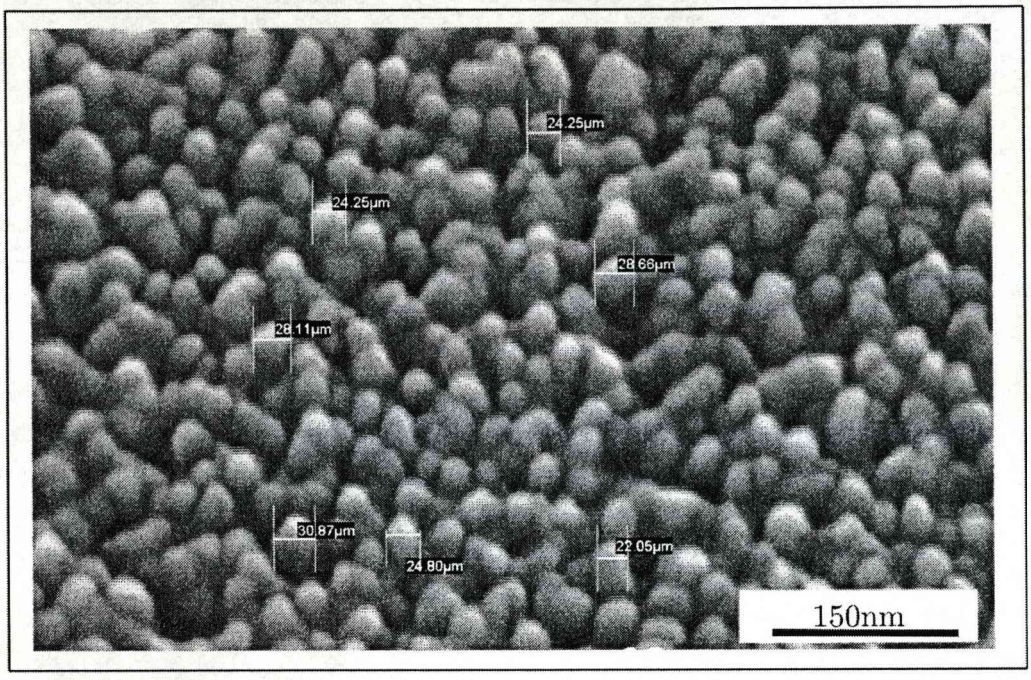

Figure 6.13. Scanning electron micrograph of a ZnO film deposited using $Zn(thd)_2$

Films of heteroepitaxially oriented ZnO were deposited on Si(111) substrates using $Zn(thd)_2$ at 600°C. These layers were subsequently used to investigate the possibility of depositing epitaxial GaN.

6.6 Deposition of GaN on ZnO layers deposited from $Zn(thd)_2$

A layer of GaN (~200nm) was deposited by MBE at 650°C on a ZnO film with a thickness of 54nm. Like the GaN/ZnO structures grown with

DMZ, only a single reflection at 34.66° was apparent in the XRD spectrum (Figure 6.14).

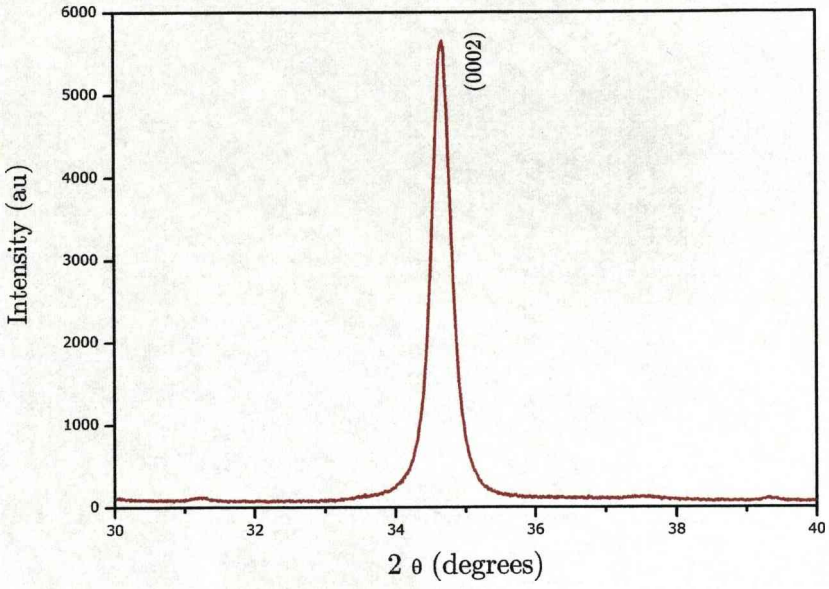

Figure 6.14. X-ray diffraction pattern of GaN/ZnO/Si (111)

The sample was prepared for cross-sectional TEM investigation, which once again revealed three distinctive layers (Figure 6.15). Upon further investigation employing EDX it was seen that this time ZnO was still present in the thin film structure. However, AES analysis did demonstrate that a partial ZnO/GaO_x interface had formed during the deposition process.

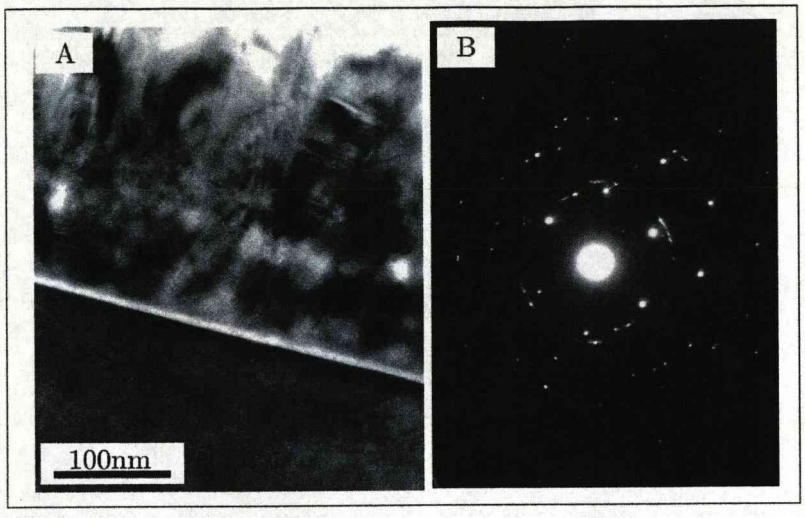

Figure 6.15. (a) Cross-sectional TEM bright field image of GaN/ZnO/Si(111) (b) Selective area diffraction pattern

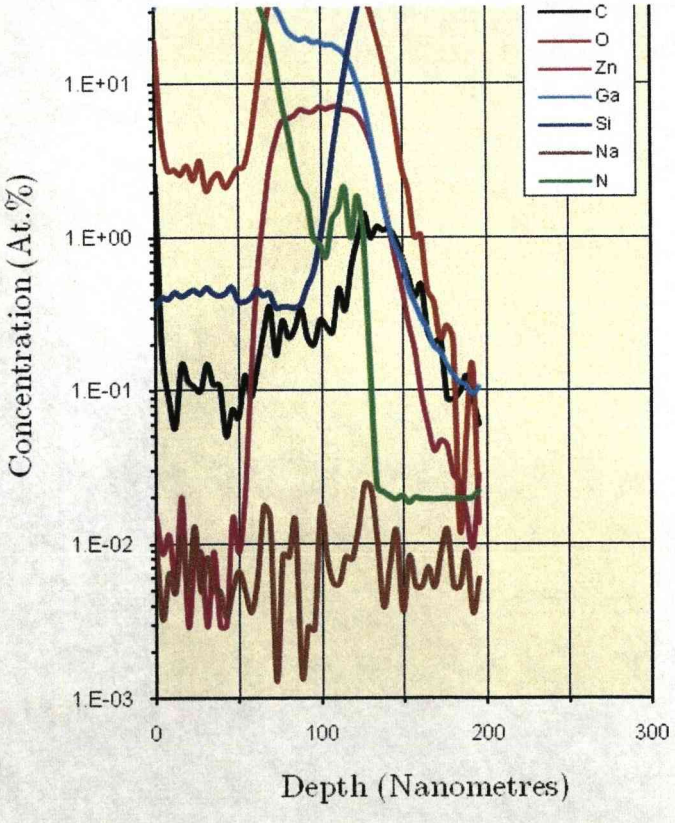

Figure 6.16. SNMS depth profile of elements in a film after GaN deposition on a ZnO/Si(111) substrate

A sample of this material was analysed using sputtered neutral mass spectrometry (SNMS). The analysis was carried out using the same conditions used for the data shown in Figure 6.11. Depth profiles of Zn, Ga, O, C and Si were measured as shown in figure 6.16. The silicon interface is again clearly defined by the onset of Si counts that occurs at ~80 to 90nm depth. In this sample, the Zn profile indicates that the [Zn] concentration remains closer to the concentration expected within the ZnO layer but nevertheless reduced to 7 to 9at%. It is also apparent that the interlayer conatins a significant concentration of GaN which would seem to suggest the formation of a $Ga_xZn_yO_z$ composition or some composite structure of the binary gallium and zinc oxides.

6.7 Conclusions

The feasibility of depositing gallium nitride on silicon by molecular beam epitaxy has been demonstrated employing a ZnO compliant layer. Initially the precursor [$Me_2Zn(THF)$] was employed at an optimum growth temperature of 500°C. This produces films consisting of nano-rods, whilst the second precursor [$Zn(thd)_2$] shows films with a columnar morphology. AES analysis shows that both precursors give stoichiometric films with no detectable carbon contamination.

The growth of gallium nitride on both types of ZnO films has been investigated. GaN films grown at 600°C by MBE on [$Me_2Zn(THF)$] ZnO films led to the complete removal of the ZnO and the formation of a [$Si/GaO_x/GaN$] heterostructure. In contrast to this, GaN deposited on

ZnO films employing $[Zn(thd)_2]$ as the precursor, led to the retention of the ZnO layer along with a $Ga_xZn_yO_z$ interlayer.

It has been shown that the integrity of the ZnO layer is critically dependent on its morphology. The surface morphology of the ZnO is also dependent on the nature of the Zn precursor and the substrate temperature.

References:

[1] X. Duan, Y. Huang, Y. Cui, J. Wang, C.M. Lieber, Nature 409 (2001) 66.

[2] S. Liang, H. Sheng, Y. Lin, Z. Hio, Y. Lu, H. Shen, J. Crystal Growth 225 (2001) 110.

[3] N. Golego, S.A. Studenkin, M. Cocivera, J. Electrochem. Soc. 147 (2000) 1592.

[4] N.W. Emanetoglu, C. Gorla, Y. Liu, S. Liang, Y. Lu, Mater. Sci. Semicond. Process. 2 (1999) 247.

[6] T. Hata, T. Minamikawa, O. Morimoto, T. Hada, J. Crystal Growth 47 (1979) 171.

[7] J.O. Barnes, D.J. Leary, A.G. Gordon, J. Electrochem. Soc. 7 (1980) 1636.

[8] J. Aronovich, A. Oritiz, R.H. Bube, J. Vac. Sci. Technol. 16 (1979) 994.

[9] F. Hamdani, M. Yeadon, D.J. Smith, H. Tang, W. Kim, A. Salvador, A.E. Botchkarev, J.M. Gibson, A.Y. Polyakov, M. Skowronski, H. Morkoc- , J. Appl. Phys. 83 (1998) 983.

[10] W. Kern, R.C. Heim, J. Electrochem. Soc. 117 (1970) 562.

[11] P.A. Lane, P.J. Wright, M.J. Crosbie, A.D. Pitt, C.L. Reeves, B. Cockayne, A.C. Jones, T.J. Leedham, J. Crystal Growth 192 (1998) 423.

[12] J. Auld, D.J. Houlton, A.C. Jones, S.A. Rushworth, M.A. Malik, P. O'Brien, G.W. Critchlow, J. Mater. Chem. 4 (1994) 1249.

[13] F.T.J. Smith, Appl. Phys. Lett. 43 (1983) 1108.

[14] C.K. Lau, S.K. Tiku, K.M. Lakin, J. Electrochem. Soc. 127 (1980) 1843.

[15] R. Solanki, G.J. Collins, Appl. Phys. Lett. 42 (1983) 662.

[16] R.H. Moss, J. Crystal Growth 68 (1984) 78.

[17] A.C. Jones, Semicond. Sci. Technol. 6 (1991) A36.

[18] P. J. Wright, R. J. M. Griffiths, B. Cockayne J.Crystal Growth **66** *Issue 1* (1984)

[19] Quanchang Li, Vageesh Kumar, Yan Li, Haitao Zhang, Tobin J. Marks, and Robert P. H. Chang *Chem. Mater.* **17** 1001-1006 (2005)

[20] X. Gu, M.A. Reschikov, A. Teke, D. Johnstone, H. Morkoc, B. Nemeth, J. Nause, Appl. Phys. Lett. 84 (2004) 2268.

[21] X.H. Luo, R.M. Wang, X.P. Zhang, H.Z. Zhang, D.P. Yu, M.C. Luo, Micron 35 (2004) 475.

[22] Q. Li, V. Kumar, Y. Li, H. Zhang, T.J. Marks, R.P. Chang, Chem. Mater. 17 (2005) 1001.

[23] E.S. Hellman, Alternative oxide substrates for GaN heteroepitaxy, in: J.H. Edgar, S. Strite, I. Akasaki, H. Amano, C. Wetzel (Eds.), Gallium Nitride and Related Semiconductors, INSPEC, London, 1999, p. 396.

[24] P.A. Lane, P.J. Wright, M.J. Crosbie, A.D. Pitt, C.L. Reeves, B. Cockayne, A.C. Jones and T.J. Leedham. *Journal of Crystal Growth*, 1998, **192**, 423.

Chapter 7

Conclusions and future work

7.1 Introduction

In summary, three general classes of thin film materials have been investigated as potential compliant layers for the epitaxy of gallium nitride on silicon. The materials systems include perovskite-based rare earth aluminates; a rocksalt nitride system; and a hexagonal symmetry oxide based buffer layer. The central purpose behind the research has been to develop a process based on metalorganic chemical vapour deposition, which could be readily incorporated into the typical growth equipment used for existing III-nitrides such as GaN.

7.2 Conclusions

In Chapter 4 the deposition of lanthanum and praseodymium aluminate by MOCVD and ALD has been investigated using a single source alkoxide precursor $[MAl(OPr^i)_6(PriOH)]_2$. This precursor forms aluminate films which are amorphous as-deposited by MOCVD or ALD in the temperature range 150°C to 600°C. However the as-deposited films are non-stoichiometric (from the perovskite composition) but subsequent annealing in air can be used to crystallize the films at temperatures between 750° and 850°C. After annealing the films exhibit a polycrystalline microstructure and some interaction is indicated between the film and the silicon substrate. Capacitance-voltage measurements show that the permittivity of the film is 13 for $LaAlO_3$ and 14 for $PrAlO_3$

at strong accumulation. The leakage current densities of the $LaAlO_3$ films are 7 x 10^{-8} A cm^{-2} at 1V for ALD and 2 x 10^{-7} A cm^{-2} at 1V for MOCVD grown films.

The growth of gallium nitride on these films produces a polycrystalline GaN film textured in the [0001] direction. This is accompanied by a minimal interaction between the oxide and GaN. These results suggest that if adverse interfacial interactions can be suppressed (e.g. by a SrO seed layer) between the silicon and perovskite, then a better epitaxial orientation might be achieved.

Chapter 5 explored the deposition of LaN on Si(111) using a Ln-alkylsilylamido precursors of the type $La[N(SiMe_3)_2]_3$. It was hypothesised that a sequential transamination reaction would occur in the gas phase leading to an intermediate precursor for the deposition of the rare earth nitride on the substrate. The transamination reaction was confirmed at low temperatures and no indication of silicon or carbon was evident in the films. However analysis of the films by AES shows that La_2O_3 has been deposited in preference to the nitride. This is attributed to the enthalpy and free energy of formation which favours the oxide rather than the nitride. The lack of the equipment integrity also hampers the nitride growth because small amounts of oxygen contamination. However the stability of the LaN is the predominant factor as MBE growth studies showed even in UHV LaN transforms to the oxide on exposure to the ambient.

MBE studies of ScN growth have demonstrated that it does not suffer the same instability issues as LaN. The optimum growth temperature for ScN is ~ 850°C. Selective area diffraction patterns demonstrate an epitaxial relationship between the ScN and Si substrate that is expressed as $(111)_{ScN}//(111)_{Si}$ and $[1\ \bar{1}0]_{ScN}//[0\ \bar{1}1]_{Si}$.

Selective area diffraction analysis indicates that on optimized ScN layers the following orientations occur in the structures: GaN [0001] // Si [111] and GaN(1 $\bar{1}$00) // Si(11 $\bar{2}$).

The precursor $Sc[N(SiMe_3)_2]_3$ has been investigated for the deposition of ScN in the presence of NH_3 by MOCVD. It was found that the precursor had insufficient volatility and thermal stability for transport. At extremely low temperature (50°C) and high carrier gas flows some transport was achieved but scandium oxide was formed rather than ScN. A high-integrity, custom designed MOCVD reactor system is necessary, if the deposition of ScN using this precursor system is to be realised

In chapter 6, the possibility of depositing gallium nitride on silicon by molecular beam epitaxy has been demonstrated employing a ZnO compliant layer. The precursor $[Me_2Zn(THF)]$ was exploited at an optimum deposition temperature of 500°C. This generates films consisting of nano-rods, whilst the second precursor $[Zn(thd)_2]$ shows films with a columnar morphology. AES analysis shows that both

precursors give stoichiometric films with no detectable carbon contamination.

The growth of gallium nitride on both morphologies of ZnO films has been investigated. GaN films deposited at 600°C by MBE on $[Me_2Zn(THF)]$ ZnO films resulted in the complete removal of the ZnO and the formation of a $[Si/GaO_x/GaN]$ heterostructure. However GaN grown on ZnO films employing the $[Zn(thd)_2]$ precursor, led to the retention of the ZnO layer along with a 2nm $Ga_xZn_yO_z$ interlayer.

It has been demonstrated that the ZnO integrity is critically dependent on its morphology. The surface morphology of the ZnO is also dependent on the nature of the Zn precursor and the substrate temperature at which it is deposited.

7.3 Future Work

The investigations carried out in this thesis have raised further questions which are beyond the scope of the present study but would be worthwhile pursuing for future research. In summary these areas are:

1) Growth conditions and precursors for the controlled stoichiometry of $LaAlO_3$ and $PrAlO_3$.

   In Chapter 4, the use of the single-source precursors $[MAl(OPr^i)_6(PriOH)]_2$ (M = La or Pr) was targeted in order to control the stoichiometry of the $MAlO_3$ films. In practice, this was not the case. One cause of this is presumed to be the premature

decomposition of the precursor during delivery. The development of other single-source precursors, with better thermal stability might overcome this problem in liquid injection MOCVD. One route to achieving this would be the development of heteroleptic alkoxide precursors to provide greater stearic protection of the metal atoms. In ALD, better self-limiting growth is achieved in precursors which are designed to inhibit β-hydride elimination. Although unclear at this stage, this mechanism might account for the difficulties in controlling to stoichiometry of the $MAlO_3$ films and merits further consideration.

2) The SrO seed layer.

Although the purpose of the research in Chapter 4 was to identify a route for the deposition of perovskite aluminate films, the end application was intended for epitaxial growth on silicon. As discussed, the development of SrO as a 'seed' layer was meant to suppress SiO_x formation and provide an epi-template for subsequent growth of the oxide compliant layer. Regrettably, this was not pursued in the COSMOS project due to time considerations. It would seem fruitful, if the SrO process developed at Qinetiq could be combined with an appropriate compliant oxide deposition process.

3) MOCVD and ALD of the rock salt nitrides.

In Chapter 5, the deposition of rock salt nitrides was investigated using the transammination reaction. The susceptibility of this process to minute amounts of background oxygen meant that this

was not realised for $Sc[N(SiMe_3)_2]_3$. However, the potential use of scandium nitride as a buffer layer was demonstrated using molecular beam epitaxy. It would be worthwhile pursuing either the MOCVD or ALD processes in a nitride reactor. In fact Qinetiq have followed up this line of research using a commercial gallium nitride MOCVD reactor.

4) Low temperature routes to La_2O_3 and Sc_2O_3.

A serendipitous outcome of the work in Chapter 5 was the identification of a route to the low temperature deposition (< 150°C) to La_2O_3 and Sc_2O_3. Although the silylamide precursors contain silicon, the films deposited showed no silicon contamination. Further work should be investigated to fully characterise the deposition parameters of these sesquioxides using the controlled introduction of oxygen.

5) GaN MOCVD on ZnO nanorods.

In Chapter 6, the development of zinc oxide as a buffer layer material was investigated. The dimethyl zinc – THF adduct was found to deposit ZnO nanowires in the presence of oxygen. It is proposed that these nanowire structures may constitute ideal compliant structures for GaN growth. The work presented, has established that free gallium is probably detrimental to the stability of these nanowires. Therefore, an MOCVD nitride process based on ammonia and a gallium source such as trimethyl gallium would be preferable for the nitride deposition step (rather than MBE). Once

again, members of the COSMOS project consortium are pursuing this prospect further.

6) Understanding mechanisms of 2D and 1D ZnO growth.

The thin film growth of zinc oxide is becoming an area of significant interest, largely due to the electronic and optical properties of this material. An area of interest for future research must clearly be a better understanding of the mechanisms of one – and two-dimensional growth processes. In this work, both growth habits have been observed, however there seems to be an absence of mechanistic studies to describe this process in the open literature.